

POLITECNICO DI MILANO

School of Industrial and Information Engineering
Department of Chemistry, Materials and Chemical Engineering "Giulio Natta"
Master of Science in Materials Engineering and Nanotechnology



POLITECNICO
MILANO 1863

**ADDITIVE MANUFACTURING OF GEOPOLYMERS
FILLED WITH END-OF-LIFE MATERIALS**

Supervisor: Prof. Marinella LEVI

Co-Supervisors: Prof. Stefano TURRI

Dr. Riccardo CIAPPONI

Emanuele AGNOLI

ID 872176

Academic Year 2017-2018

Table of contents

Table of contents	i
List of figures	v
List of tables	xiii
Glossary	xv
Nomenclature of the formulations	xvii
Abstract	xix
Estratto in lingua italiana	xxi
Aim of the thesis	xxv
1. Introduction	1
1.1. Overview on additive manufacturing	1
1.1.1. Definition and classification of additive manufacturing.....	1
1.1.2. Generalized additive manufacturing process chain	6
1.1.3. Past, present and future of additive manufacturing	7
1.2. Additive manufacturing of cementitious and ceramic materials.....	9
1.2.1. Building and construction	9
1.2.2. Other fields of application	15
1.3. Geopolymers	17
1.3.1. Geopolymerization.....	17
1.3.2. Factors affecting geopolymer properties	19
1.3.3. Geopolymer as alternative to Portland cement	21
1.4. The use of waste materials for filler purposes	24
1.4.1. Microalgae for wastewater treatment	24
1.4.2. Lignin from wood pulping processes.....	28
1.4.3. Recycled glass fibres	29
2. Materials and methods	31
2.1. Materials.....	31
2.1.1. Metakaolin	31

2.1.2.	Alkaline activator	32
2.1.3.	Bentonite	32
2.1.4.	Biomass	32
2.1.5.	Recycled fibres.....	34
2.2.	Formulations.....	35
2.2.1.	Formulations for 3D printing	35
2.2.2.	Formulations for casting.....	38
2.2.3.	Formulations to study the effect of bentonite.....	39
2.3.	3D printing setup	40
2.3.1.	3DRag.....	40
2.3.2.	Scale-up setup	42
2.4.	Preparation of the samples.....	46
2.4.1.	Preparation of the pastes	46
2.4.2.	Casting.....	46
2.4.3.	3D printing	47
2.5.	Characterization techniques.....	49
2.5.1.	Characterization techniques adopted in preliminary studies.....	49
2.5.1.1.	Thermogravimetric analysis (TGA)	49
2.5.1.2.	X-ray diffraction (XRD).....	49
2.5.1.3.	Fourier Transform Infra-Red Spectroscopy	50
2.5.2.	Rheology	50
2.5.3.	Compression tests.....	54
2.5.4.	Scanning electron microscope (SEM) and Energy-dispersive X-ray spectroscopy (EDS)	55
3.	Results and discussion	57
3.1.	Preliminary studies	57
3.2.	Unfilled geopolymer.....	58
3.2.1.	Metakaolin and activator	58
3.2.2.	Effect of bentonite addition.....	59

3.2.3.	Effect of bentonite type.....	63
3.3.	Geopolymers filled with microalgae.....	65
3.3.1.	High-bentonite formulation.....	65
3.3.1.1.	Rheological behaviour of the pastes.....	65
3.3.1.2.	Compression tests on fresh specimens.....	67
3.3.1.3.	Compression tests on hardened specimens.....	69
3.3.1.4.	SEM and EDS analyses.....	80
3.3.2.	Low-bentonite formulation.....	92
3.3.2.1.	Rheological behaviour of the pastes.....	92
3.3.2.2.	Compression tests on hardened specimens.....	99
3.3.2.3.	SEM and EDS analyses.....	104
3.3.3.	High concentration of biomass.....	109
3.4.	Feasibility study on the use of recycled glass fibres as filler.....	112
3.4.1.	Rheological behaviour of the pastes.....	112
3.4.2.	Compression tests on hardened specimens.....	115
3.4.3.	SEM and EDS analyses.....	117
3.5.	Scale-up.....	121
3.5.1.	Materials for scale-up.....	121
3.5.2.	Scale-up process and results.....	123
4.	Conclusions and future developments.....	129
4.1.	Conclusions.....	129
4.2.	Future developments.....	131
Appendix.....	133
Results of preliminary studies.....	133
Estimation of maximum height of printed structures.....	137
Bibliography.....	139
Ringraziamenti.....	147

List of figures

Figure 1.1.1. Schematic diagram of binder jetting process [2].....	2
Figure 1.1.2. Schematic diagram of a typical direct energy deposition process [4].....	2
Figure 1.1.3. Schematic representation of FDM (a) and DW (b) systems [7].....	3
Figure 1.1.4. Scheme of material jetting process [8]	4
Figure 1.1.5. Schematic representation of powder bed fusion AM process [7]	4
Figure 1.1.6. Scheme of sheet lamination AM process [7].....	5
Figure 1.1.7. Schematic representation of SLA [7]	5
Figure 1.1.8. Scheme of a general AM process [7]	7
Figure 1.1.9. Examples of objects which are impossible to produce (in one piece) by traditional manufacturing techniques [17].....	9
Figure 1.2.1. Schematic representation of large- scale Contour Crafting [23].....	10
Figure 1.2.2. Schematic representation of D-shape processes [23]	11
Figure 1.2.3. Castle printed in-situ by Andrey Rudenko [25]	12
Figure 1.2.4. Structures printed by WinSun: house (a) and five-story apartment (b) [25]	12
Figure 1.2.5. (a) BigDelta machine by WASP and (b) 3D printed structure [27]	13
Figure 1.2.6. Crane by WASP: (a) blueprint of the modular structure, (b) printing process, (c) final printed structure (Gaia), with added windows and roof [27].....	13
Figure 1.2.7. Structures obtained by D-shape technique: (a) project fo the city hall of Pondera, (b) complete house, (c) CAD and actual printed part of a structural block designed for a lunar outpost.....	14
Figure 1.3.1. Different steps of geopolymerization, divided in two groups: dissolution (in black box) and condensation/gel formation (in red box). Adapted from [44] and [43].....	18
Figure 1.3.2. Types of poly-sialates and their structures. Adapted from [37] and [44]..	19
Figure 1.4.1. Scheme of eutrophication process [68]	25
Figure 1.4.2. Configurations for suspension cultures: (a) open pond in raceway configuration; (b) tubular closed photobioreactor; (c) air-lift flat panel [71].....	27
Figure 1.4.3. Structure of lignin [77]	28

Figure 2.1.1. Particle size distribution (cumulative fraction in black, distribution fraction in red) of metakaolin Mefisto L05, provided by the supplier	32
Figure 2.3.1. 3DRag in (a) FDM and (b) LDM configuration	40
Figure 2.3.2. Schematic representation of LDM syringe extruder, designed by Dr. Gabriele Natale [88]	41
Figure 2.3.3. Delta WASP 40100 Clay	42
Figure 2.3.4. (a) STL model and (b) rendering of the machine toolpath of the pipe for scale-up printing	43
Figure 2.3.5. (a) Pirelli skyscraper; (b) STL model; (c) rendering of machine toolpath, evidencing the infill.....	44
Figure 2.3.6. (a) STL model and (b) rendering of machine toolpath, evidencing the spiral mode, of the hollow twisted structure selected for scaled-up printing.....	45
Figure 2.4.1. PDMS moulds used for casting	46
Figure 2.4.2. PLA 3D printed mould used for fresh samples.....	47
Figure 2.4.3. Hardened samples. From left to right: 3D printed hollow cylinder, casted cylinder, casted cube	48
Figure 2.4.4. 3D printed full specimens	48
Figure 2.5.1. Rotational rheometer Kinexus Pro+	51
Figure 2.5.2. Fitting with Herschel-Bulkley model performed on flow curves of the formulation HB-GEO	52
Figure 2.5.3. Model of a creep and recovery curve, in which the three different responses are highlighted. Adapted from [91]	54
Figure 2.5.4. (a) ZwickRoell Z010 dynamometer equipped with square plates for compression test; (b) plates during the test of a sample.....	54
Figure 2.5.5. Scanning electron microscope EVO 50 Extended Pressure	56
Figure 3.2.1. Viscosity curve of the alkaline activator (a) and of geopolymer (only metakaolin and alkaline activator) (b).....	58
Figure 3.2.2. Yield stress and compression strength plotted against the amount of bentonite.....	60
Figure 3.2.3. SEM micrograph and EDS analysis of sample C-GEO.....	61
Figure 3.2.4. Flow curves of geopolymer pastes (low-bentonite formulation) containing different kinds of commercial bentonites.....	63

Figure 3.2.5. Compression strength of 3d-printed specimens after 7 days of ambient curing. Comparison between different bentonites and formulations	64
Figure 3.3.1. Flow curves of high-bentonite printable pastes, containing Spirulina	65
Figure 3.3.2. Flow curves of high-bentonite printable pastes, containing Tetraselmis ..	66
Figure 3.3.3. Yield stress against biomass amount added to geopolymer pastes with HB formulation.....	67
Figure 3.3.4. Stress-strain curves of fresh specimens (HB formulation, containing different amount of Spirulina), tested in compression.....	68
Figure 3.3.5. Compressive strength of geopolymers (high-bentonite formulation, containing biomass), tested on 3D printed hollow cylinders after 7 days of ambient curing	70
Figure 3.3.6. Compressive strength of geopolymers (high-bentonite formulation, containing biomass), tested on 3D printed hollow cylinders after 28 days of ambient curing	71
Figure 3.3.7. Compressive strength of geopolymers (high-bentonite formulation, containing biomass), tested on 3D printed hollow cylinders after 7 days of ambient curing and 4 hours of annealing at 800°C.....	72
Figure 3.3.8. Compressive strength of geopolymers (high-bentonite formulation, containing biomass), tested on 3D printed hollow cylinders after 28 days of ambient curing and 4 hours of annealing at 800°C.....	73
Figure 3.3.9. Compressive strength of geopolymers (high-bentonite formulation, containing biomass), measured on cubic casted samples after 28 days of ambient curing, annealed or not.....	74
Figure 3.3.10. Comparison between compressive strength values of 3D printed and casted samples, evaluated at 28 days of curing at ambient temperature.....	75
Figure 3.3.11. Comparison between compressive strength values of 3D printed and casted samples, evaluated at 28 days of curing at ambient temperature and 4 hours of annealing at 800°C	76
Figure 3.3.12. Example of an annealed cylindrical casted specimen. Cracks are evident before testing (a) and a burning in the central region can be observed from the fracture surface (b).....	77

Figure 3.3.13. Compressive strength of geopolymers (high-bentonite formulation, containing microalgal biomass residues), tested on 3D printed hollow cylinders after 7 days of ambient curing.....	78
Figure 3.3.14. Compressive strength of geopolymers (high-bentonite formulation, containing microalgal biomass residues), tested on 3D printed hollow cylinders after 28 days of ambient curing.....	78
Figure 3.3.15. Compressive strength of geopolymers (high-bentonite formulation, containing microalgal biomass residues), tested on 3D printed hollow cylinders after 7 days of ambient curing and 4 hours of annealing at 800°C	79
Figure 3.3.16. Compressive strength of geopolymers (high-bentonite formulation, containing microalgal biomass residues), tested on 3D printed hollow cylinders after 28 days of ambient curing and 4 hours of annealing at 800°C	79
Figure 3.3.17. SEM imaging and EDS spectra of the sample HB-GEO	80
Figure 3.3.18. SEM micrographs of sample HB-GEO at different magnifications	81
Figure 3.3.19. SEM imaging and EDS spectra of the sample HB-GSP5.....	81
Figure 3.3.20. SEM micrographs of sample HB-GSP5 at different magnifications	82
Figure 3.3.21. SEM imaging and EDS spectra of the sample HB-GTT5	82
Figure 3.3.22. SEM micrographs of sample HB-GTT5 at different magnifications	83
Figure 3.3.23. SEM imaging and EDS spectra of the sample HB-GLI5	83
Figure 3.3.24. SEM micrographs of sample HB-GLI5 at different magnifications.....	84
Figure 3.3.25. SEM imaging and EDS spectra of the sample HB-GEO (annealed).....	84
Figure 3.3.26. SEM imaging of annealed sample HB-GEO (magnified)	85
Figure 3.3.27. SEM imaging and EDS spectra of the sample HB-GSP5 (annealed).....	85
Figure 3.3.28. SEM imaging of annealed sample HB-GSP5 (magnified)	86
Figure 3.3.29. SEM imaging and EDS spectra of the sample HB-GTT5 (annealed)	86
Figure 3.3.30. SEM imaging of annealed sample HB-GTT5 (magnified).....	87
Figure 3.3.31. SEM imaging and EDS spectra of the sample HB-GLI5 (annealed)	87
Figure 3.3.32. SEM imaging of annealed sample HB-GLI5 (magnified).....	88
Figure 3.3.33. Compressive strength against average pore area (HB formulations)	91
Figure 3.3.34. Flow curves of low-bentonite printable pastes, containing Spirulina.....	92
Figure 3.3.35. Flow curves of low-bentonite printable pastes, containing Tetraselmis..	92

Figure 3.3.36. Yield stress against biomass amount added to geopolymer pastes with LB formulation.....	94
Figure 3.3.37. Plots resulting from dynamic rheological analyses performed in stress sweep, at constant frequency. The linear region and the crossover point are always visible.....	95
Figure 3.3.38. Creep and recovery curves of geopolymer pastes containing Spirulina .	97
Figure 3.3.39. Comparison between printable and non-printable pastes.....	97
Figure 3.3.40. Compressive strength of geopolymers (low-bentonite formulation, containing biomass), tested on 3D printed hollow cylinders after 7 days of ambient curing	100
Figure 3.3.41. Compressive strength of geopolymers (low-bentonite formulation, containing biomass), tested on 3D printed hollow cylinders after 28 days of ambient curing	100
Figure 3.3.42. Compressive strength of geopolymers (low-bentonite formulation, containing biomass), tested on 3D printed hollow cylinders after 7 days of ambient curing and 4 hours of annealing at 800°C.....	101
Figure 3.3.43. Compressive strength of geopolymers (low-bentonite formulation, containing biomass), tested on 3D printed hollow cylinders after 28 days of ambient curing and 4 hours of annealing at 800°C.....	101
Figure 3.3.44. Comparison between compressive strength of formulations LB-GEO and LB-GSP5, measured at 28 days on samples thermally treated or not.....	103
Figure 3.3.45. SEM micrograph and EDS spectra of sample LB-GEO	104
Figure 3.3.46. SEM micrographs at different magnifications (sample LB-GEO).....	104
Figure 3.3.47. SEM micrograph and EDS spectra of sample LB-GSP5	105
Figure 3.3.48. SEM micrographs at different magnifications (sample LB-GSP5).....	105
Figure 3.3.49. SEM micrograph and EDS spectra of sample LB-GEO (annealed)	106
Figure 3.3.50. SEM micrographs at different magnifications (sample LB-GEO (annealed))	106
Figure 3.3.51. SEM micrograph and EDS spectra of sample LB-GSP5 (annealed) ...	107
Figure 3.3.52. SEM micrographs at different magnifications (sample LB-GSP5(annealed)).....	107

Figure 3.3.53. Mixture obtained with an addition of 7 php of biomass to geopolymer paste containing bentonite. The paste appears discontinuous, even with the addition of supplementary water.	109
Figure 3.3.54. SEM micrograph and EDS spectra of sample C-GSP30	110
Figure 3.3.55. SEM micrograph and EDS spectra of sample C-GSP30 (annealed)	110
Figure 3.4.1. Flow curves (a) and viscosity curves (b) of pastes containing fibres	112
Figure 3.4.2. Dynamic moduli of specimens containing fibres	113
Figure 3.4.3. Creep and recovery of geopolymer pastes containing fibres	114
Figure 3.4.4. Compressive strength of geopolymers (low-bentonite formulation, containing recycled glass fibres), tested on 3D printed hollow cylinders after 7 days of ambient curing	116
Figure 3.4.5. Compressive strength of geopolymers (low-bentonite formulation, containing recycled glass fibres), tested on casted cylinders after 28 days of ambient curing.....	117
Figure 3.4.6. SEM micrograph and EDS spectra of sample C-GVF26	118
Figure 3.4.7. SEM micrographs of C-GVF26 at different magnifications	118
Figure 3.4.8. SEM micrograph and EDS spectra of sample C-GRR26; a large crack can be noticed near the aggregate	119
Figure 3.4.9. SEM micrograph and EDS spectra of sample C-GWR13	119
Figure 3.4.10. Magnification of sample C-GWR13, showing a crack.....	119
Figure 3.4.11. SEM micrograph and EDS spectra of sample LB-GRR5.....	120
Figure 3.4.12. SEM micrographs of sample LB-GRR5 at different magnifications	120
Figure 3.5.1. Flow curves of formulations containing bentonite B3.....	122
Figure 3.5.2. SEM micrograph of LB-GSP5 for scale-up, containing B3 (a) and formulated with B1 (b).....	122
Figure 3.5.3. (a) Printing process of the pipe; (b) final structure, showing a bent shape because of the structural failure occurred	124
Figure 3.5.4. Close-up on the failure point: as can be observed, the failure started in the discontinuity due to the change of layer.....	125
Figure 3.5.5. (a) Printing process of Pirelli skyscraper model; (b) result of the printing	126
Figure 3.5.6. (a) Printing process of the hollow twisted structure; (b) final result	127

Figure A 1. TGA of the alkaline activator solution	133
Figure A 2. TGA of Spirulina.....	133
Figure A 3. TGA of Tetraselmis	134
Figure A 4. TGA of red recycled glass fibres, performed on two batches	134
Figure A 5. TGA of white recycled glass fibres, performed on three batches	135
Figure A 6. XRD spectrum of metakaolin powder	135
Figure A 7. FT-IR spectrum of microalgae	136
Figure A 8. FT-IR spectra of microalgae and geopolymer before geopolymerization.	136
Figure A 9. FT-IR spectra of geopolymer and microalgae after geopolymerization ...	137

List of tables

Table 1.2.1. Comparison between Contour Crafting and D-shape AM processes [23] .	11
Table 1.2.2. Comparison between AM technologies for ceramic materials [36]	16
Table 2.1.1. Guaranteed composition of metakaolin Mefisto L05	31
Table 2.1.2. Composition of Spirulina Platensis and Tetraselmis Suecida after centrifugation	33
Table 2.1.3. Composition of residues of Spirulina and Tetraselmis	33
Table 2.2.1. Formulations of pastes for LDM 3D printing, containing biomass	36
Table 2.2.2. Formulations of pastes for LDM 3D printing, containing fibres	37
Table 2.2.3. Formulations of pastes for casting	38
Table 2.2.4. Formulations prepared to study the effect of bentonite	39
Table 2.3.1. Printing parameters used with 3DRag LDM printer	42
Table 2.3.2. Printing parameters used with Delta WASP 40100 Clay	45
Table 2.5.1. Heating ramps adopted in thermogravimetric analyses	49
Table 3.2.1. Effect of bentonite addition on rheological properties	59
Table 3.2.2. Effect of bentonite amount on compression strength of hardened cubic specimens, after 7 days of ambient curing	60
Table 3.2.3. Comparison between samples without and with bentonite: SEM micrographs and ImageJ analyses of porosity	62
Table 3.2.4. Parameters of Herschel-Bulkley's model fitted on the flow curves of geopolymer pastes, containing different types of bentonite	63
Table 3.3.1. Parameters of Herschel-Bulkley's model for HB formulations, containing biomass	66
Table 3.3.2. Compressive strength values of hardened specimens with HB formulation	69
Table 3.3.3. Compressive strength of geopolymers containing microalgal biomass, measured on cubic casted specimens after 28 days of ambient curing, annealed or not	73
Table 3.3.4. Compressive strength of geopolymers (HB, containing biomass) tested on different kinds of samples at 28 days	74
Table 3.3.5. Surface and volume of geopolymer samples, having different geometries	75

Table 3.3.6. Compressive strength values of hardened specimens with HB formulation, containing residues of Spirulina and Tetraselmis	77
Table 3.3.7. ImageJ analyses of non-annealed samples with HB formulation	89
Table 3.3.8. ImageJ analyses of annealed samples with HB formulation.....	90
Table 3.3.9. Parameters of Herschel-Bulkley's model for LB formulations, containing biomass.....	93
Table 3.3.10. Cross-over points and estimation of yield stress compared to yield stress found from flow curves	96
Table 3.3.11. Instantaneous, retarded and total recovery of pastes containing microalgal biomass (Spirulina)	98
Table 3.3.12. Compressive strength values of 3D printed hardened specimens with LB formulation, containing Spirulina (from 1 to 5 php) and Tetraselmis (5 php).....	99
Table 3.3.13. Compressive strength of geopolymers (LB, containing biomass) tested on different kinds of samples at 28 days	102
Table 3.3.14. Comparison between casted and 3D printed samples, having the same geometry.....	103
Table 3.3.15. ImageJ analyses of LB samples	108
Table 3.3.16. Compressive strength of sample with high microalgal biomass concentration (30 php)	109
Table 3.3.17. Density of samples C-GEO and C-GSP30.....	111
Table 3.4.1. Effect of fibre addition on the rheological properties (flow) of geopolymer pastes. Parameters of Herschel-Bulkley's model are reported.....	113
Table 3.4.2. Instantaneous, retarded and total recovery of pastes containing fibres.....	114
Table 3.4.3. Compressive strength values of 3D printed hardened specimens containing recycled glass fibres, tested after 7 days of ambient curing.....	115
Table 3.4.4. Compressive strength values of cylindrical casted hardened specimens containing recycled glass fibres, tested after 28 days of ambient curing.....	116
Table 3.5.1. Composition of the formulation selected for the scale-up	121
Table 3.5.2. Flow parameters of the formulation chosen for the scale-up printing, fitted according to Herschel-Bulkley's model.....	122
Table 3.5.3. Formulation actually used in the scale-up printing. The composition is slightly changed to adapt to the screw-extrusion printing process.....	123

Glossary

#

3DP Three-dimensional Printing

A

AM Additive Manufacturing

C

CAD Computer-Aided Design

D

DIW Direct Ink Writing

DLP Direct Light Processing

DM Dry Matter

DW Direct Writing

E

EDS Energy-Dispersive X-ray Spectroscopy

ESA European Space Agency

F

FA Fly Ash

FDM Fused Deposition Modelling

FT-IR Fourier Transform Infra-Red spectroscopy

G

GBFS Granulated Blast Furnace Slag

I

ICT Information and Communication Technology

L

LCA Life Cycle Assessment
LDM Liquid Deposition Modelling
LOM Laminated Object Manufacturing

M

MK Metakaolin

O

OPC Ordinary Portland Cement

P

php per hundred parts
PLA Polylactic acid

R

RP Rapid Prototyping

S

SEM Scanning Electron Microscope
SLA Stereo Lithographic Apparatus
SLM Selective Laser Melting
SLS Selective Laser Sintering

T

TGA Thermogravimetric Analysis

U

UV Ultra-Violet

W

WASP World's Advanced Saving Project
XRD X-ray Diffraction

Nomenclature of the formulations

Each formulation prepared for 3D printing is identified by an acronym, which can be generalized as **XB – GYZN**:

- **XB** represents the approach used. Specifically, it can be:
 - **HB** for high-bentonite formulations
 - **LB** for low-bentonite formulations
- **G** indicates that the material is a geopolymer
- **YZ** addresses the filler present in the mixture. It can be:
 - **SP**, i.e. Spirulina
 - **TT**, i.e. Tetraselmis
 - **LI**, i.e. lignin
 - **RS**, i.e. residues of Spirulina
 - **RT**, i.e. residues of Tetraselmis
 - **VF**, i.e. virgin glass fibre
 - **RR**, i.e. red recycled glass fibre
 - **WR**, i.e. white recycled glass fibre
 - **EO**, if no additive is present
- **N** is a number indicating the amount of filler present in the mixture, expressed per hundred parts by weight with respect to the amount of powders.

Formulations prepared for **casting** follow almost the same nomenclature rule, except for the **XB** term, that is always substituted with a **C**.

Formulations prepared to study the **effect of bentonite** follow a different nomenclature, which is simply **B – x**:

- **B** indicated that the formulation is used for the study of the effect of bentonite
- **x** is a number, indicating the amount of bentonite present in the formulation, expressed in weight percentage with respect to the whole mass of the mixture.

Further details on formulations are reported in § 2.2.

Abstract

Environmentally related problems caused by the uncontrolled industrialization in developed as well as in emerging countries, such as greenhouse gases emissions and waste disposal, are becoming of paramount importance. As a consequence, both political and technological solutions must be found as soon as possible, to deal with these global issues. Concrete industry is addressed as the cause of 5-7% of the overall human-related carbon emissions. Furthermore, its environmental impact, due to the large quantity of highly pollutant material implied, the ordinary Portland cement, is expected to grow because of the worldwide increasing request of constructions.

In this work, possible alternatives in terms of materials and processes are investigated, also taking into account the possibility of valorising wastes in a circular economy perspective. Therefore, geopolymers are selected as a greener cementitious binder in formulations optimised for liquid deposition modelling additive manufacturing technology, which is chosen for its disruptive potential of changing the paradigms of the traditional building and construction sector. In the framework of the European projects SaltGae and FiberEUUse, end-of-life microalgae used for innovative wastewater treatments and recycled glass fibres are valorised as fillers in the 3D printed materials.

A comprehensive study is developed, following the evolution stages of the material, which is prepared and printed as a liquid paste and then hardens thanks to an inorganic polymerization reaction (geopolymerization). Thus, the characterization techniques adopted encompasses rheometry, mechanical tests performed on fresh and hardened material, scanning electron microscopy (SEM) and energy-dispersive X-ray spectroscopy (EDS). Structure-properties relationships are found and discussed in sight of the applications.

Finally, printing process is scaled-up to assess the feasibility of obtaining large-scale structures. Objects with different features are printed to understand possibilities and limitations of this technology.

Estratto in lingua italiana

Temi come il cambiamento climatico e il problema dello smaltimento dei rifiuti sono sempre più al centro di ogni agenda politica e del dibattito pubblico, poiché la necessità di trovare soluzioni per salvaguardare l'intero pianeta sta promuovendo azioni legislative, iniziative sociali ed avanzamenti tecnologici. Uno dei settori maggiormente d'impatto sulle emissioni di gas serra è l'industria del cemento, che da sola è responsabile del 5-7% delle emissioni di carbonio legate ad attività umane. Il processo di produzione del cemento tradizionale Portland presenta intrinsecamente l'emissione di grandi quantità di CO₂, che va moltiplicata per la sempre crescente quantità di materiale richiesto per applicazioni edili ed infrastrutturali.

In questa tesi vengono proposte ed analizzate delle alternative agli schemi tradizionali dell'industria del cemento sia in termini di materiali, sia per quanto riguarda i processi. In sostituzione al cemento Portland è stato scelto un cemento geopolimerico a base metacaolino, più ecosostenibile, formulato per l'uso nella stampa 3D da liquido (LDM – *Liquid Deposition Modelling*), tecnologia che ha le potenzialità di rivoluzionare i paradigmi dei processi industriali tradizionali. Inoltre, materiali a fine vita, considerati rifiuti, sono stati impiegati come filler. In particolare, nel contesto dei progetti europei SaltGae e FiberEUUse, diversi tipi di microalghe usate per il trattamento di acque reflue e di fibre di vetro riciclate sono stati forniti e valorizzati all'interno delle formulazioni preparate.

L'applicazione di materiali cementizi, in particolare geopolimeri, nella stampa LDM presenta vari aspetti da controllare ed ingegnerizzare. Di fondamentale importanza è il comportamento reologico della miscela fresca, che deve essere pseudoplastico con soglia di scorrimento per garantire la regolarità del flusso, il recupero della deformazione applicata durante l'estrusione e la possibilità di sostenere i layer che vengono progressivamente depositati. In seguito alla deposizione, il materiale evolve nel tempo, andando ad indurirsi grazie alla reazione di geopolimerizzazione, che porta alla formazione di un network amorfo basato su strutture di alluminosilicati. Il tempo di indurimento è pertanto un altro fattore critico nel considerare processi che impiegano

questo tipo di materiali. Infine, le proprietà meccaniche del materiale indurito sono condizionate sia dalla composizione chimica che dalla microstruttura che viene ottenuta.

Pertanto, al fine di studiare in modo completo questo tipo di materiali e l'effetto degli additivi utilizzati su tutte le proprietà sopraelencate, varie formulazioni sono state preparate e caratterizzate.

Per quanto riguarda le proprietà reologiche, sono state svolte analisi di diverso tipo sia in regime statico sia in regime oscillatorio. Le curve di flusso ottenute in regime statico, hanno mostrato che il comportamento delle formulazioni preparate per stampa 3D è effettivamente pseudoplastico con soglia di scorrimento ed è stato modellato con successo con l'equazione di Herschel-Bulkley. Mentre il comportamento pseudoplastico è dovuto all'aggiunta della polvere di metacaolino alla soluzione dell'attivatore alcalino, di per sé newtoniana, la comparsa della soglia di scorrimento è riconducibile unicamente all'aggiunta della bentonite, utilizzata in questo studio come modificatore di reologia. La presenza di biomassa algale incide principalmente sulla soglia di scorrimento, la quale viene ridotta fino al 60% con l'aggiunta di biomassa al 3% in peso rispetto alle polveri. Di conseguenza, la stabilità del flusso risulta migliorata, pur mantenendo valori accettabili per sostenere il peso dei layer sovrastanti. Il trend di riduzione della soglia di scorrimento, con un minimo corrispondente al 3%, è stato confermato anche dall'analisi del punto di intersezione delle curve del modulo elastico e viscoso, ottenute in regime oscillatorio. L'effetto delle fibre riciclate sulla reologia è invece diverso: la soglia di scorrimento resta pressoché invariata, ma il comportamento è più vicino a quello newtoniano e la viscosità apparente inferiore. Infine, le prove di creep e rilassamento hanno mostrato l'esistenza di una finestra di stampabilità definita dalla quantità di recupero della deformazione imposta: le formulazioni stampabili mostrano infatti un recupero istantaneo della deformazione attorno al 10%, mentre quelle non stampabili si attestano fra lo 0% e il 5%.

Il materiale fresco è stato testato anche mediante prove di compressione, per analizzare l'evoluzione delle proprietà meccaniche nei primi stadi dell'indurimento. Si è osservato che i campioni contenenti biomassa induriscono più velocemente della formulazione di riferimento senza filler. Sottraendo acqua alla soluzione dell'attivatore, la biomassa agisce pertanto da accelerante della reazione di geopolimerizzazione.

Le proprietà meccaniche dei campioni induriti stampati in 3D e ottenuti per casting sono state testate dopo 7 e 28 giorni di curing a temperatura ambiente. Il processo di stampa non incide direttamente sulle proprietà meccaniche, ma l'aggiunta di bentonite necessaria per ottenere le proprietà reologiche desiderate va ad influire negativamente sulla resistenza a compressione, ridotta di oltre il 50%. Formulazioni con minore contenuto di bentonite hanno infatti mostrato proprietà meccaniche migliori, tutte all'interno dell'intervallo normativo per applicazioni ordinarie di 16 MPa – 45 MPa. Il valore di 45 MPa è stato superato da alcune formulazioni, applicando un trattamento termico a temperatura costante di 800 °C per 4 ore. Inoltre, nella maggior parte dei casi si è dimostrato che il plateau di massime proprietà meccaniche viene già ottenuto dopo 7 giorni. L'aggiunta di biomassa algale come di fibre riciclate non risulta influenzare in modo significativo le proprietà meccaniche; il lieve calo del valor medio di resistenza a compressione osservabile per i campioni contenenti microalghe è infatti compreso all'interno dell'intervallo di deviazione standard. Pertanto, tali materiali possono essere efficacemente usati come filler fino ad aggiunte rispettivamente di 5 php e 10 php in impasti per stampa 3D. Concentrazioni maggiori portano a riduzioni più significative delle proprietà meccaniche o a difficoltà nell'ottenere impasti omogenei e stampabili. L'utilizzo della lignina come filler, utilizzata come biomassa di confronto, ha invece portato ad una riduzione molto più accentuata dei valori di resistenza a compressione.

Il principale effetto della biomassa sulla microstruttura è la creazione di pori e la conseguente riduzione della densità, come dimostrato dalle immagini ottenute mediante microscopia elettronica a scansione (SEM). Tali analisi hanno anche dimostrato che i campioni sono in generale omogenei e non mostrano segni dovuti al processo di stampa né aggregazioni riconducibili agli additivi utilizzati. Inoltre, il confronto fra provini trattati termicamente e non, ha permesso di capire che l'effetto della cottura è principalmente quello di ridurre le porosità ed uniformare ulteriormente la matrice. Tramite l'analisi microstrutturale è stato quindi possibile legare le variazioni delle proprietà meccaniche principalmente a due fattori, ovvero la porosità e la minore resistenza della bentonite, che causano la presenza di punti di debolezza nella struttura solida ottenuta.

La maggior parte delle stampe, tramite cui sono stati prodotti i campioni per le prove meccaniche, è stata condotta utilizzando una stampante desktop 3DRag (volume di

stampa 20 cm x 20 cm x 20 cm), adattata alla tecnologia LDM. Una volta ottimizzato il processo, si è proceduto ad uno scale-up con una stampante WASP Delta 40100 (volume di stampa 40 cm x 40 cm x 100 cm), per verificare la fattibilità di stampare strutture a scala maggiore. Sono stati stampati tre oggetti dalle caratteristiche differenti, al fine di verificare i pregi e le limitazioni della tecnologia LDM. I risultati hanno dimostrato che possono essere stampate strutture dalle forme complesse, al patto che siano leggere e con sbalzi non eccessivamente pronunciati. L'ottenimento di una buona rifinitura superficiale e la resa dei dettagli è legata alla scelta dell'ugello rispetto alle dimensioni della struttura. La principale limitazione della stampante utilizzata è la l'alimentazione a serbatoio, che, unita al progressivo indurimento del materiale, ha imposto pause durante la stampa, con conseguenti errori visibili anche nei pezzi finiti.

Aim of the thesis

In the framework of the European Union's projects SaltGae and FiberEUse, the aim of this work is to prepare and characterize geopolymer formulations for 3D printing applications, loaded with recycled materials.

SaltGae project is developing an economically and technologically viable solution to treat saline wastewaters with algal biomass. Dealing with end-of-life biomass is an important part of the project, which is addressed in this work. Microalgal biomass is compared in this thesis with lignin. Lignin is another biomass which represents a waste in pulping industry.

FiberEUse is focused on the recycle of glass fibre components. The recycled fibres are used in this work as fillers and their effect is compared to that of virgin glass fibres.

The characterization of the materials encompasses the study of rheology, mechanical properties and microstructure, to give a comprehensive description useful for the final applications mainly in building and construction industry

1. Introduction

1.1. Overview on additive manufacturing

1.1.1. Definition and classification of additive manufacturing

The functionality of a manufactured object is derived from the combination of geometry and materials' properties. According to ISO/ASTM 52900:2015(E) [1], the shaping of materials into objects can be achieved by one, or by a combination of three basic principles:

- Formative shaping: the shape is obtained by the application of pressure to a body of raw material;
- Subtractive shaping: the shape is acquired by the selective removal of material;
- Additive shaping: the shape is given by successive addition of material.

Manufacturing processes based on additive shaping are included in the category of additive manufacturing (AM), also designated as solid freeform fabrication (SFF), Rapid Prototyping (RP), or, popularly, 3D printing.

Many 3D printing processes have been developed starting from the 1980s, and several different classifications of them have been proposed. In the aforementioned ISO/ASTM standard, additive manufacturing processes are sorted in seven categories: binder jetting, direct energy deposition, material extrusion, material jetting, powder bed fusion, sheet lamination and vat photopolymerization.

Binder jetting consists in selectively spreading a binding agent onto a ceramic or metal powder bed to build a part one layer at a time. The most famous technique following this approach is called three-dimensional printing (3DP). For the fabrication of each layer, a layer of powder material is spread on top of the build platform and a printhead selectively deposits certain amount of binder droplets at designated locations of the powder bed. After binder deposition, the entire powder bed surface can be subjected to external heating applied via a radiation heat source in order to partially cure the binder and ensure adequate mechanical strength for consequent printing processes. After the

drying/curing, a new layer of powder will be added to the powder bed, and this sequence of actions repeats until the entire part is printed. At the end of printing process, the parts are in a green state and require additional post-processing before they are ready to use [2]. Binder jetting steps are schematized in Figure 1.1.1.

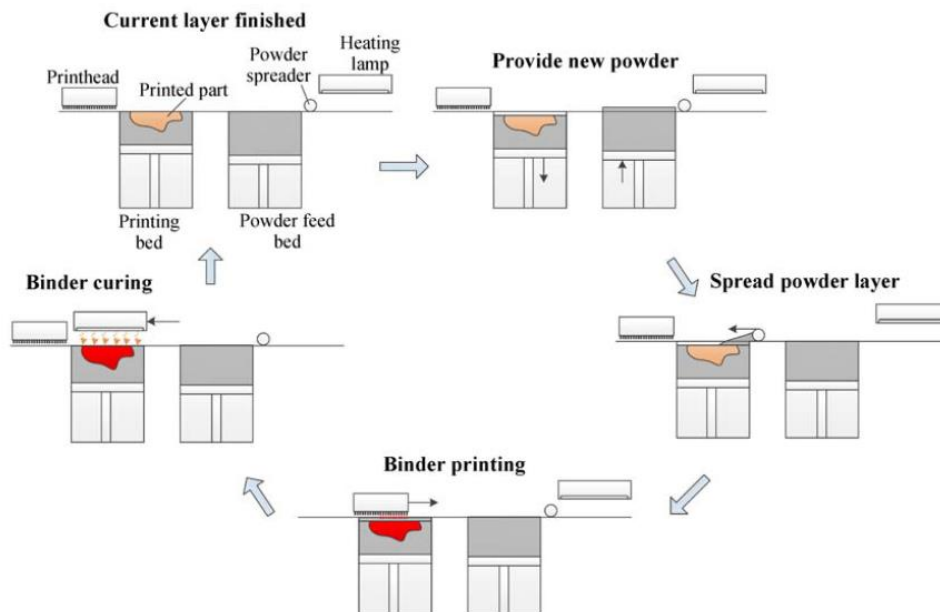


Figure 1.1.1. Schematic diagram of binder jetting process [2]

Direct energy deposition exploits a source of energy (laser or electron beam) directly focused on a small region of the substrate to melt a feedstock material (powder or wire) along with the substrate itself. The melted material is deposited in layer-by-layer fashion and fused into the melted substrate; solidification occurs after the movement of the energy beam. Usually, this technique is used for manufacturing or repairing large components with low complexity, made by metallic materials (even super-alloys) [3].

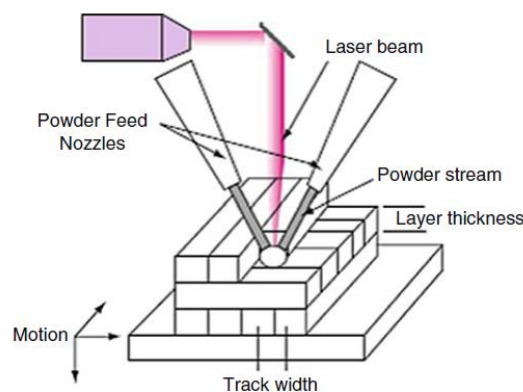


Figure 1.1.2. Schematic diagram of a typical direct energy deposition process [4]

Material extrusion techniques are based on the extrusion of material through a nozzle. Fused deposition modelling (FDM), the most known and widespread 3D printing technology, falls in this category. In this process, the material, typically plastic fed by a filament, is heated to a temperature slightly above its melting point within the head, then it is extruded through a nozzle to a substrate and cooled down until it solidifies. The main limitation of FDM technology, which is the possibility to print only thermoplastic materials, has been overcome by direct writing (DW) technologies, like Robocasting, direct ink writing (DIW) and liquid deposition modelling (LDM). In all these technologies the liquid deposited is not a molten polymer, but a liquid material at ambient temperature. Being heating and melting not involved, the layer-by-layer formation a free-standing structure relies only on a proper control of the rheology of the paste [5]. By DW, ceramic and cementitious materials can be printed (§ 1.2). Recently, a modified version of LDM has been proposed to print photo-crosslinking resins, and composites based on them, by exploiting UV-radiation. In this technique, called UV-assisted 3D (UV-3D) printing, the feed material is cured at room temperature right after exiting the extrusion nozzle by means of UV-light irradiation [6].

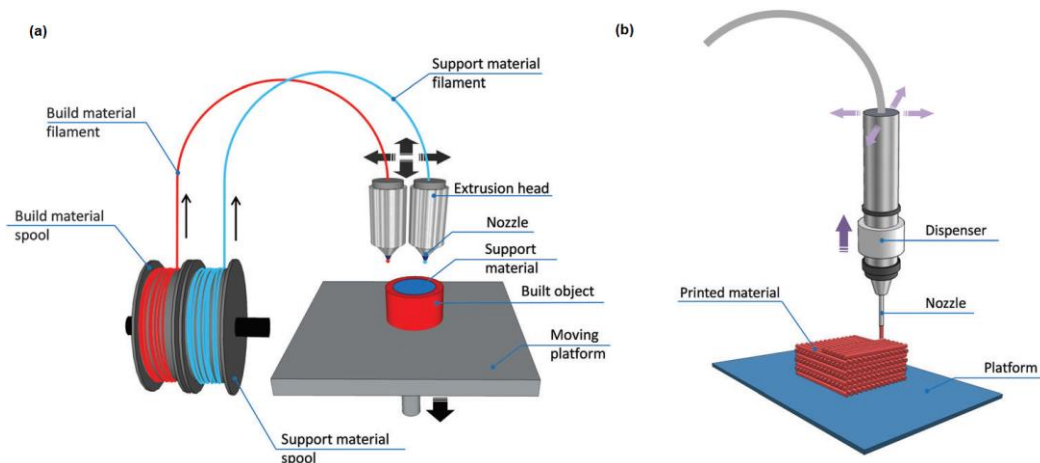


Figure 1.1.3. Schematic representation of FDM (a) and DW (b) systems [7]

Material jetting is often compared to the 2D ink jetting process. Viscous materials, like photopolymers and waxes, are typically used thanks to their ability to form drops. 3D models are created through the use of movable inkjet print heads that jet the material onto a build platform (Figure 1.1.4). To facilitate jetting, viscosity is reduced through heating or by using solvents. Curing is performed via UV-radiation or thermal treatment, depending on the material [8].

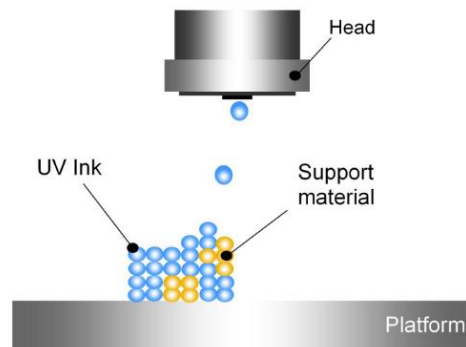


Figure 1.1.4. Scheme of material jetting process [8]

Powder bed fusion processes consist in a bed of powder, typically metallic, which is selectively sintered or melted by a high energy source (laser or electron beam). To form the 3D object, layers of powder are subsequently rolled on the previous one and fused together. Size distribution and packing of the powder bed are the most important parameters which determine the density of the printed part. Depending on the powder material, different techniques can be used: while selective laser melting (SLM) is carried out on metals with low melting temperature, typically aluminium and some steels, selective laser sintering (SLS) is adopted for a variety of polymers, metals and alloy, which can be sintered in the same range of temperatures [3].

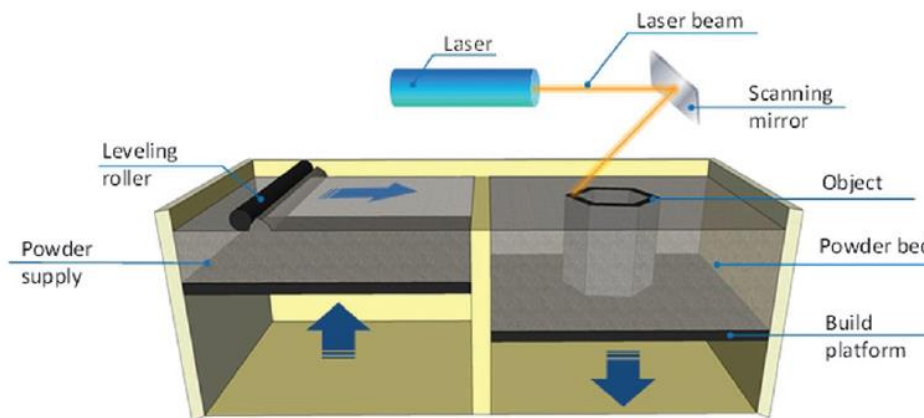


Figure 1.1.5. Schematic representation of powder bed fusion AM process [7]

Sheet lamination, also known as laminated object manufacturing (LOM), involves the stacking of laminated materials on top of one another after a layer contour definition has been achieved by cutting tools. For each layer, a sheet of material is loaded onto a stage and then undergoes the cutting process, done by laser or blade, which defines the contour according to the CAD model. After the removal of the excess of material, the process is repeated for the subsequent layer. Each layer is bonded to the previous one by

using adhesives or welding techniques. Every material which is available in sheets can be processed by this technique [7].

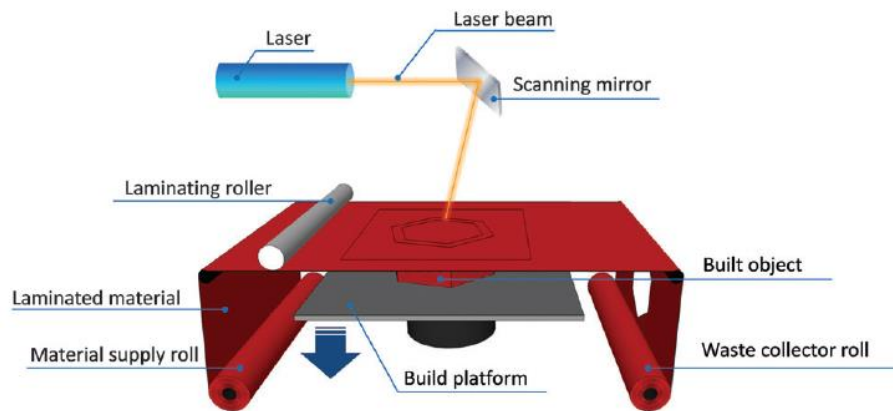


Figure 1.1.6. Scheme of sheet lamination AM process [7]

Vat photopolymerization is the AM process in which liquid photopolymer in a vat is selectively cured by light-activated photopolymerization (usually by UV-radiation). One of the earlier developed AM techniques is stereolithography (SLA). In SLA the build platform is submerged in the photopolymer resin. A single point laser located inside the machine maps the layer through the bottom of the tank, solidifying the material. After the layer has been completed and solidified, the platform lifts up and lets a new layer of resin flow beneath the part. This process is repeated until the completion of the object. Very high resolutions, depending on the focalized UV light beam, are obtained. An alternative approach is represented by direct light processing (DLP). In DLP light is projected over a mask, which reports the shape of a whole layer. So, differently from SLA, which creates the layer pointwise, with DLP an entire layer is obtained at once [9], [10].

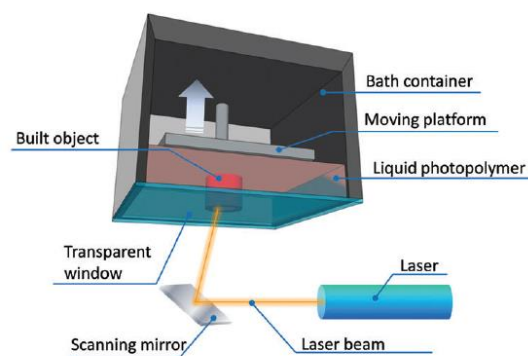


Figure 1.1.7. Schematic representation of SLA [7]

1.1.2. Generalized additive manufacturing process chain

Additive manufacturing is a digital technology, since a designed object can be directly manufactured without passing through the production of a mould. This process can be always schematized in eight steps [9]:

- 3D modelling
- conversion to STL
- transfer to AM machine and STL file manipulation
- machine setup
- build
- removal
- post-processing
- application

A 3D solid model is the starting point for the production of any AM part. It can be obtained by computer aided design software (CAD) or by reverse engineering equipment, such as 3D scanning and photogrammetry.

The conversion to STL file removes construction data and modelling history and approximates the outer surfaces with a series of triangles (mesh). This process introduces a certain degree of inaccuracy, which is directly proportional to the size of the mesh.

The STL file is then sliced, transforming the continuous contour into discrete stair steps. Then, once sliced, the file is converted in a G-Code, which is composed by the series of commands (tool path) the machine has to follow to perform the printing. G-Code can include some machine setups, which in some cases can be also manually controlled directly from the user interface.

At this point, after having set the machine and charged the material, printing process can take place. The subsequent steps listed are highly dependent on materials and technology implied, as well as on the final application. Post-processing can include the removal of supports, thermal or chemical treatments, surface machining, application of glazes, coating etc. [7], [9], [11].

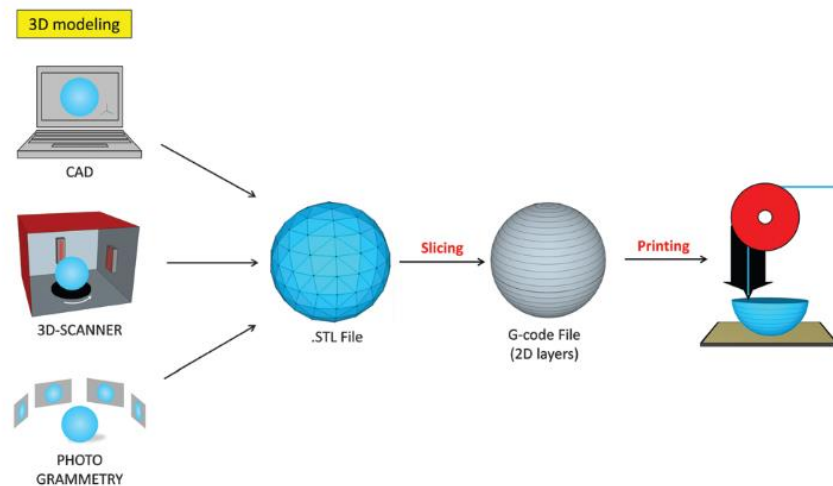


Figure 1.1.8. Scheme of a general AM process [7]

1.1.3. Past, present and future of additive manufacturing

Although 3D printing is commonly considered as a recent technology, the first patent was filed in 1986 by Charles Hull, who invented the SLA system and then co-founded the company “3D System” [7].

Starting from that moment, 3D printing has undergone a three-phase evolution process. At the beginning, AM was intended just as rapid prototyping, to produce prototypes and mockups of new designs in a quicker and cheaper way. Thanks to the low costs of modifying prototypes, marketers could more easily test different product versions based on customer and design feedback. In the second evolutionary phase, 3D printing became an instrument used to create finished goods, rather than just prototypes. According to Terry Wohlers, manager of a market resource firm specializing in 3d printing, over 20% of the output of 3D printers is now in final products as opposed to prototypes, and this ratio will rise to 50% by 2020. In the third phase, which is at its beginning, 3D printers are owned by final consumers, just like personal computers or traditional “2D” printers [12].

The last passage has been made possible by the low-cost and the relatively ease of use of the most recent 3D printing technologies, especially FDM. A vibrant community of 3D printing enthusiasts started sharing ideas and improving low-cost technologies, both online and “offline”, in the so called “hackerspaces”, “makerspaces” and “fab labs” [13]. Projects such as RepRap and Fab@home paved the way, starting from the beginning of 2000s, to an open-source culture related to 3D printing, which moved the market,

reducing furtherly the costs of the entry-level machines, as well as people's attention and expectations on this technology [4].

This phenomenon can be perfectly inserted in the larger framework of frugal innovation. Frugal innovation is defined as the process by which “luxury” features are obtained at low cost [14]. The term, coined in India, is directly linked to the ability of making high value-added goods even with scarce resources, to meet the needs of low-income customers. Redefining traditional manufacturing, 3D printing has the potential to improve lives and to integrate those who were previously excluded from the formal economy. By integrating the poor into the formal economy it can improve their standard of living, leading to a positive and sustainable impact on economic empowerment, social development and democratization [15].

Along with all these benefits, relatable to a socioeconomic perspective, there are also many technical advantages of additive manufacturing with respect to traditional manufacturing technologies. In comparison to traditional formative and subtractive shaping techniques, such as injection moulding, casting and stamping, higher part complexity can be achieved, obtaining shapes that are impossible or very difficult to produce traditionally, as well as built-in interlocked object with no need of assembly (Figure 1.1.9). While in metal casting and injection moulding, each new product requires a new mould and in machining several tool changes are needed to create the finished product, AM is a “single tool” process. Thanks to this aspect, AM is perfect to create objects with customized and complex geometries. Moreover, since material is added layer-by-layer, wastes are dramatically reduced [16].

Nonetheless, some intrinsic limitations of AM processes make them not suitable for certain applications. The low speed to produce similar products in series, if compared for example to injection moulding, makes it unsuitable for large standardized production. Fine dimensional control and the possibility to manufacture a large variety of materials were limitations that are now going to be overcome by research on materials and optimization of machines [16].

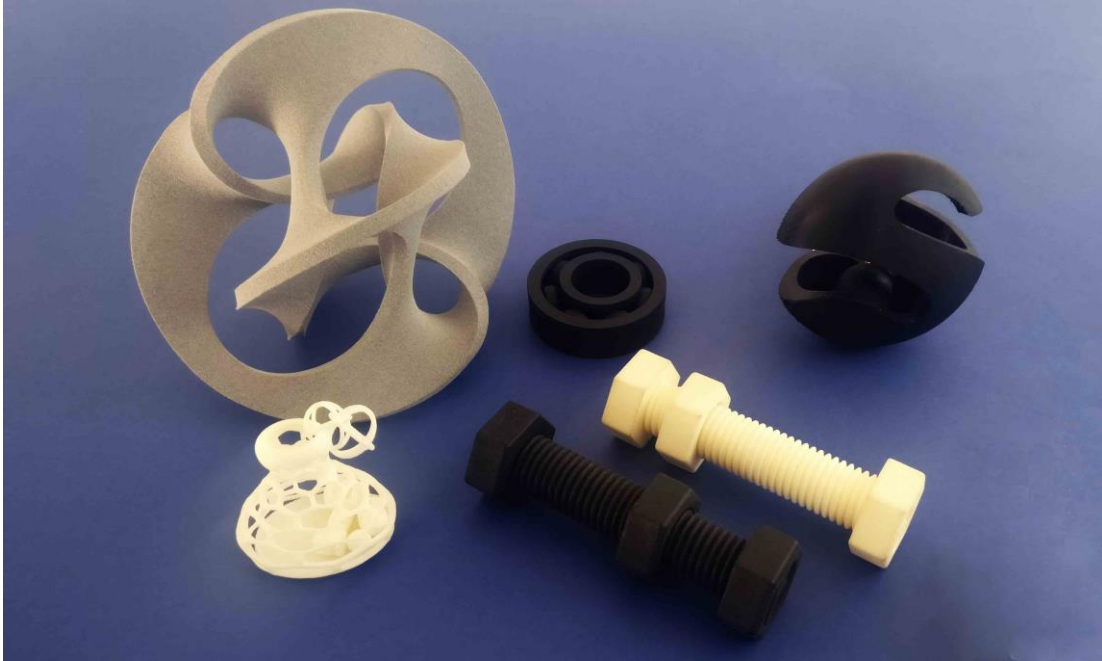


Figure 1.1.9. Examples of objects which are impossible to produce (in one piece) by traditional manufacturing techniques [17]

1.2. Additive manufacturing of cementitious and ceramic materials

Geopolymers, which are the materials studied in this work, have been proved to be suitable both as cementitious and as ceramic materials. Up to now, the primary area of application of geopolymer technology is in the development of reduced-CO₂ construction materials as an alternative to Portland-based (calcium silicate) cements. Other applications for geopolymers include as a host matrix in waste encapsulation, as a low-cost ceramic (either used directly or as a precursor for calcination), and in fire protection of structures [18].

Taking into account these areas of application, in the following paragraphs an overview on additive manufacturing of cementitious and ceramic materials is provided. Geopolymer chemistry and technology are described in §1.3.

1.2.1. Building and construction

Many attempts have been conducted to explore the potential of 3D printing in the building and construction industry. In 1997 the first attempt of cement-based AM was made by Joseph Pegna in Rensselaer Polytechnic Institute (USA) [19]. Concrete components were manufactured by depositing layers of sand and of cement paste, used to selectively glue the sand together. Layers were compressed and then steam was applied

to obtain rapid curing. In 1998, professor Berokh Khoshnevis [20] at the University of Southern California (USA) developed a cementitious material AM process called “Contour Crafting”, which later has become an effective method to print real-life houses. Contour crafting is a direct writing AM technique, that can construct large scale components (even buildings) by extruding cementitious materials through a gantry-driven nozzle without using extra formworks. Smooth planar surfaces can be obtained by using a top and a side-trowel attached to the extruder [21]. In general, four key parameters has to be taken into account when dealing with cement extrusion-based processes [22]:

- pumpability: the ease and reliability with which material is moved through the delivery system;
- printability: the ease and reliability of depositing material through a deposition device;
- buildability: the resistance of deposited wet material to deformation under load;
- open time: the period where the above properties are consistent within acceptable tolerances.

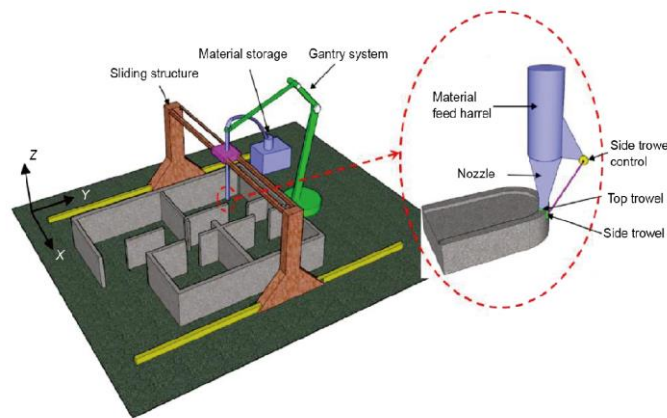


Figure 1.2.1. Schematic representation of large- scale Contour Crafting [23]

In 2007, the Italian engineer Enrico Dini invented and patented a largescale powder-based 3D printer, named “D-shape”, which is based on the use of sand and an inorganic binder with 5–10 mm of the layer depth [24].

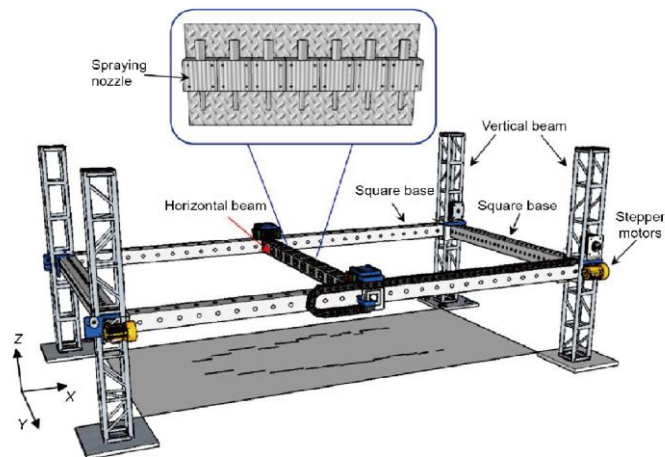


Figure 1.2.2. Schematic representation of D-shape processes [23]

All the large-scale 3D printing processes developed until now are mainly based on Contour Crafting and D-shape approaches, adopted with slight variations. Table 1.2.1 summarizes the main differences between these two processes.

Table 1.2.1. Comparison between Contour Crafting and D-shape AM processes [23]

	Contour-Crafting	D-shape
Process	Extrusion-based	Selective binding
Support	Vertical: no Horizontal: lintel	Unused powder
Material	Cementitious material	Sand
Printing resolution	Low	High
Layer thickness	13 mm	4-6 mm
Print head	1 nozzle	Hundreds of nozzles
Nozzle diameter	15 mm	0.15 mm
Printing speed	Fast	Slow
Printing dimension	Mega-scale	Limited by frame (max 6 m x 6 m x 6 m)

Large-scale printings using both techniques are present in literature. Contour-crafting has been successfully applied in in-site applications. In 2014 Andrey Rudenko built an entire castle, using a mix of cement and sand. Whole building was printed on a single run, except of towers, that were printed separately and assembled to the building [23].



Figure 1.2.3. Castle printed in-situ by Andrey Rudenko [25]

In the same year, WinSun, a company in China, built ten houses in Shanghai using a gigantic 3D printer (150 m×10 m×6.6 m) within 24 h. Each building (200 m² floor area) was entirely created by high-grade cement and glass fibres. After that, they built the highest 3D printed building, a five-story apartment and the world’s first 3D printed villa, whose parts were printed in a factory and then assembled together to create whole construction [25].



(a)



(b)

Figure 1.2.4. Structures printed by WinSun: house (a) and five-story apartment (b) [25]

In 2015, the Italian company WASP (World’s Advanced Saving Project) created a 12 m tall 3D printer (“BigDelta”) to study the possibility of producing houses with raw materials available on the printing site, like clay and straws. A structure developed 2.7 m in height and 5 m in diameter was printed, by an extrusion-based process (Figure 1.2.5). In 2018 a new printing system, “Crane”, was introduced. Differently from “BigDelta”, Crane is formed by printing moduli, each having a print volume of 6.60 m in diameter and 3 m in height (Figure 1.2.6 a). With this configuration is theoretically possible to cover any surface just by adding ties and print arms to the module, so making feasible the

possibility of printing simultaneously entire villages. WASP first tested “Crane” with the construction project called Gaia, a house printed in 3D from a mix of earth, straw and compost [26].

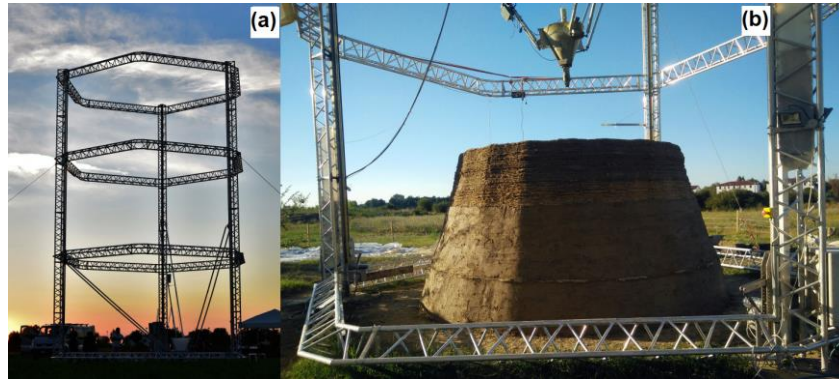


Figure 1.2.5. (a) BigDelta machine by WASP and (b) 3D printed structure [27]

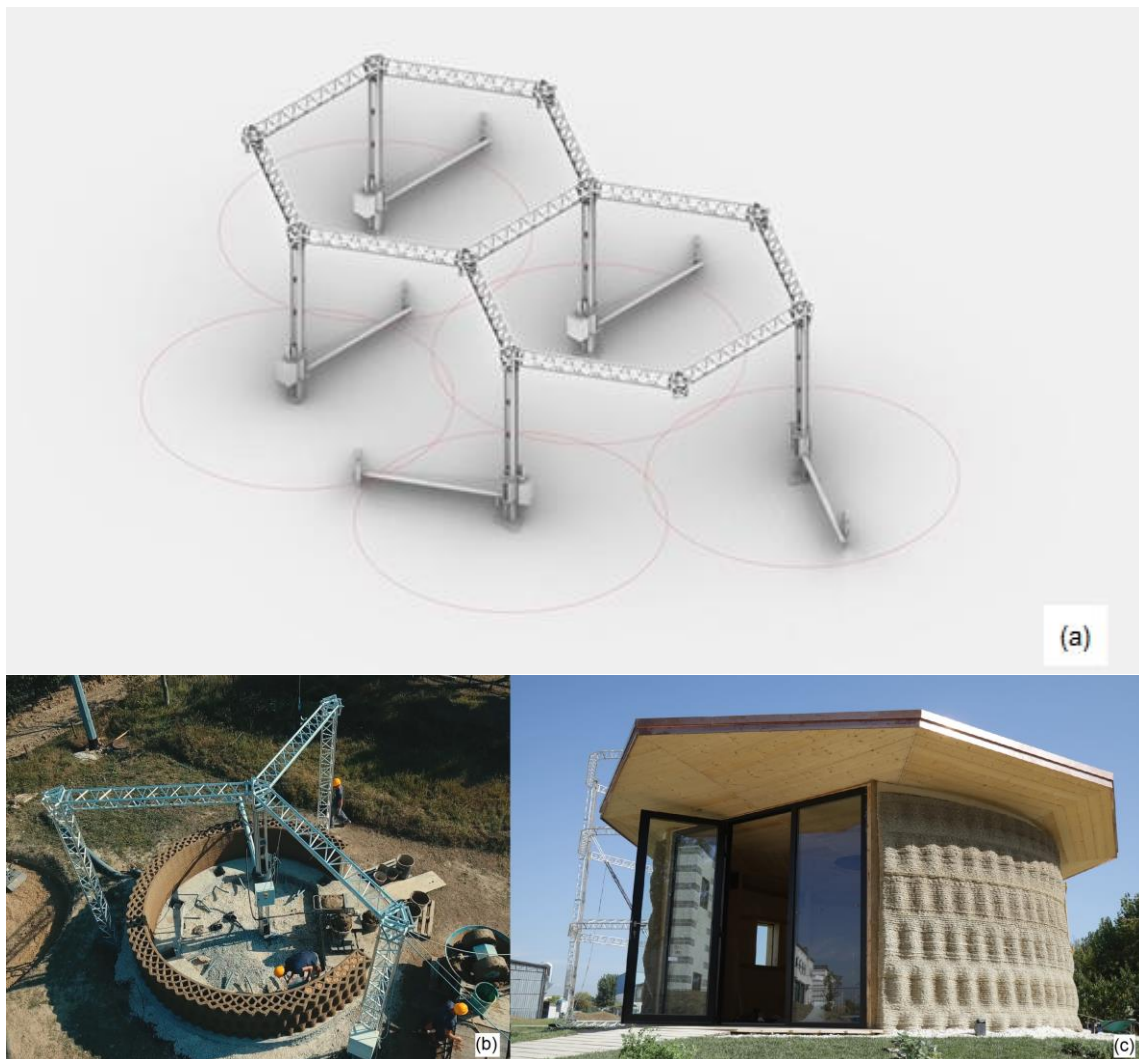


Figure 1.2.6. Crane by WASP: (a) blueprint of the modular structure, (b) printing process, (c) final printed structure (Gaia), with added windows and roof [27]

WASP trial of using materials alternative to Portland cement is the only one reported in literature for large-scale structures. Studies on 3D printing of greener building materials are at their first stage. One example is represented by the group of Biranchi Panda and his co-workers, who published many papers on 3D printed fly ash-based geopolymers for building and construction applications [28]–[31].

D-shape was used to build large-scale structures, too. In 2008, designer Andrea Morgante printed an urban temple project for the city hall of Pontedera (Pisa), with a size of 3 m x 3 m x 3 m. In 2010 a complete house was printed in one single printing [23]. Because of the high resistance of the built structures, the feasibility of using this technique for building a lunar outpost was studied in a project funded by the European Space Agency (ESA). Demonstrators of structural components have been successfully printed with a clayey material which simulated the lunar sand [32].

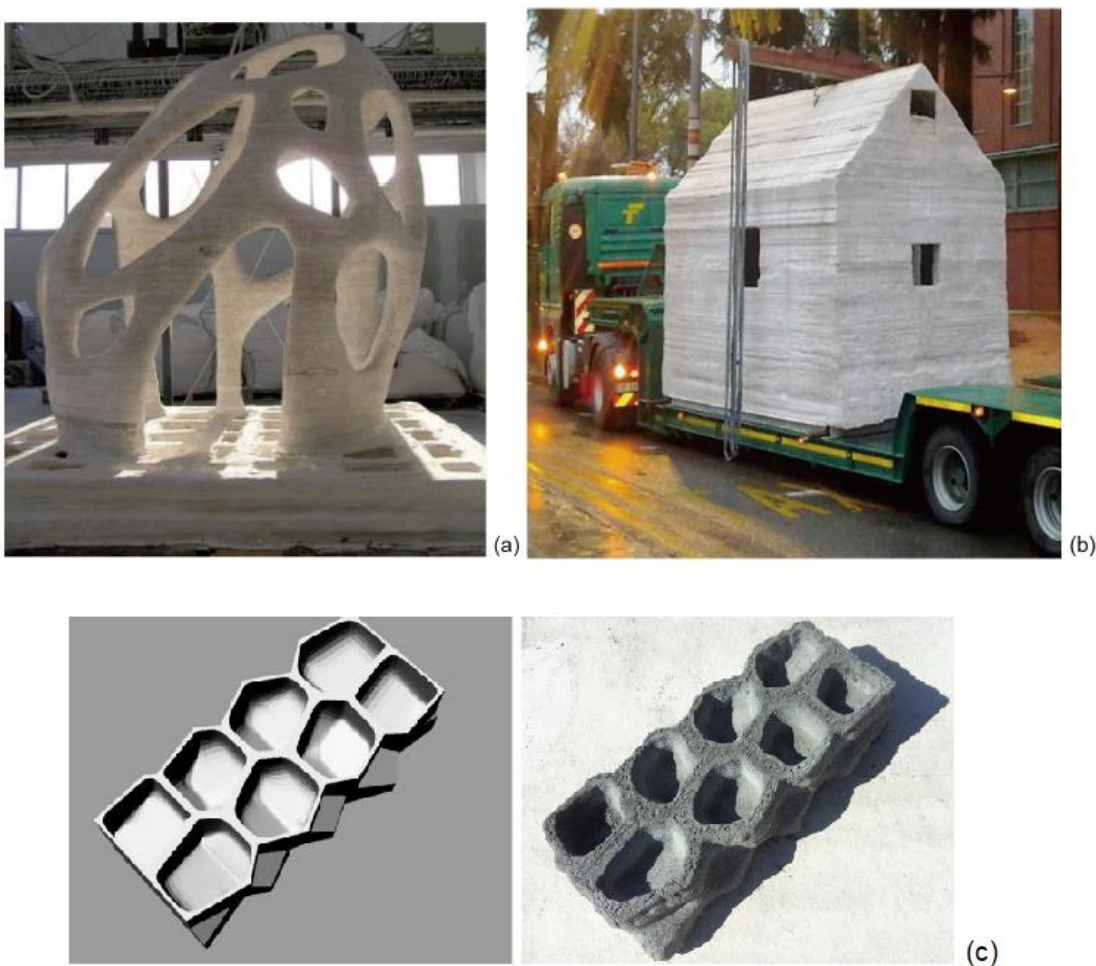


Figure 1.2.7. Structures obtained by D-shape technique: (a) project for the city hall of Pondera, (b) complete house, (c) CAD and actual printed part of a structural block designed for a lunar outpost

Large-scale 3D printed structures can be also obtained by printing small parts, which can be assembled in situ afterwards. This approach, sometimes called “concrete printing”, enables higher freedom of design and precision of manufacturing, better foreseeing functional integrations like reinforcements [22].

Several benefits can come from large-scale 3D printing of cementitious materials. As all AM technologies, since material is added layer-by-layer, wastes are reduced to the minimum and self-standing structures can be obtained without the need of formworks. Being an automated technology, lower manpower is needed, so costs can be potentially reduced. Moreover, a high degree of flexibility in design can be introduced in a sector which traditionally is characterized by standardization. On the other hand, since this technology is at its infancy stage, some issues are yet to be overcome. Life cycle performances of built structures are still unclear, as well as market response to this technology [33]. In addition, reinforcements must be completely redesigned with respect to traditional concrete technology, since no casting is performed. The direct in-print entrainment of reinforcement cable into the concrete filament during printing is still at a research level [34].

1.2.2. Other fields of application

Enabling the fabrication of very complex shapes, AM can make a breakthrough in ceramic and concrete industry, which has been technologically underdeveloped for many years [35]. Applications of AM of ceramics different from building and construction can be divided mainly in two classes: production of porous structures and of dense monolithic bodies. It is well-known that most of the AM technologies successfully applied to the manufacture of ceramics have been used to fabricate porous structures, for example, scaffolds for biological applications, filters, lightweight structures etc. In these cases, a certain amount of random and residual porosity in the solid ceramic part is tolerated or even desired, as it provides further functionality to the component. On the other hand, there are very few AM technologies on the market capable of generating fully dense monolithic ceramic bodies. AM of monolithic ceramics, enabling the components to fully retain their superior physico-chemical properties, is still a challenge and remains the most important task that needs to be solved to promote AM of ceramics to more than a niche technology [36].

Differently from building and construction applications, where the large scale limits the possible applicable techniques, for AM of ceramic materials almost all the approaches described in § 1.1 can be adopted. Table 1.2.2 summarizes the main features of all AM technologies applied to ceramics.

Table 1.2.2. Comparison between AM technologies for ceramic materials [36]

Technology	Feedstock	Part dimension (orders of magnitude)	Surface quality of parts	Overall cost (feedstock and process)
Powder-based 3D printing	Powder	10 mm – 1 m	Medium	Medium
Powder-based selective laser sintering	Powder	10 mm – 0.1 m	Medium	High
Stereolithography	Suspension of ceramic particles in a liquid polymeric binder	100 μ m – 10 mm	High	Medium-high
Slurry-based 3D printing	Liquid (slurry)	10 mm – 1 m	High	Medium
Laminated object manufacturing	Green ceramic tapes	10 mm – 0.1 m	Medium	Medium
Direct inkjet printing	Low viscosity suspension	1 mm – 10 mm	Medium	Medium-high
Direct ink writing/liquid deposition modelling	Liquid (paste)	1 mm – >1 m	Low	Low
Fused deposition modelling	Polymeric filament loaded with ceramic powder	1 mm – 10 mm	Low	Medium

1.3. Geopolymers

Inorganic polymers, more commonly referred to as “geopolymers” or alkali-activated cements, are alumino-silicate materials which exhibit excellent physical and chemical properties and a diverse range of potential applications, including precast structures and non-structural elements, concrete pavements and products, containment and immobilisation of toxic, hazardous and radioactive wastes, advanced structural tooling and refractory ceramics, and fire resistant composites used in buildings, aeroplanes, shipbuilding, racing cars, and the nuclear power industry [37].

The name “geopolymer” was coined in 1972 by the French chemist Davidovits to identify ceramic materials which are formed by inorganic polymerization of mineral raw materials typically coming from geological sources [38]. The principal means of synthesising geopolymers is to combine an alkaline solution with a reactive aluminosilicate powder. This results in the formation of a disordered alkali aluminosilicate gel phase, known as the geopolymeric gel binder phase [18].

Raw materials can be natural (alumino-silicate) minerals or industrial wastes such as fly ash, slag, waste glass [39] and rice husk [40]. In particular, metakaolin (MK) is a thermally treated product from kaolin, which is one of the naturally occurring abundant minerals in the earth's crust [41].

In the following paragraphs, the most important aspects of geopolymer chemistry and the technology, as well as the future perspectives, are presented and discussed.

1.3.1. Geopolymerization

The reaction leading to the formation of the geopolymer network is a polycondensation, occurring in different steps, by a still controversial reaction scheme. The basic steps of geopolymerization involve dissolution in alkaline environment of solid alumino-silicate oxides in MOH solution (where M is an alkali metal), diffusion or transportation of dissolved Al and Si complexes from the particle surface to the inter-particle space, formation of a gel phase resulting from the polymerization between added silicate solution and Al and Si complexes and finally hardening of the gel phase [42]. The separation between these steps is not clear: the reactions probably occur simultaneously once the solid material is mixed with liquid activator. Therefore, the aforementioned

separation has just a thermodynamic meaning [43]. Figure 1.3.1 reports the chemical equations related to the different steps of geopolymerization.

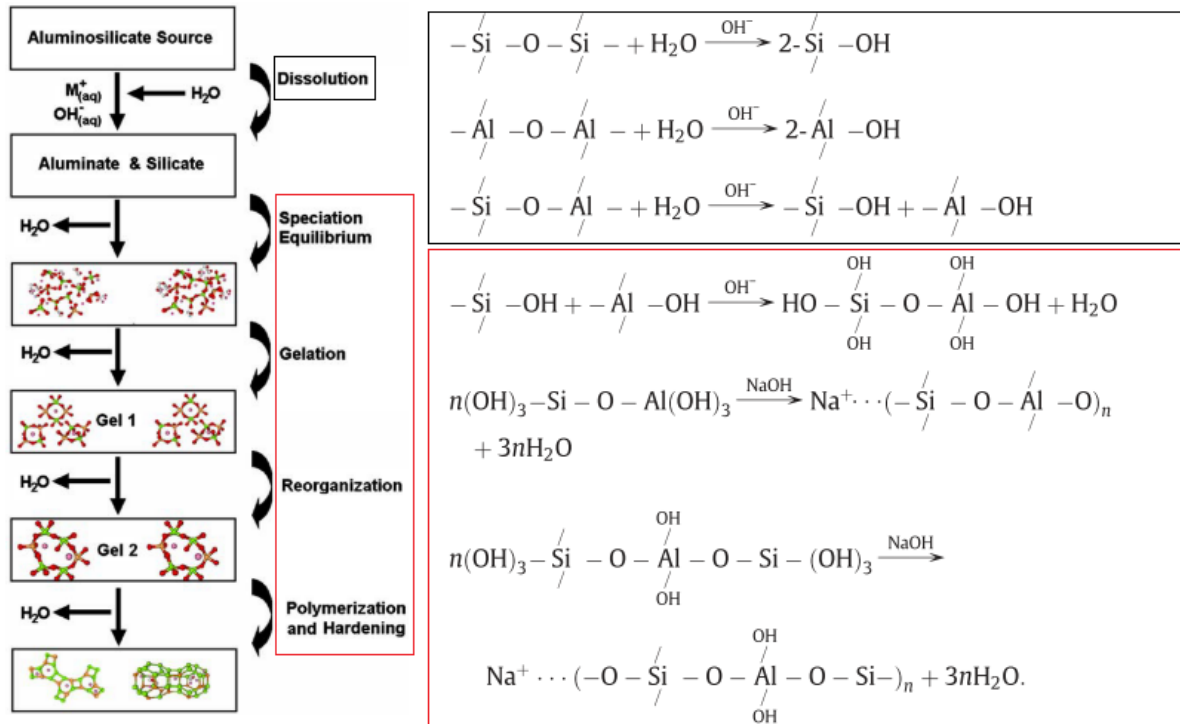


Figure 1.3.1. Different steps of geopolymerization, divided in two groups: dissolution (in black box) and condensation/gel formation (in red box). Adapted from [44] and [43]

The result of geopolymerization is a sialate (silicon-oxo-aluminate) network consisting of SiO_4 and AlO_4 tetrahedra linked alternately by sharing all oxygen atoms. Positive ions such as Na^+ , K^+ and Ca^{2+} must be present in the framework cavities to balance the negative charge of Al^{3+} . Poly(sialates) are chain and ring polymers with Si^{4+} and Al^{3+} in 4-fold coordination with oxygen and their empirical formula is displayed as $\text{M}_n(-(\text{SiO}_2)_z-\text{AlO}_2)_n \cdot w\text{H}_2\text{O}$, where z is 1, 2 or 3, M is a monovalent cation such as K^+ or Na^+ and n is the degree of polycondensation. The overall structure can be amorphous or semi-crystalline, consisting of chains, sheet-like and three-dimensional networks [37], [45]. Figure 1.3.2 shows the three types of polysialates identified by Davidovits [46] and sketches of the possible 3D networks that can be formed in the geopolymer structure.

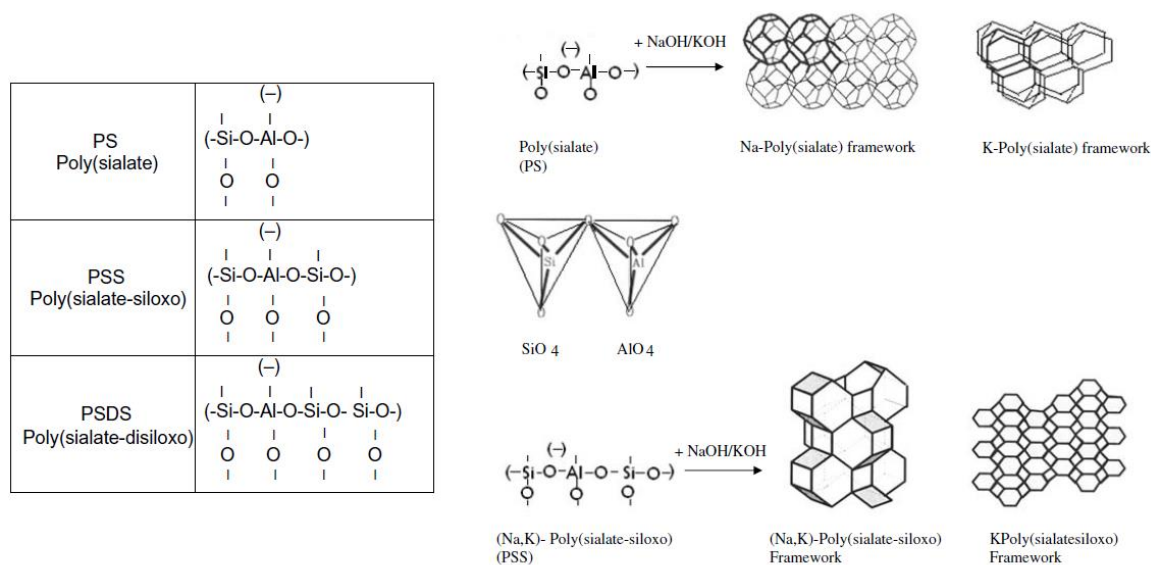


Figure 1.3.2. Types of poly-sialates and their structures. Adapted from [37] and [44]

1.3.2. Factors affecting geopolymer properties

The setting process and the final microstructural and mechanical properties of geopolymers are affected by the chemical composition and by external parameters, such as pH and temperature.

Setting time is mainly controlled by the alumina content and increases with increasing $\text{SiO}_2/\text{Al}_2\text{O}_3$ ratios in the initial mixtures [47]. $\text{SiO}_2/\text{Al}_2\text{O}_3$ ratio affects also mechanical properties: mixtures containing high content of alumina (i.e. low $\text{SiO}_2/\text{Al}_2\text{O}_3$ ratio) display lower mechanical properties in general. Duxson et al. found that compressive strength of metakaolin based geopolymers linearly increases by approximately 400% from $\text{Si}/\text{Al} = 1.15$ to $\text{Si}/\text{Al} = 1.90$. Higher Si/Al ratios shows lower mechanical properties because of unreacted raw material, which acts as weaker points [48].

Alkali cations have an important role, as well. According to Van Jaarsveld, alkali metal cations control and affect almost all stages of geopolymerization and in particular during gel hardening and crystal formation, cations contribute to the structure formation of geopolymers [49]. In geopolymerization, the alkali metal content of reacting minerals could have a significant effect on strength development in contrast to concrete manufacture where the presence of alkali metals is undesirable due to stresses developed by alkali activation [42]. The size of the cation also affects the eventual crystal morphology. Na^+ , having a smaller size than K^+ , displays strong pair formation with

smaller silicate oligomers (such as monomers). The larger size of K^+ favours the formation of larger silicate oligomers with which $Al(OH)_4^-$ prefers to bind. Therefore, in KOH solutions more geopolymer precursors exist resulting thus in better setting and stronger compressive strength compared to geopolymers synthesised in NaOH solutions. K^+ is seemingly responsible for a higher degree of condensation when compared to Na^+ under the same conditions. Matrices containing K^+ exhibited higher compressive strength and specific surface area, but lower degree of crystallinity and resistance to attack by HCl [39].

The presence of calcium is beneficial in geopolymer network, since it can form amorphously structured Ca-Al-Si gel, which reduces porosity and enhance mechanical properties [37]. Moreover, it was found that both the rate and the extent of metakaolin dissolution were enhanced. Accelerating dissolution increases the Al concentration in solution, thus reducing Si/Al available for geopolymer gel formation and further accelerating the gel formation to cause faster setting [50].

Being a reactant in the first stage and a product in the second stage of geopolymerization, water plays a very important role in the reaction. Since alkali solutions of high concentration can activate the reactive raw material in a quicker and stronger way, the presence of too much water will reduce the geopolymerization rate at first stage because of its dilution effect. At the beginning of condensation stage, too high concentration of water can hinder polycondensation kinetically. However, at the end of polycondensation, residual water can cause an increase of reaction rate. This strange phenomenon may be caused by the continuous dissolution of residual solid particles and hydrolysis of generated Al^{3+} and Si^{4+} [43]. Moreover, once the geopolymer network is formed, the evaporation of residual water contained in the pores can cause shrinkage, due to the contraction of the gel [51].

Alkali also affect pH, which is one of the main parameters to control mechanical properties. pH in the range of 13-14 is found to be the most suitable for the achievement of optimal mechanical properties [45].

Geopolymerization is an exothermal reaction, occurring spontaneously even at room temperature. Curing at higher temperatures, keeping constant the humidity, leads to an increasing rate and extent of reaction, improving mechanical properties. The beneficial

effect of temperature is subjected to a proper control of water evaporation, because of the aforementioned motivations [41], [51].

1.3.3. Geopolymer as alternative to Portland cement

During the last 50 years, geopolymers have proved to be a valid alternative to Portland cement (OPC). Along with interesting engineering properties, equal or even higher than OPC, and the effective passivation of steel rebars, geopolymers have many peculiar properties:

- Fire resistance [52]
- Fast hardening [53]
- Encapsulation of heavy metals and mine tailings [49], [54]–[56]
- Possibility to obtain highly porous inorganic foams [57]
- Synthesis also from wastes, such as fly ashes, blast furnace slag [58]
- Possibility of using organic waste materials as filler [59]
- Low permeability and high resistance to chloride ingress and freeze-thaw [49]
- Acid resistance [42]
- Low CO₂ footprint [60]

Thanks to these properties, geopolymers are finding their applications in niche market sectors, like wastewater treatment, thermal insulation, refractory and nuclear waste storage.

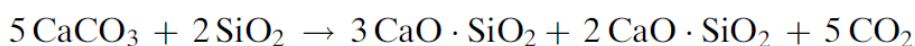
However, relatively little progress has been made towards commercial utilisation in concrete industry. The poor acceptance by the concrete industry is mainly due to the entrenched position of OPC concrete, and it is well known that the industry is quite conservative in adopting new and innovative technologies and products that will replace existing ones [37].

Along with this attitude problem, legislative and technical issues must be solved, which are respectively related to the need for standards in each governmental jurisdiction and to the unanswerable question on durability of geopolymer concrete, given a standard requirement for structural concretes to last for at least several decades. In the developed world, there are very specific standards for what is considered “acceptable” performance for a cementitious binder, which have clearly been developed over many years in collaboration with input from the cement manufacturing companies with the chemistry

and behaviour of OPC-based concretes in mind. Despite this, standards containing constraints, like the minimum cement content, are beginning to be seen as prohibitive, even for cement-based systems. High cement content essentially allows and encourages mix design favouring poor quality aggregates and high water content. Products such as geopolymer concrete, or other non-cementitious and even high-performance cementitious based systems, may not simply be an evolution of existing OPC technology but instead may require an entirely different chemical paradigm to understand their behaviour, and may perform acceptably even without conforming exactly to the established regulatory standards [61].

Provided that a practical mechanism can be put in place to achieve regulatory acceptance of geopolymer concrete in the market, the question still remains over durability. A material that has been subjected to detailed investigation only recently cannot possibly have decades' worth of durability data to prove its long-term stability. Most standard methods of testing cement and concrete durability involve exposing small samples to very extreme conditions – like highly concentrated acid or salt solutions – for short periods of time. These results are then used to predict how the material will perform in normal environmental conditions over a period of decades or more. The major problem with this approach to prove durability is that it can only give indications of the expected performance, rather than definitive proof. Therefore, there has been a process of very slow adoption of new materials, as one may need to wait up to 20–30 years for real-world verification. Adoption of fly ash and slag in concretes is the prime example, where the use of these supplementary materials was resisted for decades [18].

The propellant for the evolution of concrete industry should be the need of a greener technology. Concrete is the most widely used construction material. Current average consumption of concrete is about 1 t/year per every living human being, second only to water consumption. Due to its large consumption, even small reductions of greenhouse gas emissions per ton of manufactured concrete can make a significant global impact. Manufacture of OPC requires the mining of limestone and releasing of carbon dioxide, according to the following reaction [45]:



For each ton of limestone mined, one-third is released as carbon dioxide. Emissions of greenhouse gases through industrial activities have a major impact on global

warming and it is believed that at least 5–7% of CO₂ released to the atmosphere is due to the production of OPC. The demand for worldwide cement production is increasing by approximately 30% per decade as of 2016, and the need for new infrastructure construction in developing nations is projected to force the demand up for cement in the coming years. Manufacture of Portland cement is the fourth largest contributor to worldwide carbon emissions and is only behind petroleum, coal, and natural gas in releasing carbon dioxide that has been locked beneath the earth's surface for millions of years. The new cement factories that are being built mostly in developing nations to meet this forthcoming demand are unsustainable in the long term for three main reasons:

- Cement factories are extremely capital-intensive developments. Once the capital is invested, the investor is committed to cement-production tonnages to recoup their capital investments. Cement manufacturers are notoriously well connected in the construction industry and are resistant to any new low-carbon technologies to protect their investments. Once capital investments are locked into new cement factories, there is little incentive for the cement manufacturers to embrace low-carbon technologies.
- Since cement manufacture is largely automated employments are low with respect to investments: a modern plant usually employs less than 150 people.
- OPC production process is highly energy intensive: each ton of cement produced requires 60–130 kg of fuel oil or its equivalent, depending on the cement variety and the process used, and about 110 kWh of electricity [62].

Geopolymerization has definitely a good potential for the production of “green” concrete and construction materials with lower carbon footprint. In order to accurately assess this potential, the environmental impact of geopolymers has to be quantified by considering also the impact of the by-products (or wastes) used through Life Cycle Assessment (LCA) studies. From the analysis of works present in literature, geopolymer concrete made from fly ash (FA) and granulated blast furnace slag (GBFS) results in lower CO₂ emissions than OPC concrete. The environmental impact of geopolymer concrete is related with the use of sodium silicate solution as activator that results in pollution transfer within all other environmental impact categories. Nowadays, the production of sodium silicate utilizes pure glass cullet, but discarded glass cullet could be

easily used as alternative silicate source. Concerning instead metakaolin-based geopolymer concrete, it has been shown that due to the low Si/Al ratio in metakaolin a high amount of sodium silicate is required, causing thus a higher environmental impact with respect to fly ash and slag-based geopolymers, but still lower than OPC [63]–[65].

Therefore, the best way for the concrete industry to reach its current CO₂ objectives, would be to produce geopolymer concrete from raw material with a suitable Si/Al molar ratio which is recognised as industrial waste and does not have an allocation impact [60].

1.4. The use of waste materials for filler purposes

As previously discussed, geopolymers can be filled with organic and inorganic additives, in some cases even improving in their properties. In this thesis, different wastes, both organic (microalgal biomass and lignin) and inorganic (recycled glass fibres), are used as filler of 3D printed geopolymers.

In the following paragraphs, the applications and the end-of-life management of the materials used as filler in this work are presented.

1.4.1. Microalgae for wastewater treatment

Nowadays, although the strategic importance of fresh water is universally recognized more than ever before, and although issues concerning sustainable water management can be found almost in every scientific, social, or political agenda all over the world, water resources seem to face severe quantitative and qualitative threats. The pollution increase, industrialization and rapid economic development, impose severe risks to availability and quality of water resources in many areas worldwide. Watercourses receive pollution from many different sources, from towns and villages, consisting of discharges from manufacturing or industrial plants, run-off from agricultural land and leachates from solid waste disposal sites. The composition of wastewater is a complex mixture of natural organic and inorganic materials as well as man-made compounds. Three quarters of organic carbon in sewage are present as carbohydrates, fats, proteins, amino acids, and volatile acids. The inorganic constituents include large concentrations of sodium, calcium, potassium, magnesium, chlorine, sulphur, phosphate, bicarbonate, ammonium salts and heavy metals [66].

One of the main consequences of discharge of these saline waters containing lots of nutrients in seas, lakes and rivers is the phenomenon of eutrophication (Figure 1.4.1). Eutrophication occurs when a dense bloom of algae grows in water due to presence of high concentrations of nitrogen and phosphorus, the main nutrients of concern. This reduces the level of oxygen in the aquatic system to less than the natural level that is required by other aquatic organisms causing their death [67].

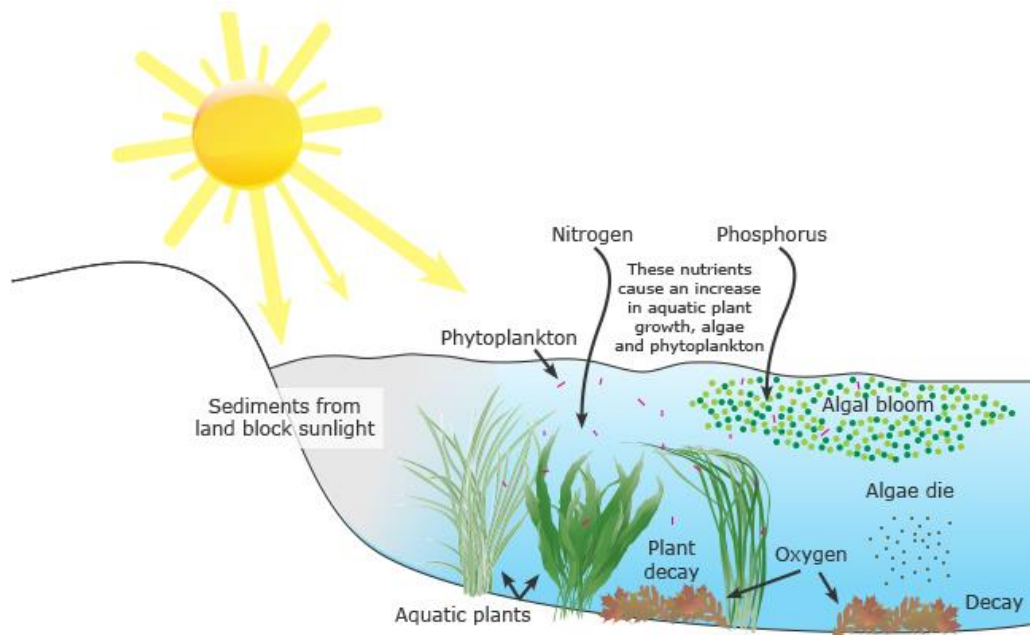


Figure 1.4.1. Scheme of eutrophication process [68]

The ability of microalgae to grow quickly in water that is rich in nutrients can be positively used in wastewater treatment to remove the nutrients from wastewater before discharge to the river. Thus, microalgae have the potential for alternative wastewater treatment systems with almost zero concentration of final nutrients [69].

The aim of wastewater treatment is to convert the waste materials present in wastewaters into stable oxidised end products which can be safely discharged to inland or coastal waters without any adverse ecological effects. A wastewater treatment plant is a combination of separate treatment processes or units designed to produce an effluent of specified quality from a wastewater influent of known composition and flow rate. Unit treatment processes can be classified into five stages [70]:

- Preliminary treatment consists in the removal and disintegration of gross solids and grits, and in the separation of storm water. Oil and grease are also removed at this stage if present in large amounts;
- Primary (sedimentation) treatment usually involves the removal of settleable solids which are separated as sludge;
- Secondary (biological) treatment consists in the oxidation of the dissolved and colloidal organics by the action of micro-organisms;
- Tertiary treatment is a further treatment of a biologically treated effluent to eliminate the organic content (expressed by the parameter BOD₅), bacteria, suspended solids, specific toxic compounds or nutrients to enable the final effluent to comply with standards;
- Sludge treatment, finally, consists in the dewatering, stabilisation and disposal of sludge.

Microalgae growth in waste waters is inserted in the secondary and tertiary treatment. There are mainly two approaches to grow microalgae: suspended cultures and immobilized cultures.

In suspended cultures, algae are grown in a continuously agitated water to keep them in suspension. Open and closed photobioreactor systems can be adopted. The most commonly used open system is the so-called raceway pond (Figure 1.4.2a), which is made of a closed loop recirculation channel, no more than 0.3 m deep in order to provide enough sunlight to allow photosynthesis by microalgae. Raceways are relatively inexpensive to build and operate, but often suffer low productivity. A less expensive, but more productive alternative is given by closed suspension systems. Several configurations of closed photobioreactor can be found: in tubular arrays (Figure 1.4.2b) water containing biomass is moved by pressure, while in air-lift panels (Figure 1.4.2c) water movement is promoted by bubbling. Also for these systems, the dimension of the channels containing algae is selected to promote sunlight arrival and photosynthesis [71]–[73].

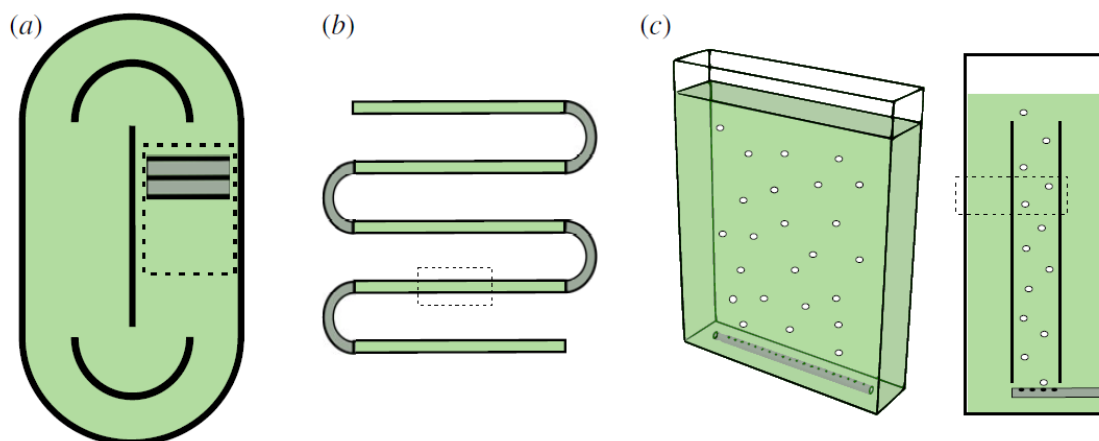


Figure 1.4.2. Configurations for suspension cultures: (a) open pond in raceway configuration; (b) tubular closed photobioreactor; (c) air-lift flat panel [71]

Immobilized cultures, also known as attached cultures, are based on microalgae growing in the form of biofilm on the surface of substrates. Attached microalgae cultivation could overcome the issues of high energy, high cost and difficult harvesting of traditional suspended systems because it shows higher microalgae biomass productivity, requires less space and water consumption, and it can be easily scaled-up at industrial level. However, with this technique the culture control is low. This is why, up to now, the most used cultivation techniques remain the suspended ones [74].

Institutions are increasing their attention through the problem of wastewater treatment and to economic viable alternatives to tackle it. European Union, along with legislation activity, promoted the project SaltGae in the framework of Horizon 2020 research and innovation programme. The aim of the project is to implement and demonstrate at large scale the long-term technological and economic feasibility of an innovative, sustainable and efficient solution for the treatment of high salinity wastewater based on the use of microalgae. In addition to an effective and ecological solution for wastewater treatment, SaltGae includes in its workplan the valorisation of end-of-life algal biomass into different by-products for high value-added applications, including extraction of compounds, animal feed, synthesis of platform chemicals, preparation of edible coatings and fillers for bioplastics and ceramics. This view of end-of-life management of microalgae is supposed to furtherly reduce the economic and environmental impact of the treatment [75].

1.4.2. Lignin from wood pulping processes

Lignin is a major constituent in structural cell walls of all higher vascular land plants. Its polyphenolic structure is well known for its role in woody biomass to give resistance to biological and chemical degradation, thanks to its hydrophobic nature and insolubility in aqueous systems that prevents the access of degrading chemicals and organisms. The monomeric units of phenylpropane in lignin polymers are linked in a complex network through different types of ether and ester bonds as well as carbon-carbon bonds (Figure 1.4.3). The lignin occurring in plant cell walls is commonly closely associated with polysaccharide structures of cellulose and hemicellulose [76].

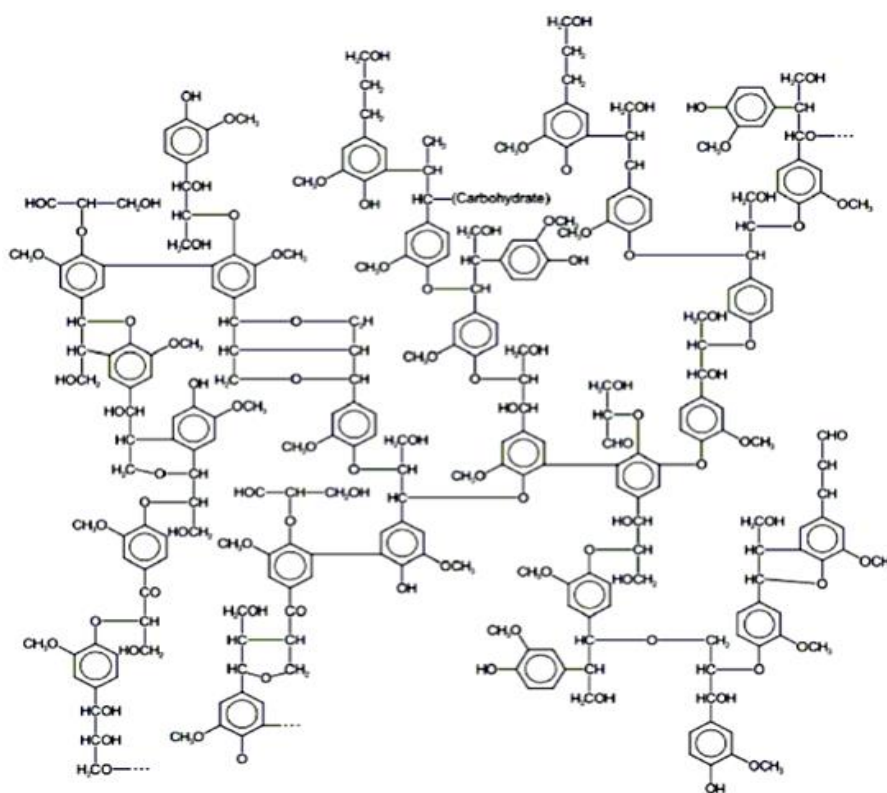


Figure 1.4.3. Structure of lignin [77]

Wood and other lignocellulosic resources are used to extract the cellulose fibres for paper or composite applications or for the production of dissolving cellulose. In these processes, lignin is a waste, which must be dissolved and separated from the other constituents of wood. There are two main dissolution processes of lignin:

- Sulfite pulping: the lignin is made water soluble through the introduction of hydrophilic sulfonate groups followed by hydrolytic cleavage of ether groups;

- Kraft (and soda) pulping: the lignin structure is modified and depolymerized through the action of strong aqueous alkali with simultaneous presence of hydrosulfide ions [78].

Today, around 95% of the worldwide production of lignin is mainly applied as fuel for biorefinery plants, while just the 5% is commercialized for the production of adhesives, dispersants for dyes, surfactants, pesticides, fertilizers, additives for concrete [79].

Rapidly increasing concentration of carbon dioxide in the atmosphere resulting in successive global warming has created a growing awareness that the future society must rely much more on renewable resources both for energy production and in material systems. In this development, biomass will play important roles. Consequently, several initiatives have been taken to develop new and simplified separation processes for biomass polymers and many laboratories are also working on the development of new products and material combinations in which lignin is involved, as an alternative to burning [80].

1.4.3. Recycled glass fibres

As the thermoset and thermoplastic composite technology evolves, more and more materials are being replaced by glass fibre composites, which can provide high performing products in several applications. The need to find a way to recycle these composites is a real concern, urged by the gradually stricter environmental legislation.

Several recycling techniques for glass fibre components exist:

- Mechanical recycling: this recycling approach (also called “grinding”) consists in the shredding of the composite into powder of finer or coarser dimension. The process starts with low-speed cutting or crushing of the material to a size of 50-100 mm, which is further reduced to 10 mm – 50 μm . The hammer mill process is a common method that reduces the size of the material through impact and shear action until it can pass through a defined size of milling screening holes [81].
- Thermal processes: the general principle of thermal processes is that the composite is heated in a furnace with operative temperatures between 450°C and 700°C based on the resin type. Polyester resins require a lower

temperature than epoxy and thermoplastic ones. The resin is volatilised into lower-weight molecules while releasing mainly gases, such as hydrogen, methane and carbon dioxide. Oil fraction can be used for combustion, but it leaves char on the fibres, thus requiring additional purification steps that might further lower the properties of the material [82], [83].

- Solvolysis: this technique is based on nucleophilic substitution or elimination, where the nucleophile is a solvent molecule. During the process, a reactive solvent, alone or mixed with reactive or not co-solvent, diffuses inside the material and cleaves specific bonds, such ester bonds in polyesters. This implies that it is possible to recover monomers from the polymeric matrix while leaving the fibres clean from residual material [84]. To degrade the polymeric matrix, solvolysis needs temperatures lower than pyrolysis, hence it is advantageous. However, to reach supercritical conditions of the liquids, the reactor has to sustain severe temperature and pressure conditions, as well as the corrosion caused by the modified properties of the solvent. As a consequence, the machinery has high maintenance costs and few industries adopted this technique [85].

European Union is promoting glass fibre recycling, in compliance with the waste treatment legislation. In the framework of the already mentioned Horizon 2020 programme, the project FiberEUse aims at integrating different innovation actions through a holistic approach to enhance profitability of composite recycling and reuse in value-added products. Through new cloud-based ICT solutions for value-chain integration, scouting of new markets, analysis of legislation barriers, life cycle assessment for different reverse logistic options, FiberEUse wants to support industry in the transition to a circular economy model for composites [86].

2. Materials and methods

2.1. Materials

The geopolymer formulations present in this study are based on the following components:

- Metakaolin
- Alkaline activator
- Bentonite
- Filler (biomass or fibre)

All formulations contain metakaolin and the activator in a fixed ratio of 5/4. The presence and the amount of other components may vary (formulations are reported in § 2.2).

2.1.1. Metakaolin

The raw material (Mefisto L05) is provided by České lupkové závody a.s.. The composition guaranteed by the supplier is reported in Table 2.1.1.

Table 2.1.1. Guaranteed composition of metakaolin Mefisto L05

Al₂O₃ (wt%)	SiO₂ (wt%)	K₂O (wt%)	Fe₂O₃ (wt%)	TiO₂ (wt%)	MgO (wt%)	CaO (wt%)
41.1	54.1	0.8	1.1	1.8	0.18	0.13

The specific surface of the powder is 12.69 m²/g and the average particle size d₅₀ is 3 μm. Figure 2.1.1 shows the particle size distribution curves.

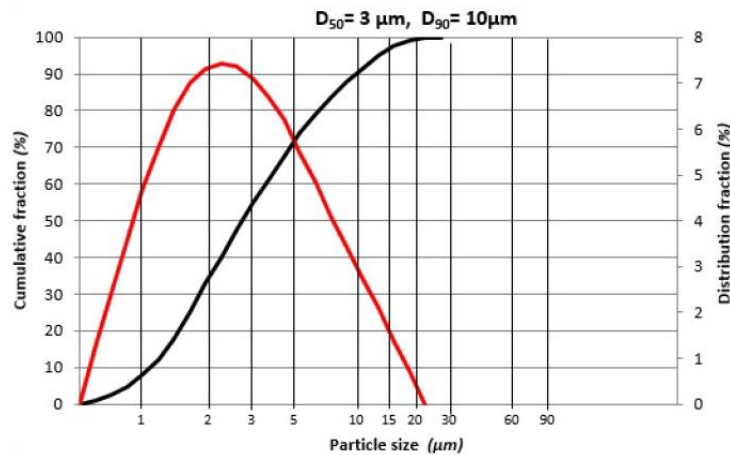


Figure 2.1.1. Particle size distribution (cumulative fraction in black, distribution fraction in red) of metakaolin Mefisto L05, provided by the supplier

2.1.2. Alkaline activator

A commercial alkaline activator based on Na_2SiO_3 and NaOH , provided by České lupkové závody a.s., is used. From thermogravimetric analysis (TGA) performed on the activator, the residual solid part is 38% by weight of the total solution (refer to § 2.5.1 for the experimental procedure and to Appendix for the results). pH, measured by litmus paper, is 12.

2.1.3. Bentonite

Bentonite is an absorbent aluminium phyllosilicate clay consisting mostly of montmorillonite. It is used in geopolymer pastes as a rheology modifier, to increase plasticity and to obtain a proper viscosity.

Three different kinds of sodium bentonite are used:

- Bentonite, provided by Sigma Aldrich Inc., named B1 in the nomenclature of this work;
- Nanoclay, provided by Sigma Aldrich Inc., named B2;
- Mapeproof Seal, provided by Mapei S.p.A., named B3.

2.1.4. Biomass

Since the framework of the thesis is SaltGae project, one of the main focus is on the valorisation of microalgal biomass used for wastewater treatment. Two different species of microalgae, provided by Archimede Ricerche S.r.l., are added to geopolymer pastes:

- Spirulina Platensis, named SP in the nomenclature of this work;
- Tetraselmis Suecica, named TT.

Table 2.1.2 reports the results of the compositional analysis on microalgae performed by Extractis. The pH of microalgae in water ranges from 7 to 8.

Table 2.1.2. Composition of *Spirulina Platensis* and *Tetraselmis Suecica* after centrifugation

	Spirulina Platensis	Tetraselmis Suecica
Dry Matter (DM) (%)	97.49	95.16
Ash (%/DM)	9.12	17.05
Proteins (%/DM)	67.78	37.89
Total sugars (%/DM)	9.31	14.49
Total free sugars (%/DM)	2.79	4.19
Lipids (%/DM)	6.26	12.82
Other (%/DM)	4.74	13.56

Proteins and other nutrients can be extracted from microalgal biomass. The possibility to use low-protein residues of biomass after the extraction as filler is very interesting, since these materials, which are effectively wastes, have an even lower value than pristine microalgae. Residues of *Spirulina* (named RS in this work) and of *Tetraselmis* (named RT in this work) were obtained by Extractis, from microalgae provided by Archimede Ricerche. Only data about ash % and protein % are available and reported in Table 2.1.3.

Table 2.1.3. Composition of residues of *Spirulina* and *Tetraselmis*

	Residue of Spirulina	Residue of Tetraselmis
Dry Matter (DM) (%)	> 99.5	> 99.5
Ash (%/DM)	22.6	16.9
Proteins (%/DM)	35.7	20.6

The effect of microalgae on the mechanical behaviour of geopolymers has been compared to that of lignin (named LI in this work). Lignin used in this work has been extracted from wood through Kraft process, which is based on the action of sodium hydroxide and sodium sulphide.

2.1.5. Recycled fibres

Glass fibres are commonly used as reinforcing materials for geopolymer concrete [87]. Feasibility tests on the use of recycled glass fibres as additives for geopolymers have been performed in the framework of the European project FiberEUUse. Recycled glass fibres, provided by Rivierasca S.p.A., are obtained by mechanical crushing of end-of-life glass fibre structures (e.g. windmill blades, canoe, etc.). As a consequence of this process, the fibres are surrounded by residual polymer binder; the average glass content of these recycled materials was estimated in previous works by TGA (refer to § 2.5.1 for the experimental procedure and Appendix for the results). Two types of recycled glass fibres are used:

- white recycled (named WR in the nomenclature of this work); glass content = $11.9 \pm 0.1\%$, average dimension = $3 \mu\text{m}$;
- red recycled (named RR), containing iron oxides impurities; glass content = $32.0 \pm 2.0\%$, average dimension = $4 \mu\text{m}$.

Virgin chopped glass fibres (Fill 100, series FM04, named VF in this work), provided by Italdry S.r.l., having diameter of $15 \mu\text{m}$ and a fibre-length of $200 \mu\text{m}$, are used as a benchmark.

2.2. Formulations

Several geopolymer formulations have been prepared and tested. They are divided in formulations for 3d-printing, containing bentonite, and formulations for casting, without bentonite. Notice that some casted samples are prepared with recipes for 3D printing, but not vice versa (§ 3.2, 3.3 and 3.4). If not explicitly specified, the bentonite used is B1.

2.2.1. Formulations for 3D printing

Two approaches are followed to prepare pastes suitable for LDM 3D printing:

- adding to the slurry made of metakaolin and activator a high amount of bentonite and then distilled water to adjust viscosity (high-bentonite formulation, HB in the nomenclature of this work);
- adding to the same slurry a lower amount of bentonite, without the further addition of water (low-bentonite formulation, LB in the nomenclature of this work).

The addition of biomass and fibre is computed by weight over the sum of the powders and is indicated per hundred parts (php) with respect to metakaolin and bentonite. In Table 2.2.1 and Table 2.2.2 the compositions are reported both in weight percentage, with respect to the total mass of the paste, and in grams, considering the typical weighing to fill a 20 mL syringe.

Each formulation is named with an acronym, generally XB-GYZN. XB stands for the approach the formulation is based on, i.e. HB (high-bentonite) or LB (low-bentonite). GYZ indicates the additive present, e.g. GSP is used for samples containing *Spirulina*. N is a number, which indicates the amount of additive per hundred parts. If no additive is present, the sample is called XB-GEO.

Water to solid ratio is computed taking into account that the concentration of sodium silicate in the activator is 38% by weight.

Table 2.2.1. Formulations of pastes for LDM 3D printing, containing biomass

Sample	Additive php (powder)	Metakaolin		Bentonite		Activator		Water		Additive		W/S
		wt%	g	wt%	g	wt%	g	wt%	g	wt%	g	
HB-GEO	0	37.6	18.8	22.6	11.3	30.0	15.0	9.8	4.9	0.0	0.0	0.40
HB-GSP1	1	37.0	18.8	22.2	11.3	29.5	15.0	10.6	5.4	0.6	0.3	0.41
HB-GSP3	3	36.2	18.8	21.8	11.3	28.9	15.0	11.4	5.9	1.7	0.9	0.42
HB-GSP5	5	35.5	18.8	21.3	11.3	28.3	15.0	12.1	6.4	2.8	1.5	0.42
HB-GTT1	1	37.0	18.8	22.2	11.3	29.5	15.0	10.6	5.4	0.6	0.3	0.41
HB-GTT3	3	36.2	18.8	21.8	11.3	28.9	15.0	11.4	5.9	1.7	0.9	0.42
HB-GTT5	5	35.5	18.8	21.3	11.3	28.3	15.0	12.1	6.4	2.8	1.5	0.42
HB-GRS1	1	37.0	18.8	22.2	11.3	29.5	15.0	10.6	5.4	0.6	0.3	0.41
HB-GRS3	3	36.2	18.8	21.8	11.3	28.9	15.0	11.4	5.9	1.7	0.9	0.42
HB-GRS5	5	35.5	18.8	21.3	11.3	28.3	15.0	12.1	6.4	2.8	1.5	0.42
HB-GRT1	1	37.0	18.8	22.2	11.3	29.5	15.0	10.6	5.4	0.6	0.3	0.41
HB-GRT3	3	36.2	18.8	21.8	11.3	28.9	15.0	11.4	5.9	1.7	0.9	0.42
HB-GRT5	5	35.5	18.8	21.3	11.3	28.3	15.0	12.1	6.4	2.8	1.5	0.42
HB-GLI1	1	37.0	18.8	22.2	11.3	29.5	15.0	10.6	5.4	0.6	0.3	0.41
HB-GLI3	3	36.2	18.8	21.8	11.3	28.9	15.0	11.4	5.9	1.7	0.9	0.42
HB-GLI5	5	35.5	18.8	21.3	11.3	28.3	15.0	12.1	6.4	2.8	1.5	0.42
LB-GEO	0	47.3	23.6	15.0	7.5	37.7	18.8	0.0	0.0	0.0	0.0	0.31
LB-GSP1	1	46.8	23.6	14.9	7.5	37.3	18.8	0.4	0.2	0.6	0.3	0.31
LB-GSP3	3	46.1	23.6	14.6	7.5	36.7	18.8	0.8	0.4	1.8	0.9	0.31
LB-GSP5	5	45.4	23.6	14.4	7.5	36.1	18.8	1.2	0.6	2.9	1.5	0.31
LB-GSP10	10	43.6	23.6	13.9	7.5	34.8	18.8	2.2	1.2	5.5	3.0	0.31
LB-GTT1	1	46.8	23.6	14.9	7.5	37.3	18.8	0.4	0.2	0.6	0.3	0.31
LB-GTT3	3	46.1	23.6	14.6	7.5	36.7	18.8	0.8	0.4	1.8	0.9	0.31
LB-GTT5	5	46.8	23.6	14.9	7.5	37.3	18.8	0.4	0.2	0.6	0.3	0.31

Table 2.2.2. Formulations of pastes for LDM 3D printing, containing fibres

Sample	Additive php (powder)	Metakaolin		Bentonite		Activator		Water		Additive		W/S
		wt%	g	wt%	g	wt%	g	wt%	g	wt%	g	
LB-GEO	0	47.3	23.6	15.0	7.5	37.7	18.8	0.0	0.0	0.0	0.0	0.31
LB-GRR5	5	45.4	23.6	14.4	7.5	36.2	18.8	1.2	0.6	2.9	1.5	0.31
LB-GRR10	10	45.6	18.8	12.1	5.0	36.4	15.0	0.0	0.0	5.9	2.5	0.29
LB-GRR20	20	42.1	18.8	11.2	5.0	33.6	15.0	2.2	1.0	11.0	4.9	0.30
LB-GRR30	30	39.0	18.8	10.4	5.0	31.2	15.0	4.2	2.0	15.3	7.4	0.31
LB-GWR5	5	45.4	23.6	14.4	7.5	36.2	18.8	1.2	0.6	2.9	1.5	0.31
LB-GWR10	10	45.6	18.8	12.1	5.0	36.4	15.0	0.0	0.0	5.9	2.5	0.29

2.2.2. Formulations for casting

Formulations prepared exclusively for casting are reported Table 2.2.3. A “C” in the nomenclature denotes that the formulations are for casting, then the same nomenclature rules explained in § 2.2.1 are applied. The amount of additive is calculated over the powders, so just over metakaolin in this case. Mass values showed in the table refer to the typical weighing to fill a set of eight cubic samples. Supplementary water is added only to the sample containing high concentration of biomass (C-GSP30).

Table 2.2.3. Formulations of pastes for casting

Sample	Additive php (powder)	Metakaolin		Activator		Water		Additive		W/S
		wt%	g	wt%	g	wt%	g	wt%	g	
C-GEO	0	55.6	18.8	44.4	15.0	0.0	0.0	0.0	0.0	0.38
C-GSP30	30	45.3	18.8	36.1	15.0	5.1	2.1	13.5	5.6	0.38
C-GRR13	13	51.9	18.8	41.4	15.0	0.0	0.0	6.8	2.5	0.35
C-GRR19	19	50.3	18.8	40.1	15.0	0.0	0.0	9.6	3.6	0.33
C-GRR26	26	48.6	18.8	38.8	15.0	0.0	0.0	12.7	4.9	0.32
C-GRR39	39	45.7	18.8	36.5	15.0	0.0	0.0	17.9	7.4	0.29
C-GRR57	57	42.2	18.8	33.7	15.0	0.0	0.0	24.1	10.7	0.27
C-GWR13	13	51.9	18.8	41.4	15.0	0.0	0.0	6.8	2.5	0.35
C-GVF13	13	51.9	18.8	41.4	15.0	0.0	0.0	6.8	2.5	0.35
C-GVF26	26	48.6	18.8	38.8	15.0	0.0	0.0	12.7	4.9	0.32
C-GVF39	39	45.7	18.8	36.5	15.0	0.0	0.0	17.9	7.4	0.29

2.2.3. Formulations to study the effect of bentonite

Bentonite amount is of paramount importance both for rheological properties of the fresh pastes and for mechanical properties of the hardened specimens. To understand the effect of bentonite, five formulations at different percentages have been prepared and characterised. These formulations are named “B-x”, where x is the weight percentage of bentonite. Notice that B-0 corresponds to the slurry made just by metakaolin and activator (also called C-GEO) and B-15 is equivalent to the unfilled low bentonite formulation (LB-GEO).

Table 2.2.4. Formulations prepared to study the effect of bentonite

Sample	Metakaolin		Activator		Bentonite		W/S
	wt%	g	wt%	g	wt%	g	
B-0 (C-GEO)	55.7	23.6	44.3	18.8	0.0	0.0	0.38
B-7.5	51.3	25.7	41.2	20.6	7.5	3.8	0.34
B-15 (LB-GEO)	47.3	23.6	37.7	18.8	15.0	7.5	0.31
B-22.5	43.0	21.5	34.4	17.2	22.5	11.3	0.27
B-30	38.8	19.4	31.2	15.6	30.0	15.0	0.24

2.3. 3D printing setup

2.3.1. 3DRag

3DRag (Figure 2.3.1) is a low-cost 3D printer produced by Futura Elettronica S.r.l., compatible with all the RepRap software and firmware available for free. The structure, made by aluminium profiles, is designed to ease the interlocking between all the parts and to give lightness and rigidity, suppressing unwanted vibrations. The movement on the plane (X/Y axes) is controlled by the platen, while the progression in height (Z axis) is related to the cart. In this configuration, the extruder, which is fixed on the cart, moves only in Z-direction. The printing volume is 20 cm x 20 cm x 20 cm.

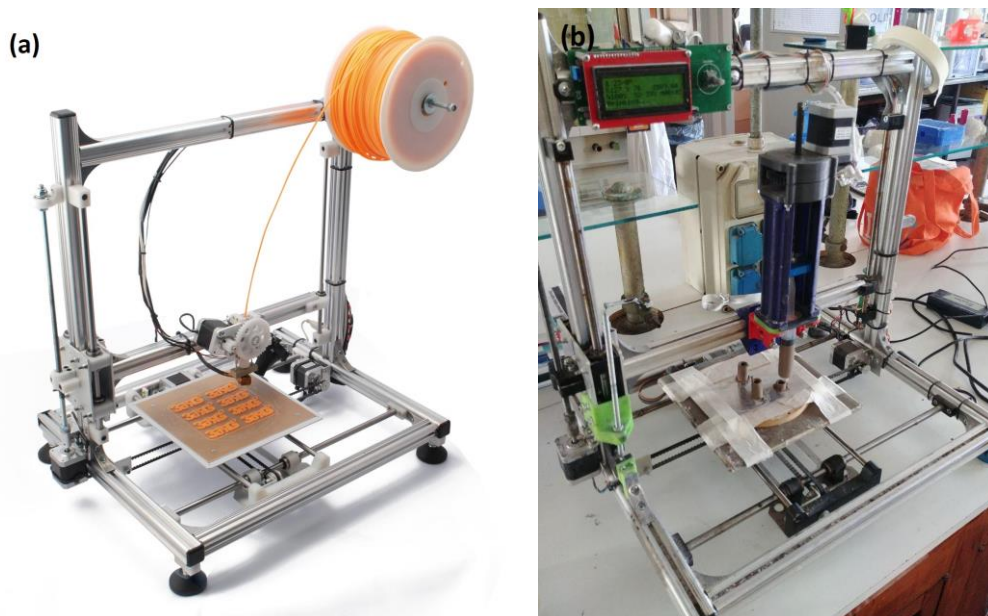


Figure 2.3.1. 3DRag in (a) FDM and (b) LDM configuration

3DRag is originally designed as a traditional FDM printer, processing plastic filaments. The extruder part has been modified by Dr. Gabriele Natale to print liquid materials through a syringe (LDM technology) [88]. In the standard FDM configuration three stepper motors NEMA 17 are necessary to move all the mechanical parts; in the modified configuration, another stepper motor is added, and the heated extruder is replaced by a syringe. The additional motor, thanks to plastic gears and mechanical interconnections (Figure 2.3.2), pushes down the piston inside the syringe and the material can be extruded.

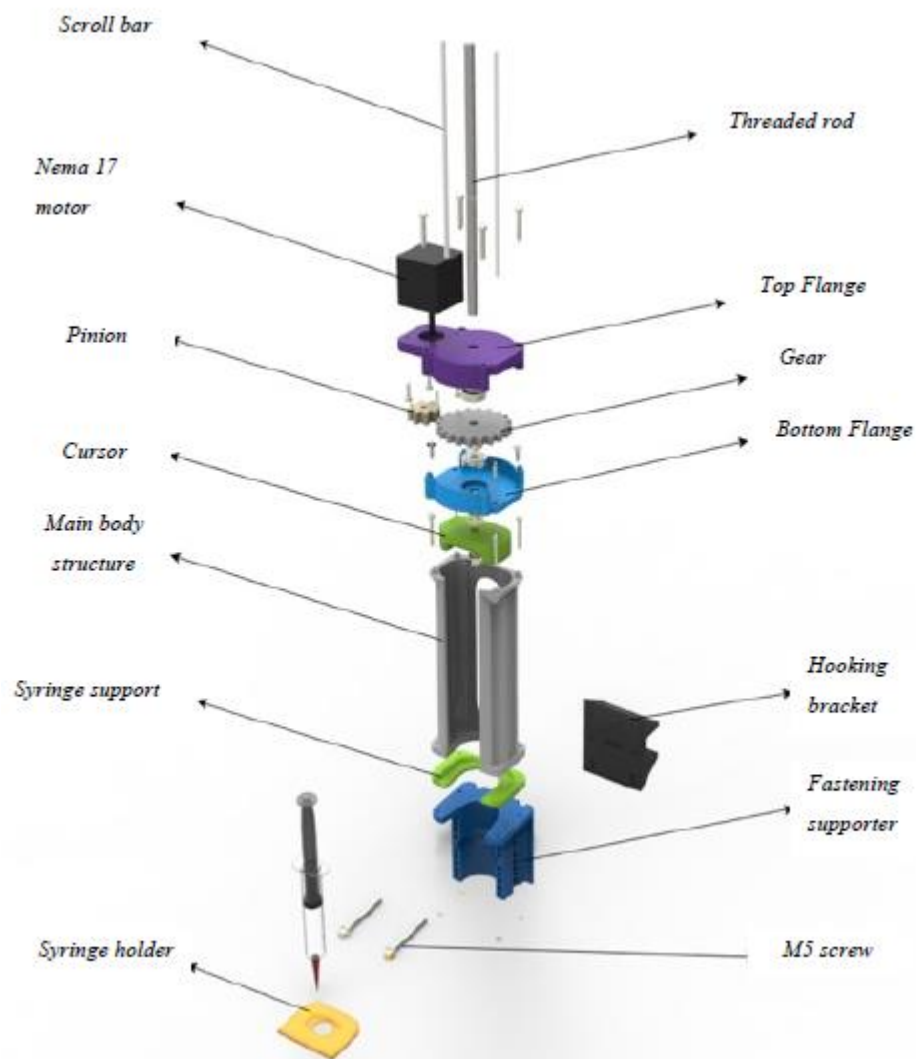


Figure 2.3.2. Schematic representation of LDM syringe extruder, designed by Dr. Gabriele Natale [88]

This setup is used in this work to produce samples for mechanical tests. The majority of printed samples are made in spiral mode, which is a printing technique that converts the subsequent layers in a continuous spiral. In this way, hollow structures can be obtained from bulky CAD models, since only the outer perimeter is printed. The printing parameters, kept constant for all the printings performed, are listed in Table 2.3.1. Since in LDM configuration no filament is present, the diameter of the syringe is taken as filament diameter.

Table 2.3.1. Printing parameters used with 3DRag LDM printer

Layer height	Shell thickness	Print speed	Filament diameter	Flow	Nozzle size	Travel speed	Infill
0.6 mm	2.25 mm	20 mm/s	18.6 mm	130 %	2.25 mm	140 mm/s	0 % (spiral mode)

2.3.2. Scale-up setup

To print bigger parts, a Delta WASP 40100 Clay (Figure 2.3.3), produced by WASP S.r.l., and rent by the makerspace Superforma (Milano) is employed. This printer has a printing volume of 40 cm x 40 cm x 100 cm.



Figure 2.3.3. Delta WASP 40100 Clay

Differently from 3DRag, whose movements are based on three Cartesian axes, Delta machines move according to polar coordinates. The extrusion system is different, as well: the material is charged in a close container (with capacity ranging from 3L to

10L), which is kept under pressure; pressure makes material flow to an extruder provided with an endless screw, which transports the fluid to the nozzle.

Three objects, characterized by different features, have been selected for large scale printing:

- a pipe with a bulge (Figure 2.3.4a), designed to be inserted in a chemical reactor, is selected as a technical part that can be manufactured by LDM technology. The pipe is designed as a self-standing hollow structure with a thick perimeter (1.6 cm). To obtain a hollow object from a bulky CAD model, the amount of infill is set to 0 to print only the perimeters. Using an 8 mm-nozzle, perimeters are printed with a double shell structure (Figure 2.3.4b); no high level of detail is required;

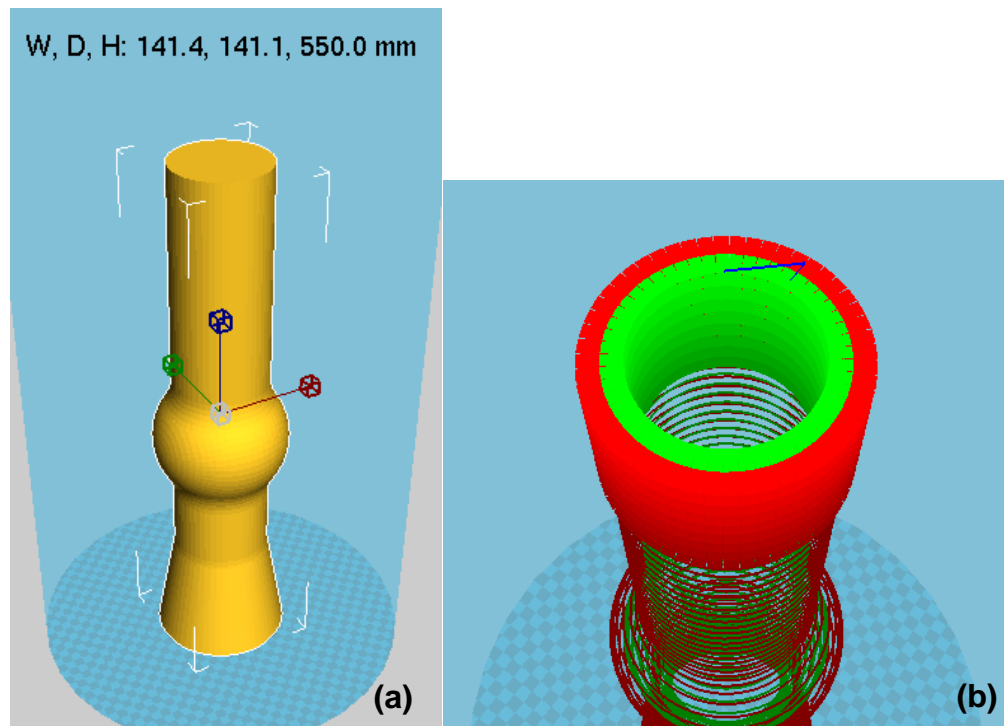


Figure 2.3.4. (a) STL model and (b) rendering of the machine toolpath of the pipe for scale-up printing

- a model of Pirelli skyscraper (also known as “Pirellone”) is selected as a reproduction of an iconic building (Figure 2.3.5 a and b). In this case, a higher level of detail is required, so a smaller nozzle is used (4 mm). 25% of infill is selected to sustain the roof of the structure, without increasing too much its weight (Figure 2.3.5 c). As for the pipe, the outer perimeter is printed with two shells;

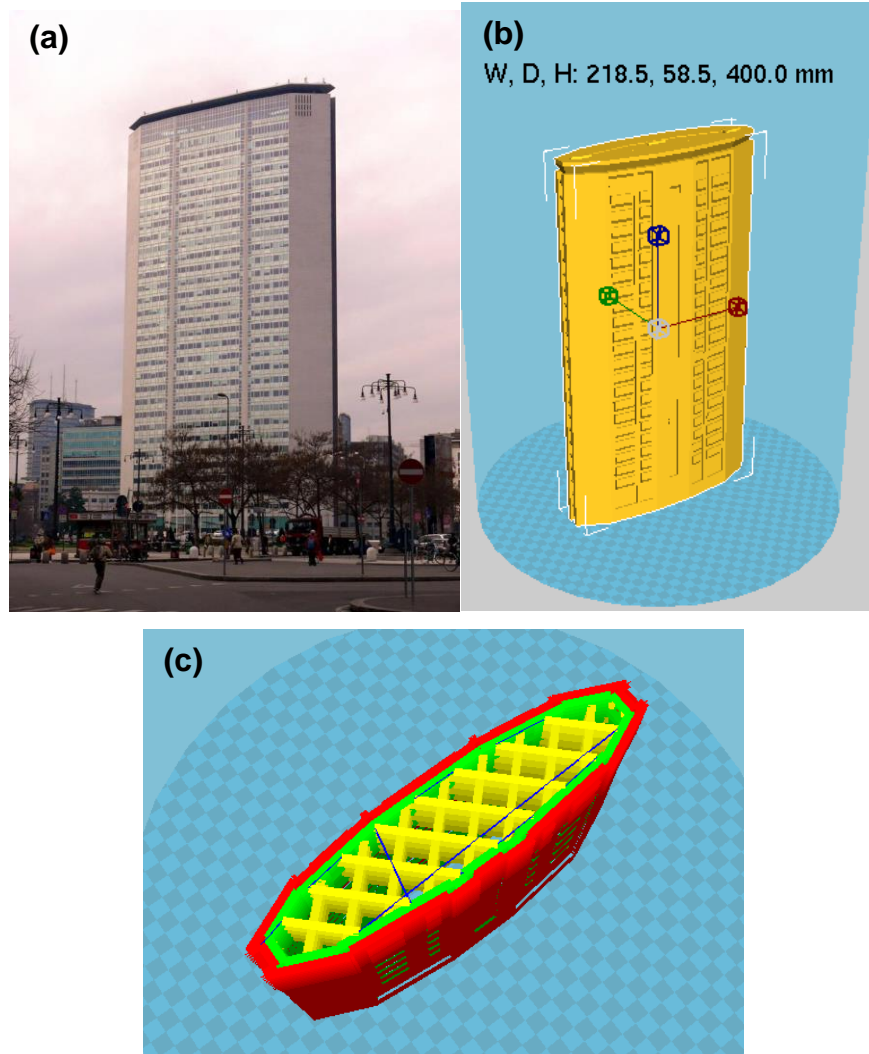


Figure 2.3.5. (a) Pirelli skyscraper; (b) STL model; (c) rendering of machine toolpath, evidencing the infill

- a hollow structure with a complex twisted geometry (Figure 2.3.6 a) is selected as an example of a shape very difficult to obtain by traditional manufacturing technologies. The hollow structure is obtained by printing the perimeters in spiral mode (Figure 2.3.6 b). A 4 mm-nozzle is adopted, and the perimeter is printed with a single thin wall.

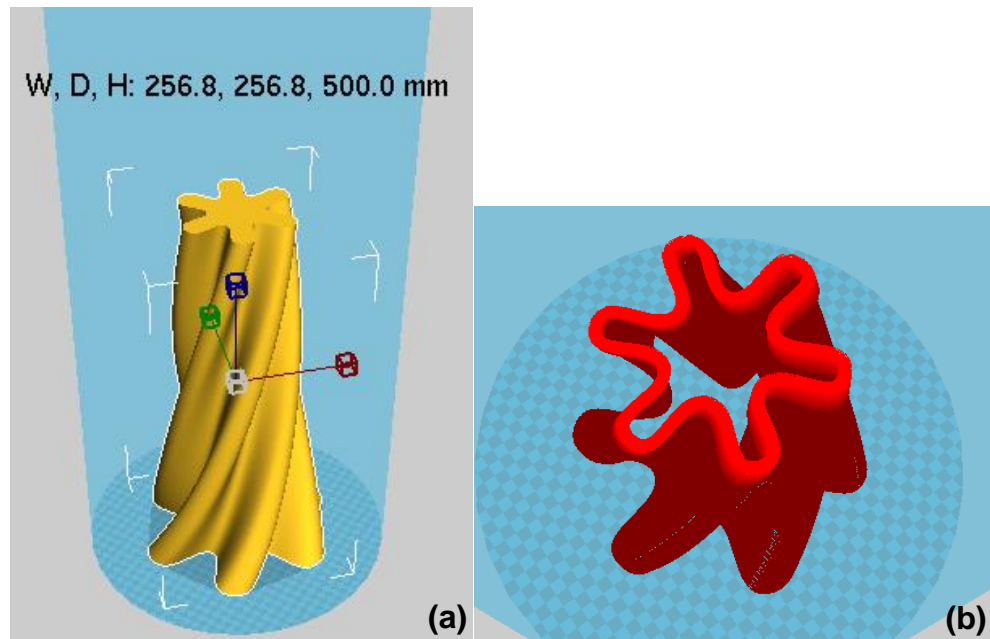


Figure 2.3.6. (a) STL model and (b) rendering of machine toolpath, evidencing the spiral mode, of the hollow twisted structure selected for scaled-up printing

Printing parameters, which are summarized in Table 2.3.2, have been adapted for each model. Flow was adjusted during printing, remaining in a certain range, to cope with flow instabilities.

Table 2.3.2. Printing parameters used with Delta WASP 40100 Clay

Object	Nozzle size	Layer height	Shell thickness	Print speed	Filament diameter	Flow	Travel speed	Infill
Pipe	8 mm	4 mm	16 mm (double-shell)	50 mm/s	1.8 mm	100-120%	120 mm/s	0 %
Pirellone	4 mm	2 mm	8 mm (double-shell)	85 mm/s	1.8 mm	85-100%	120 mm/s	25%
Twisted structure	4 mm	2 mm	4 mm (single-shell)	85 mm/s	1.8 mm	50-75%	120 mm/s	0% (spiral mode)

2.4. Preparation of the samples

2.4.1. Preparation of the pastes

The procedure adopted to prepare the pastes consists in the following steps:

- powders are weighed in a plastic beaker;
- liquids are then added and weighed in the same beaker;
- the components are manually mixed with a spatula for around five minutes, until a fluid homogeneous paste is obtained.

2.4.2. Casting

Casted samples are prepared to test non-printable formulations and to have a comparison with 3D printed specimens, regarding both geometry and process. Cylinders (diameter 14 mm, height 28 mm) and cubes (side 14 mm) are casted in PDMS moulds (Figure 2.4.1).



Figure 2.4.1. PDMS moulds used for casting

To obtain homogeneous casts, pastes with low viscosity are manually vibrated for 2 minutes, while more viscous ones are mechanically compacted in the moulds with a

piston. After two days, the specimens are removed from the moulds and kept at ambient temperature under a plastic film for 7 or 28 days. At the end of the ambient curing period, some specimens are annealed at 800 °C for 4 hours in a muffle oven (model 10-D1418/A, produced by Controls S.p.A.).

Casting is used also to prepare cylindrical specimens to be tested when still fresh. PLA 3D printed (by FDM) moulds, which are designed to be easily opened without damaging the fresh material, are used (Figure 2.4.2). The dimensions of these specimens are the same as the other casted samples.

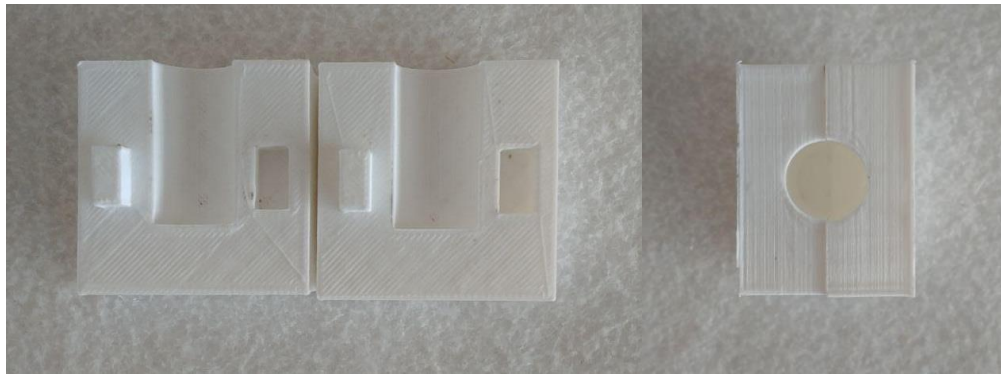


Figure 2.4.2. PLA 3D printed mould used for fresh samples

2.4.3. 3D printing

3D printing with 3DRag adapted to LDM is used to prepare specimens for mechanical compression tests. Since one of the main advantages of additive manufacturing is the possibility to easily obtain empty lightweight structures, most of the printed specimens are hollow cylinders (diameter 15 mm, height 28 mm). A full cylinder has been modelled on SolidWorks (developed by Dassault Systèmes) and the STL file has been exported to the slicing software Cura (by Ultimaker) to create the G-Code. By adopting spiral mode, only the perimeters of the model are printed, and the hollow structure is obtained. For each batch, six specimens are printed on an metallic support; then they are kept at ambient temperature under a plastic film for 7 or 28 days. At the end of the ambient curing period, some specimens are annealed at 800 °C for 4 hours in a muffle oven (model 10-D1418/A, produced by Controls S.p.A.).

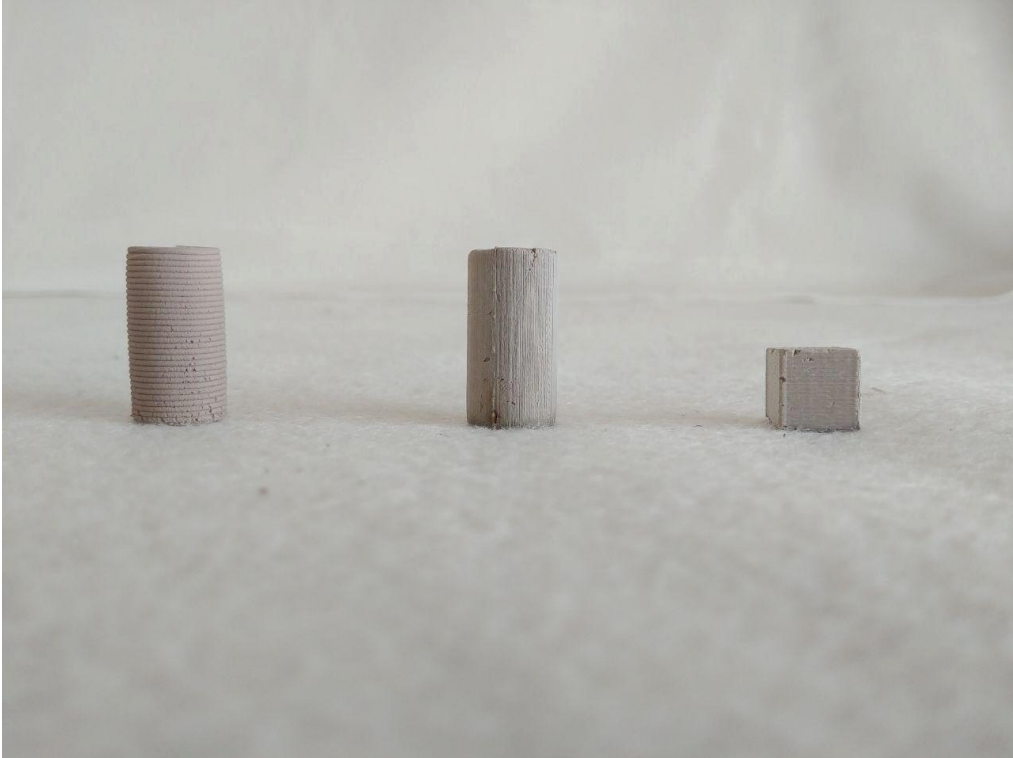


Figure 2.4.3. Hardened samples. From left to right: 3D printed hollow cylinder, casted cylinder, casted cube

To complete the comparison between casting and 3D printing, some filled specimens have been printed with the same shape and dimension of casted ones (Figure 2.4.4).

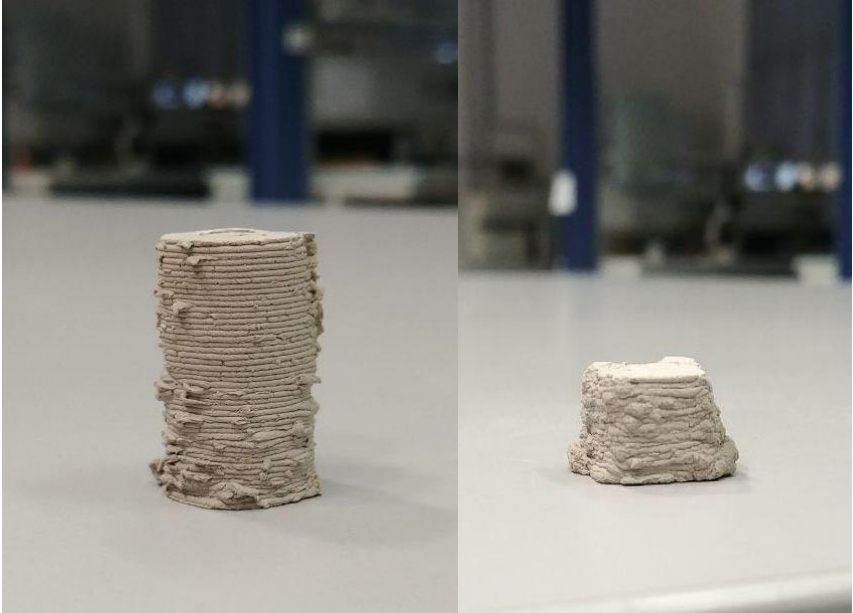


Figure 2.4.4. 3D printed full specimens

2.5. Characterization techniques

2.5.1. Characterization techniques adopted in preliminary studies

2.5.1.1. Thermogravimetric analysis (TGA)

Thermogravimetric analysis (TGA) was performed on microalgal samples to characterize the different decomposition steps, on alkaline activator to evaluate the amount of water contained in solution and to recycled glass fibres to assess the actual amount of fibres and of residual binder. TGA is a technique that provides a very precise measurement of weight variation as a function of temperature or time. It can be performed in air or inert gas (N₂) atmospheres.

The experiments were carried out with a TGA Q 500, produced by TA Instruments. All the tests were performed in air atmosphere, while different ramps were set, as reported in Table 2.5.1.

Table 2.5.1. Heating ramps adopted in thermogravimetric analyses

Microalgal samples	Alkaline activator	Recycled glass fibres
From 25°C to 800°C; heating rate 10°C/min	From 25°C to 300°C; heating rate 10°C/min	From 25°C to 300°C; heating rate 20°C/min

2.5.1.2. X-ray diffraction (XRD)

X-ray diffraction (XRD) was performed to characterize the metakaolin powders. The interaction between x-rays and a crystal produces constructive interference when Bragg's law is satisfied ($n\lambda=2d\sin\theta$). This law relates the wavelength of electromagnetic radiation (λ) to the diffraction angle (θ) and the lattice spacing (d) in a crystalline sample. By scanning the sample through a range of θ angles, all possible diffraction directions of the lattice should be attained due to the random orientation of the powdered material. Conversion of the diffraction peaks to d-spacings allows identification of the mineral because each mineral has a set of unique d-spacings.

XRD analysis was performed with D8 Advance instrument, produced by Bruker, with a radiation generated at 40kV and 40 mA and 2θ ranging from 2° to 80° with a step size of 0.02°. Intensity peaks of diffracted X-rays were continuously recorded with scan step time 1.2 s at room temperature.

2.5.1.3. Fourier Transform Infra-Red Spectroscopy

Fourier transform infrared spectroscopy (FT-IR) was performed on different samples to evaluate whether microalgae chemically link with the geopolymer network or not. This is possible, thanks to the fact that the absorption of IR radiation can excite specific vibrational modes of molecules. Therefore, by knowing the absorption spectrum, it is possible to reconstruct the chemical structure of the sample.

Thermo Nicolet NEXUS 470 FTIR, produced by GMI Inc., was used. The analysed powders were blended with potassium bromide (KBr) powder, ground together and then pressed with a hydraulic press into thin disks of diameter 13 mm under 8 tons for 3 min. Then, IR spectra region $4000 - 400 \text{ cm}^{-1}$ were recorded at room temperature. Each spectrum was an average of 64 scans at a resolution of 4 cm^{-1} . Spectra analysis was done using OMNIC Spectra Software (by Thermo Scientific).

2.5.2. Rheology

Rheological characterization is carried out to understand the behaviour of the pastes during the extrusion and how this is influenced by the additives. Moreover, rheological properties of the material, such as yield stress and recovery ability, can be related to printability and to the development of printed objects in Z-direction.

All measurements have been performed with the stress-controlled rotational rheometer Kinexus Pro+, produced by Malvern Panalytical Ltd (Figure 2.5.1). For low viscosity fluids, the geometry selected is 40 mm plate-plate, while for more viscous ones 20 mm plate-plate geometry is preferred, to apply higher values of stress.



Figure 2.5.1. Rotational rheometer Kinexus Pro+.

For each test a sample has been prepared. If not explicitly specified, the test is carried out immediately after the paste preparation. Temperature was always set at 25°C.

Several types of test are performed:

- Shear stress ramp applied on highly viscous pastes: after a preshear at rate 100 s^{-1} for 25 seconds and a 60 second rest, a ramp at 125 Pa/s is applied. Preshear and consequent rest is used to normalize the starting condition of all samples;
- Shear stress ramp applied on lowly viscous pastes and fluids: a ramp at rate lower than 10 Pa/s is applied, without preshear;
- Creep and recovery: a constant stress is applied until the steady state for creep compliance is reached; recovery phase is programmed to last 10% more than the creep one. The applied stress depends on the specific sample and it is selected in the range of stable flow;
- Dynamic stress sweep: after a preshear at rate 100 s^{-1} for 25 seconds and a 60 second rest, a stress ramp from 10 to 10^5 Pa is applied at constant frequency of 1 Hz . Preshear and consequent rest is used to normalize the starting condition of all highly viscous samples, while they are not applied on lowly viscous ones;

The curves obtained by shear stress ramps in steady state are then fitted with rheological models. Herschel-Bulkley model is adopted for pseudoplastic fluids showing a yield stress, according to the following equation:

$$\tau = \tau_y + K\dot{\gamma}^n \quad (1)$$

in which τ is the shear stress, τ_y is the yield stress, K is the consistency, $\dot{\gamma}$ is the shear rate, and n is the flow index [89].

For pastes and fluids which does not exhibit a yield stress, a slightly different approach is followed: a power-law fitting on the linear region of viscosity curves (in double logarithmic plot) is performed, according to the relation:

$$\eta = K\dot{\gamma}^{n-1} \quad (2)$$

which, passing to the logarithms, becomes

$$\log \eta = \log K + (n - 1) \log \dot{\gamma} \quad (3)$$

in which η is the apparent viscosity, K is the consistency, $\dot{\gamma}$ is the shear rate, and n is the flow index [89].

Each formulation is tested on more than one specimen, to verify the experimental reproducibility of the results. Fitting is performed on the average curve obtained from all the tested pastes for the same formulation. The software Origin (developed by Originlab Corporation) is used to compute the fitting. Figure 2.5.2 shows an example of the fitting procedure.

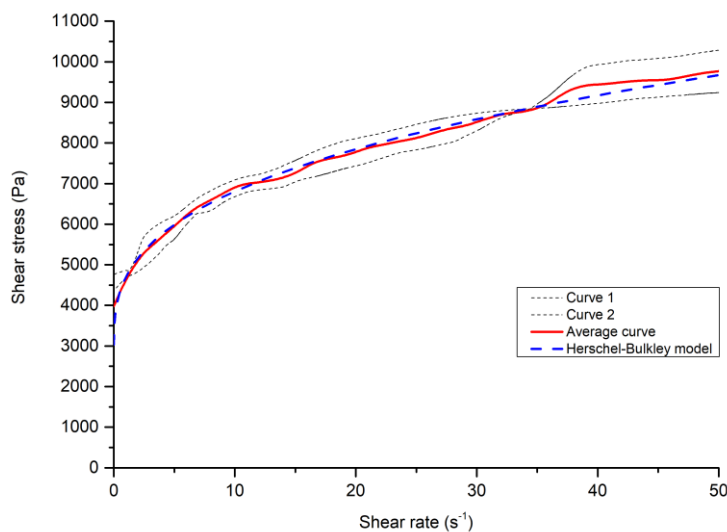


Figure 2.5.2. Fitting with Herschel-Bulkley model performed on flow curves of the formulation HB-GEO

Fitting is used to eliminate any kind of subjectivity from the extrapolation of data from the curve.

Concerning creep and recovery, creep compliance is reported as a function of time. Shear deformation (γ), which is the actual response of the material, and creep compliance (J) are proportional, according to the relation

$$J(t) = \frac{\gamma(t)}{\bar{\sigma}} \quad (4)$$

in which $\bar{\sigma}$ is the applied constant stress [90].

All recovery tests comprise three essentially separate parts once the source of stress is removed [91] (Figure 2.5.3):

- an instantaneous elastic recover (J_i);
- a retarded viscoelastic recover (J_r);
- a non-recoverable level of deformation, which is represented by a plateau of shear compliance (J_∞)

Instantaneous (X_i), retarded (X_r) and total recovery (X_{tot}) are computed as percentages, with respect to the maximum shear compliance reached:

$$X_i = \left(\frac{J_i}{J_{tot}} \right) \cdot 100\% \quad (5a)$$

$$X_r = \left(\frac{J_r}{J_{tot}} \right) \cdot 100\% \quad (5b)$$

$$X_{tot} = \left(\frac{J_i + J_r}{J_{tot}} \right) \cdot 100\% \quad (5c)$$

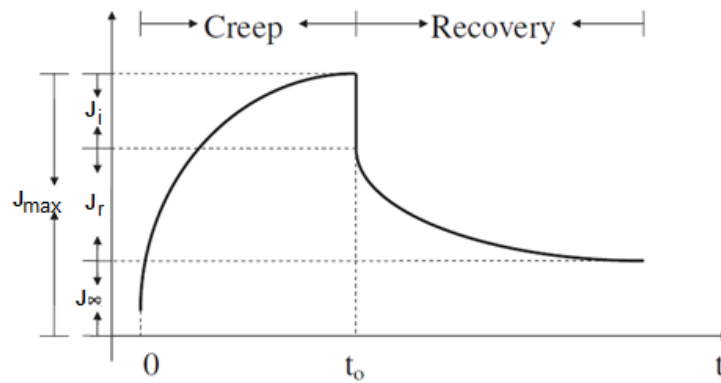


Figure 2.5.3. Model of a creep and recovery curve, in which the three different responses are highlighted. Adapted from [91]

2.5.3. Compression tests

Mechanical properties of geopolymers, casted and 3D printed, are assessed by compression tests. The tests are performed in displacement control, with the dynamometer ZwickRoell ProloLine Z010, equipped with a 10 kN load cell and square plates (Figure 2.5.4).

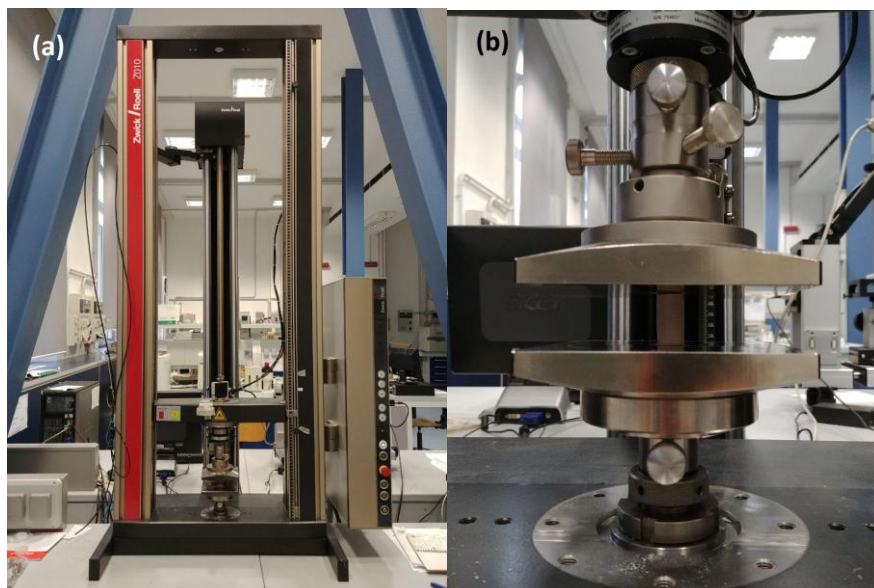


Figure 2.5.4. (a) ZwickRoell Z010 dynamometer equipped with square plates for compression test; (b) plates during the test of a sample

For hardened specimens, after a preload of 5N, displacement is applied at constant rate of 1 mm/min. The test finishes when the specimen displays a well-defined fracture pattern. For each specimen, compressive strength is calculated as the ratio between the maximum load sustained and the original cross-sectional area. For each formulation, at

least 5 specimens are tested, and the value of compressive strength reported in the results is computed as the average of the compressive strength of each specimen. The error is evaluated as standard deviation, considering all the averaged values.

For fresh samples, displacement is applied at 10 mm/min. No preload is employed.

2.5.4. Scanning electron microscope (SEM) and Energy-dispersive X-ray spectroscopy (EDS)

A scanning electron microscope (SEM) is a type of microscope that produces images of a sample by scanning the surface with a focused beam of electrons. The interaction between the electron beam and the surface of the specimen generates secondary electrons (from inelastic interactions), backscattered electrons (from elastic collisions), diffracted backscattered electrons, photons (characteristic X-rays and continuum X-rays), visible light (cathodoluminescence), and heat. SEM images are constructed by using mainly secondary electrons and backscattered electrons.

X-rays emitted are used instead for elemental analysis (energy-dispersive X-ray spectroscopy, EDS): the radiation coming from the sample is compared with a database containing the characteristic radiations of the elements to reconstruct the composition.

The scanning electron microscope used in this work is an EVO 50 Extended Pressure, produced by ZEISS (Figure 2.5.5). It works in a continuous vacuum up to $3 \cdot 10^3$ Pa and allows the differentiation of the vacuum degree between the filament chamber and the sample holder chamber thanks to a valve system. The electron source is a LaB₆ nanocrystal. Electrons are accelerated by a potential difference of 20kV.

Analyses are carried out on fragments obtained from specimens used for compression tests by N₂ cryogenic fracture in low vacuum regime.



Figure 2.5.5. Scanning electron microscope EVO 50 Extended Pressure

Micrographs from SEM are processed with the software ImageJ, to quantify the average size of the pores. To highlight pores with respect to the matrix, the colour threshold is adjusted. The average size of the pores is found with “Analyse particles” option; a minimum and a maximum cut-off area (1 and 500 μm^2 , respectively) are set to reduce errors during image elaboration and eliminate noise.

3. Results and discussion

3.1. Preliminary studies

Some of the results achieved by the research group before the beginning of this work are necessary to complete the characterization of the raw materials and to understand the whole discussion. The following list provides a brief overview of these results. Detailed graphs are reported in the Appendix.

- TGA performed on the alkaline activator showed that the residual solid is about 38% with respect to the total weight of the solution;
- TGA of *Spirulina Platensis* and *Tetraselmis Suecica* showed a similar trend, in which three decomposition steps can be identified: at temperature lower than 180°C, dehydration occurs; between 180°C and 540°C a massive weight loss is related to the decomposition of proteins, carbohydrates and lipids; after 540°C the residual carbonaceous matter continues to decompose with a very slow rate, until solid residue reaches a plateau;
- TGA of recycled glass fibres demonstrated that glass fibre content in the recycled material is quite low (32 ± 2 % for the red recycled and 11.9 ± 0.1 % for the white recycled);
- XRD on metakaolin showed a background without a well-defined baseline, which is typical of amorphous structures. The crystalline peaks found can be attributed to muscovite impurities;
- FT-IR spectra of microalgae evidenced a very complex structure. Functional groups typical of proteins, saccharides, lipids and other nutrients are found. FT-IR of geopolymer are characterized by Si-O-Si and Si-O-Al stretching vibrations. The addition of microalgae to geopolymer was investigated before and after geopolymerization and no new peaks appeared. This result demonstrates that no chemical bonds are formed between microalgae and geopolymer network.

3.2. Unfilled geopolymer

Before focusing on the main results of this work, which are related to the addition of microalgal biomass and other fillers to geopolymer matrix, the properties of the unfilled material are reported.

Since 3D printable pastes are prepared by adding bentonite to the slurry made of metakaolin and alkaline activator, the effect of the amount and the type of bentonite is clarified in terms of rheological and mechanical properties.

3.2.1. Metakaolin and activator

As mentioned in § 2, all the formulations tested are based on a slurry made of metakaolin and activator, to which bentonite and other fillers are added. From a rheological point of view, the activator exhibits a Newtonian behaviour, showing a constant viscosity of $3 \cdot 10^{-2}$ Pa·s (Figure 3.2.1a).

Rheological behaviour becomes pseudoplastic when metakaolin powder is added to the activator solution, as shown by Figure 1b. The pseudoplastic interval ranges from 10^{-2} s⁻¹ to 3 s⁻¹. At lower and higher shear rates, the behaviour is Newtonian, with two plateau levels at viscosity $2 \cdot 10^2$ Pa·s and 5 Pa·s, respectively. The parameters of the power law, fitted according to Equation (3), are $n = 0.43$ and $K = 13 \pm 1$ Pa sⁿ. No yield stress is found.

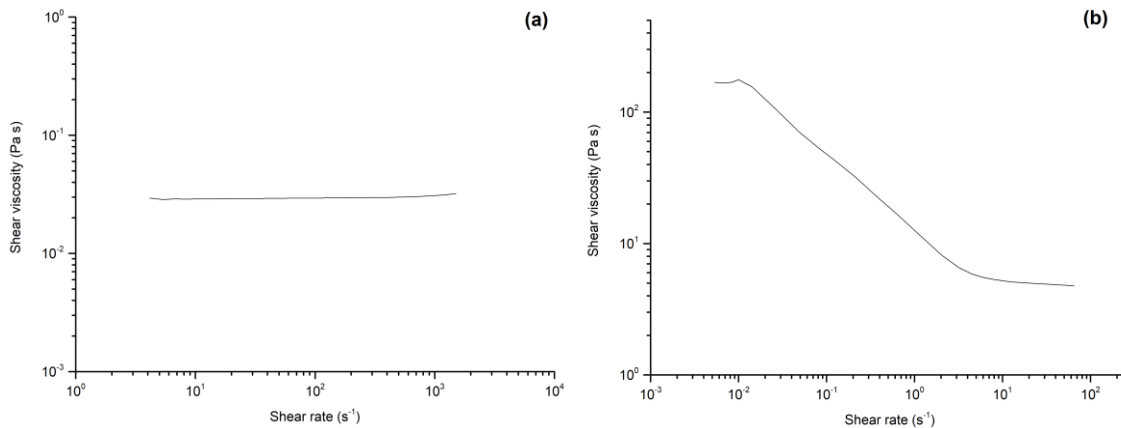


Figure 3.2.1. Viscosity curve of the alkaline activator (a) and of geopolymer (only metakaolin and alkaline activator) (b)

3.2.2. Effect of bentonite addition

The addition of bentonite affects the rheological properties of the paste as well as the mechanical properties of hardened specimens. Table 3.2.1 summarises the rheological parameters obtained fitting the flow curves according to Equations (1) and (3); the absence of data for 30 wt% of bentonite is due to the impossibility to obtain a homogeneous mix at that concentration.

Table 3.2.1. Effect of bentonite addition on rheological properties

Sample	Bentonite wt%	Yield stress (Pa)	K (Pa s ⁿ)	n	R ²
B-0	0	0 ± 0	13 ± 1	0.43 ± 0.00	0.999
B-7.5	7.5	167 ± 16	2183 ± 18	0.62 ± 0.01	0.965
B-15	15	2864 ± 241	2444 ± 212	0.53 ± 0.03	0.984
B-22.5	22.5	3371 ± 7	4264 ± 4	0.62 ± 0.00	0.999
B-30	30	-	-	-	-

From the data, it is evident that bentonite addition increases the viscosity of the paste, in terms of consistency, flow index and yield stress. Particularly important is the increase of yield stress, which has a twofold effect. From one hand, it can be related to the buildability of a 3D printed object, that is the ability to sustain the weight of the structure, increased layer by layer, without any other support. Expressing buildability as the maximum height of a structure (H), the relation with yield stress (τ_y) is the following:

$$H = \frac{\alpha}{\rho g} \tau_y \quad (6)$$

in which α is a geometrical parameter, ρ is the density, and g is the gravity acceleration. Therefore, from this perspective, the increase of yield stress is beneficial, as it leads to the improvement of buildability [92], [93].

Nevertheless, since the flow begins when the yield stress is exceeded, a fluid with high yield stress may be too difficult to extrude, causing phenomena like plugging and rupture of the syringe, due the high pressure build-up. So, even though a yield stress is necessary to build a self-standing structure, it should be not higher than the maximum shear stress that the extrusion system can provide.

Regarding mechanical properties, the addition of bentonite was demonstrated to reduce compression strength, according to literature [94]. Data obtained from compression tests of casted cubes after 7 days of ambient curing are reported in Table 3.2.2.

Table 3.2.2. Effect of bentonite amount on compression strength of hardened cubic specimens, after 7 days of ambient curing

Sample	Bentonite wt%	Compression strength (MPa)
B-0 (C-GEO)	0	40.9 ± 6.8
B-7.5	7.5	22.8 ± 1.1
B-15 (LB-GEO)	15	21.9 ± 2.5
B-22.5	22.5	21.7 ± 3.6
B-30	30	14.8 ± 2.5

The main reductions of mechanical properties occur passing from 0 wt% to 7.5 wt% amount of bentonite and for the sample at 30 wt%. In between, a sort of plateau is found.

Yield stress and compression strength, changing with respect to bentonite wt%, are plotted in Figure 3.2.2. An optimum point, in which shear yield stress is sufficiently high and compressive strength is not too low, is found at 15 wt% of bentonite.

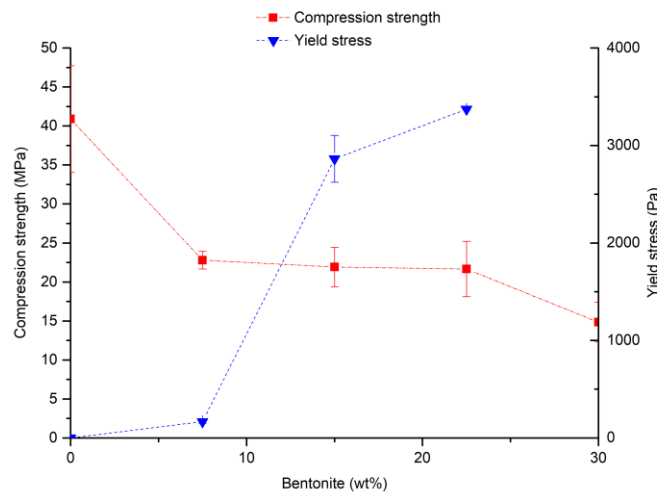


Figure 3.2.2. Yield stress and compression strength plotted against the amount of bentonite

Despite the lower mechanical properties at 7 days, bentonite acts as a fine aggregate in geopolymer mortars, lessening the effects of drying shrinkage [43]. The reduction in volume due to the progressive setting of the material and to the evaporation of residual water, in fact, can lead to the formation of cracks, which worsen the durability.

As can be seen from SEM micrographs, cracks are progressively reduced as bentonite quantity is increased. The filling effect of bentonite is also demonstrated by the reduction of average pore size, which is evaluated with the software ImageJ, following the procedure explained in § 2.5.4. As a consequence, the drop of compressive strength can be explained by the lower resistance of bentonite, with respect to geopolymer matrix, not by porosity.

Comparing the micrographs, it can be also noticed that large crystallites (diameter > 10 µm) are present even in the sample without bentonite, and so they are not directly related to its addition, but to impurities present in metakaolin. EDS analyses (Figure 3.2.3) show that these crystallites are based on Ca, while the surrounding amorphous matrix is mainly constituted by Si, O and Al atoms, which are the components of the geopolymer network.

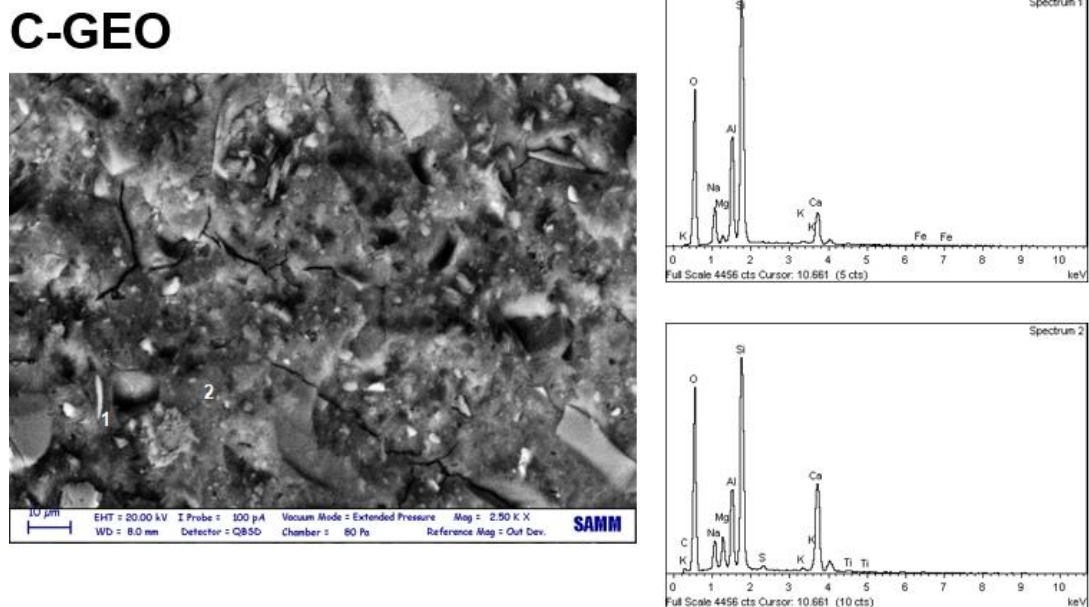
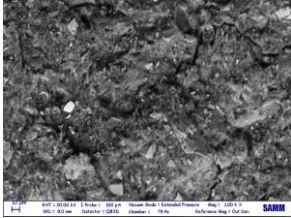
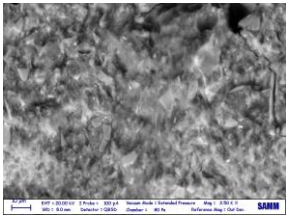
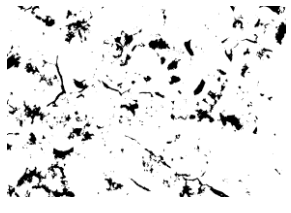



Figure 3.2.3. SEM micrograph and EDS analysis of sample C-GEO

The absence of visible bentonite particles suggests that bentonite is mixed well or even that it may take part in the geopolymerization reaction, as proposed in some studies [95].

SEM micrographs and porosity analysis are reported in Table 3.2.3.

Table 3.2.3. Comparison between samples without and with bentonite: SEM micrographs and ImageJ analyses of porosity

Sample	C-GEO (0 wt% bentonite)	LB-GEO (15 wt% bentonite)
SEM micrograph		
Processed image		
Average pore size (μm^2)	12.36	10.74

The beneficial filling effect of bentonite is also evident upon annealing. Annealing performed on cylindrical casted samples of unfilled geopolymer provoked the formation of cracks and an unwanted reduction of mechanical properties from 40.1 ± 9.3 MPa to 25.3 ± 6.5 MPa. Samples containing bentonite, on the other hand, took advantage of thermal treatment, since the action of bentonite as filler prevented embrittlement and uncontrolled shrinkage. The beneficial effect of annealing on samples containing bentonite and its effect on mechanical properties are deeply discussed in § 3.3.

3.2.3. Effect of bentonite type

Three different commercial bentonites were tested. The effect of the type of bentonite on rheological behaviour of the pastes is reported in Figure 3.2.4, and Herschel-Bulkley's model parameters, computed from fitting according to Equation (1), in Table 3.2.4.

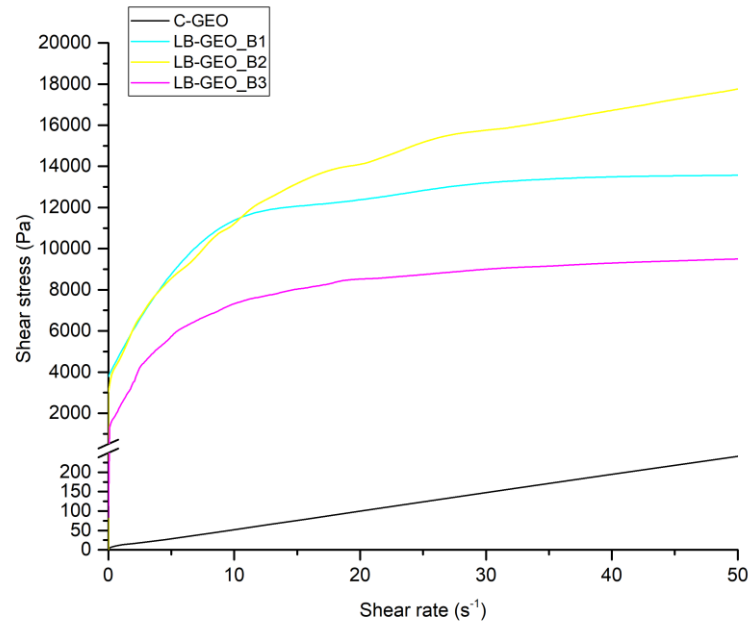


Figure 3.2.4. Flow curves of geopolymer pastes (low-bentonite formulation) containing different kinds of commercial bentonites

Table 3.2.4. Parameters of Herschel-Bulkley's model fitted on the flow curves of geopolymer pastes, containing different types of bentonite

Sample	Yield stress (Pa)	K (Pa s ⁿ)	n	R ²
C-GEO	0 ± 0	13 ± 1	0.43 ± 0.00	0.999
LB-GEO_B1	2864 ± 241	2444 ± 212	0.53 ± 0.03	0.984
LB-GEO_B2	1471 ± 17	2513 ± 21	0.44 ± 0.00	0.988
LB-GEO_B3	380 ± 15	2660 ± 17	0.48 ± 0.00	0.989

In all the cases, when bentonite is present, a yield stress is found. While consistency and flow index are similar, the value of yield stress is different. This result

suggests that the formulation should be slightly changed according to the bentonite used, particularly in the case of B3, whose value of yield stress is very low.

Mechanical properties are much less affected by the different kind of bentonite. Compression tests, carried out on 3D printed hollow cylinders made of unfilled geopolymer with LB formulations, showed that the value of compression strength after 7 days of ambient curing is practically the same (Figure 3.2.5).

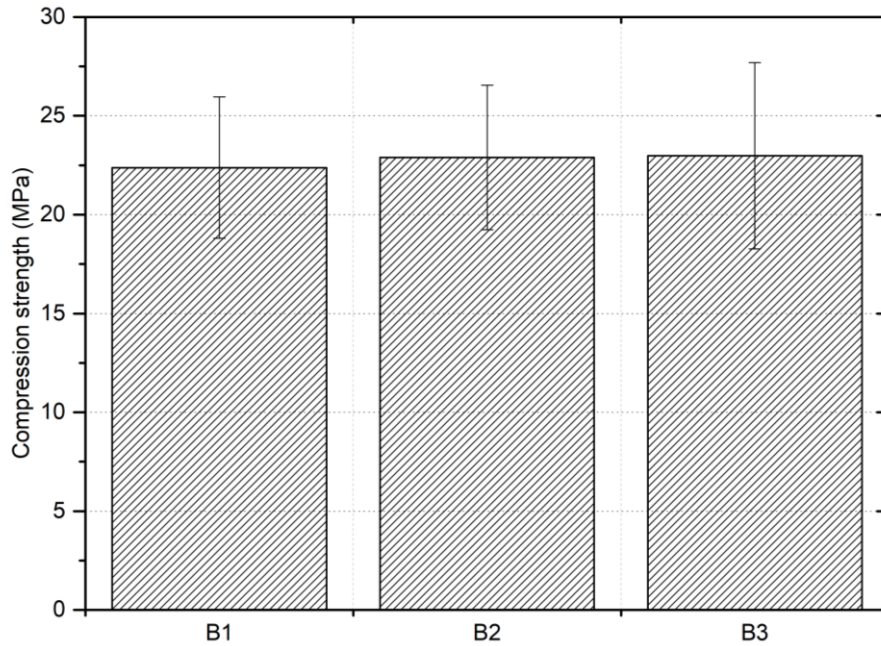


Figure 3.2.5. Compression strength of 3d-printed specimens after 7 days of ambient curing. Comparison between different bentonites and formulations

3.3. Geopolymers filled with microalgae

This work is part of the European project SaltGae, whose aim is the valorisation of microalgal biomass used for wastewater treatment. As already mentioned in § 2.2.1, two different approaches have been followed to produce 3D printable pastes, containing biomass: for HB formulation, bentonite was added in high amount and water was used to adjust rheology, while for LB formulation, a lower amount of bentonite was added and W/S ratio was kept constant.

In this chapter all the results coming from the study of rheology, mechanical properties and scanning electronic microscopy of geopolymer formulations containing biomass are reported and discussed.

3.3.1. High-bentonite formulation

3.3.1.1. Rheological behaviour of the pastes

Flow curves of the geopolymer pastes filled with 1, 3 and 5 php (with respect to the powders) of *Spirulina* and *Tetraselmis* are reported in Figure 3.3.1 and Figure 3.3.2, respectively.

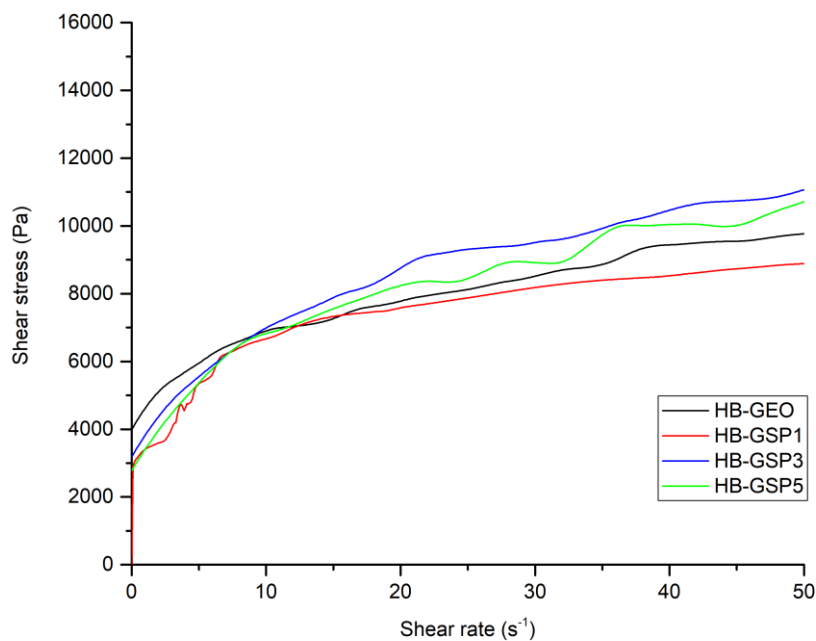


Figure 3.3.1. Flow curves of high-bentonite printable pastes, containing *Spirulina*

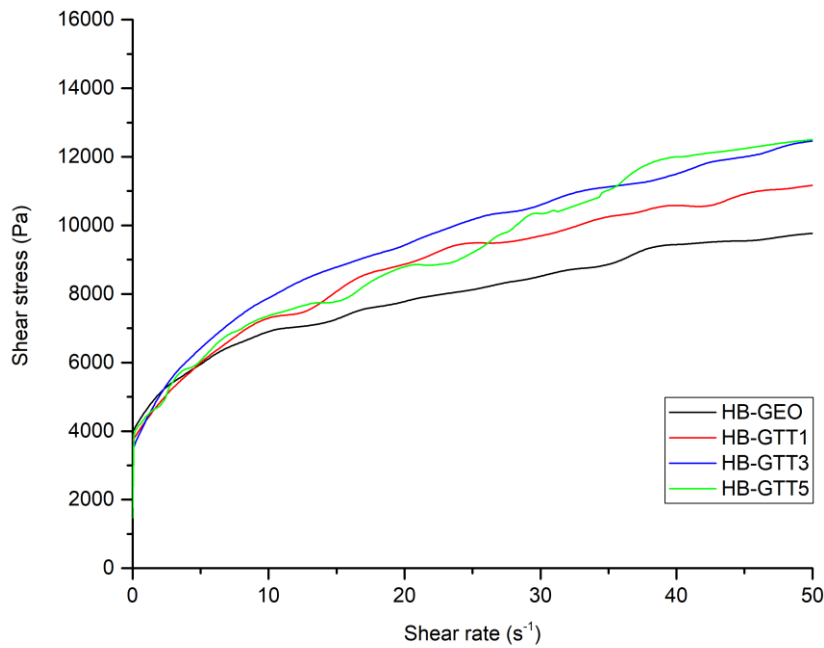


Figure 3.3.2. Flow curves of high-bentonite printable pastes, containing *Tetraselmis*

Qualitatively, the rheological behaviour of the pastes is not highly affected by the type and by the amount microalgae added. A more complete description comes from the fitting of the curves with Herschel-Bulkley's model (Table 3.3.1).

Table 3.3.1. Parameters of Herschel-Bulkley's model for HB formulations, containing biomass

Sample	Biomass php (powder)	Yield stress (Pa)	K (Pa s ⁿ)	n	R ²
HB-GEO	0	2984 ± 55	1717 ± 42	0.35 ± 0.00	0.993
HB-GSP1	1	1195 ± 29	2479 ± 40	0.25 ± 0.00	0.952
HB-GSP3	3	1040 ± 75	2847 ± 56	0.32 ± 0.00	0.996
HB-GSP5	5	1022 ± 85	2605 ± 63	0.34 ± 0.00	0.994
HB-GTT1	1	1737 ± 98	2658 ± 78	0.32 ± 0.01	0.992
HB-GTT3	3	1424 ± 72	3034 ± 54	0.33 ± 0.00	0.997
HB-GTT5	5	2670 ± 123	1733 ± 100	0.42 ± 0.01	0.984

Herschel-Bulkley's model fitted very well with all formulations. Therefore, the rheological behaviour of all the pastes is pseudoplastic ($n < 1$) with yield stress.

The most interesting result is the appreciable reduction of yield stress (plotted in Figure 3.3.3) in presence of biomass. The easier interpretation in this case is to relate this phenomenon to the higher presence of water (higher W/S ratio) in formulations

containing biomass (see § 2.2). The only difference between the two microalgal species is that for *Spirulina* this reduction is monotonic while for *Tetraselmis* there is an increase of yield stress for the paste with 5 php of biomass, which can be caused by the absorption of water by biomass.

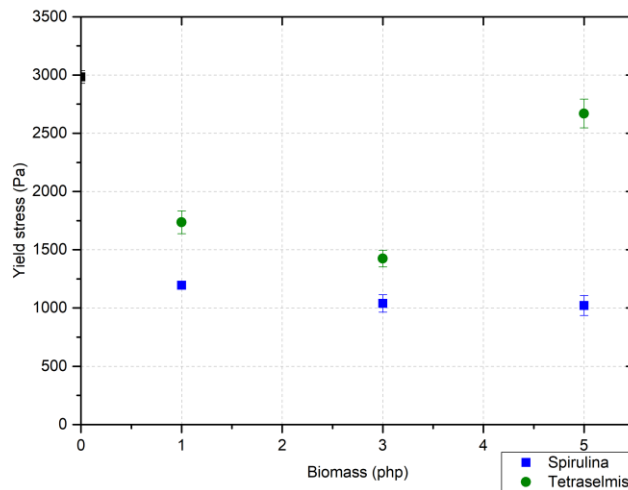


Figure 3.3.3. Yield stress against biomass amount added to geopolymer pastes with HB formulation

Once the stress is higher than the yield stress, the pastes flow. During flow, at shear rates higher than $10\text{-}15\text{ s}^{-1}$, the trend of flow curves changes: the curve of unfilled geopolymer (HB-GEO) becomes lower than the others (except HB-GSP1), meaning that the apparent viscosity (defined point by point as the ratio between stress and shear rate) at each shear rate is lower. Appreciating this behaviour from the model is less straightforward than the trend of yield stress; referring to Equation (1), the interpretation of flow passes through the parameters K , which acts as multiplying factor, and n , which is the power law exponent.

3.3.1.2. Compression tests on fresh specimens

Geopolymer is a fast setting cementitious material [18]. Therefore, obtaining reliable flow curves when the material starts to harden can be difficult. To have indications on the hardening process, tests on fresh casted samples with cylindrical geometry containing *Spirulina* were performed, following the procedure used by R.J.M. Wolfs et al. to assess the early age properties of Portland cement used for 3D printing [96].

The results are reported in Figure 3.3.4 as stress-strain curves. The first observation that can be made is that during time stress values increase, as hardening is taking place. Just after the mixing (time 0 min) the effect of biomass addition is not noticeable. The curves start to diversify after 30 minutes, when the samples with biomass start reaching higher values of stress than the unfilled one. At 60 minutes this phenomenon is even more pronounced. At 90 minutes, samples with biomass are hard enough to present a behaviour at compression that is more solid-like: the curves show a maximum, which corresponds to the point of failure. Specimen without biomass does not present this fracture mechanism at 90 minutes, keeping a plastic behaviour for longer time. A clear trend with respect to the amount of biomass is not found.

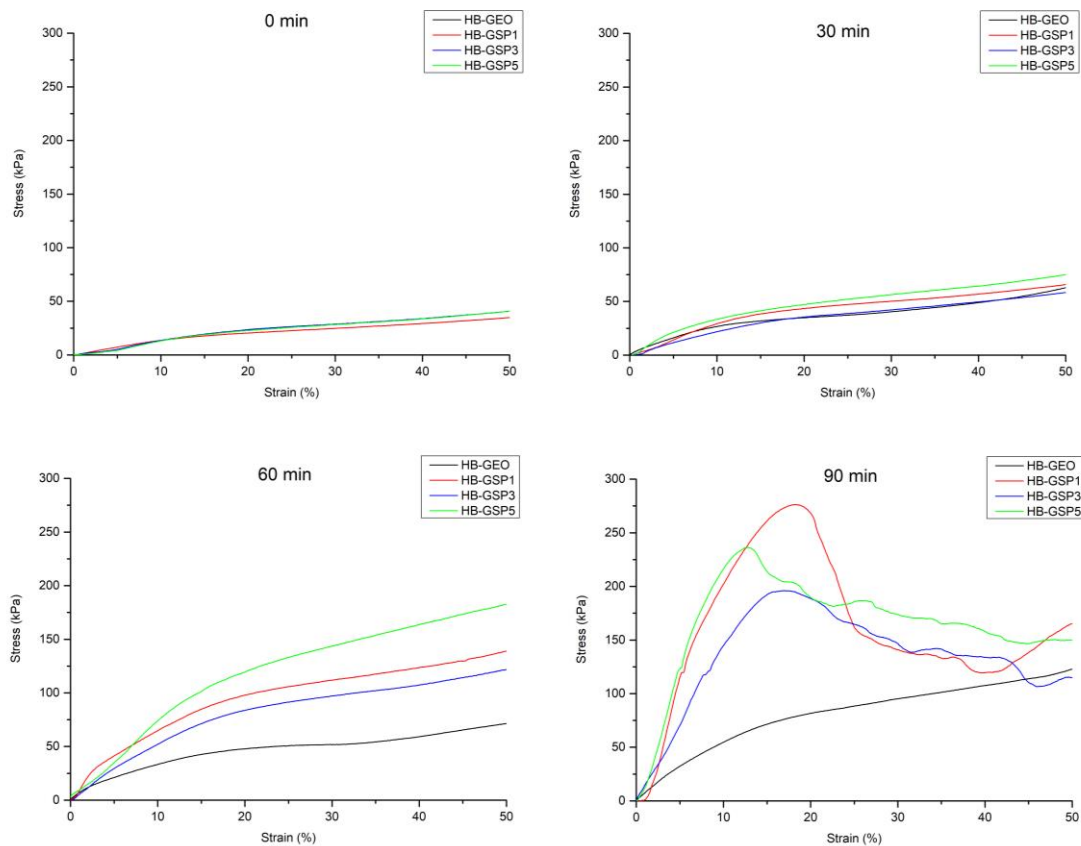


Figure 3.3.4. Stress-strain curves of fresh specimens (HB formulation, containing different amount of Spirulina), tested in compression

According to these results, biomass is an accelerating agent of the setting process in geopolymers. As discussed in § 1.3, keeping the $\text{SiO}_2/\text{Al}_2\text{O}_3$ ratio constant, the main parameter affecting setting time is the amount of water. Despite the higher W/S for formulations containing biomass, it is reasonable thinking that during time microalgae

absorb water, subtracting it from geopolymer matrix. The result is that the actual amount of water involved in the formation of the network is lower with respect to the unfilled geopolymer and, consequently, setting time is reduced.

3.3.1.3. Compression tests on hardened specimens

Compression tests were performed on 3D printed hardened specimens (hollow cylinders), containing different biomass type and concentration, after 7 or 28 days, with or without annealing. Table 3.3.2 summarizes the results obtained.

Table 3.3.2. Compressive strength values of hardened specimens with HB formulation

Sample	Biomass php (powders)	Compressive strength (MPa)			
		7 days	28 days	7 days (annealed)	28 days (annealed)
HB-GEO	0	14.7 ± 3.1	15.5 ± 3.1	38.3 ± 2.3	25.5 ± 3.2
HB-GSP1	1	14.3 ± 3.6	13.7 ± 2.5	45.0 ± 7.1	37.8 ± 7.2
HB-GSP3	3	14.2 ± 2.8	14.7 ± 4.6	46.5 ± 6.9	25.3 ± 6.6
HB-GSP5	5	13.0 ± 2.8	13.3 ± 3.5	42.3 ± 7.0	26.9 ± 4.7
HB-GTT1	1	12.9 ± 3.1	16.1 ± 3.8	38.6 ± 7.0	19.7 ± 4.5
HB-GTT3	3	13.4 ± 3.4	13.0 ± 0.5	47.3 ± 2.0	32.4 ± 5.2
HB-GTT5	5	11.6 ± 2.7	10.1 ± 0.8	46.1 ± 1.5	32.2 ± 7.1
HB-GLI1	1	12.7 ± 3.8	13.8 ± 4.6	32.1 ± 20.7	27.9 ± 10.2
HB-GLI3	3	8.9 ± 3.8	9.8 ± 1.8	24.7 ± 16.6	15.8 ± 7.4
HB-GLI5	5	8.7 ± 2.0	8.1 ± 3.3	20.2 ± 12.6	25.3 ± 7.6

Regarding non-annealed samples, it is clear that no noticeable difference exists between values of compressive strength at 7 and 28 days of ambient curing (Figure 3.3.5 and Figure 3.3.6). So, differently from Portland concrete, the plateau of mechanical properties is already obtained at 7 days. The already discussed detrimental effect of bentonite on mechanical properties (§ 3.2) can be clearly observed for all the 3D printed samples, with a decrease higher than 60% with respect to the mixture of metakaolin and activator (C-GEO).

Biomass addition slightly reduces the compressive strength. Samples containing Spirulina are the least affected by this reduction, that is always negligible if standard deviation is taken into account. The same consideration is true for formulations

containing Tetraselmis at 7 days of ambient curing, while at 28 days a more marked reduction of compressive strength is observed. Considering lignin, formulations with 3 and 5 php addition exhibit compressive strength much lower than the benchmark given by unfilled geopolymer; 1 php addition of lignin has an effect that is comparable to microalgal biomass. Therefore, microalgal biomass can be successfully used as a filler, without a noticeable depletion of mechanical properties; lignin, on the other hand, reduces too much the compressive strength of the material.

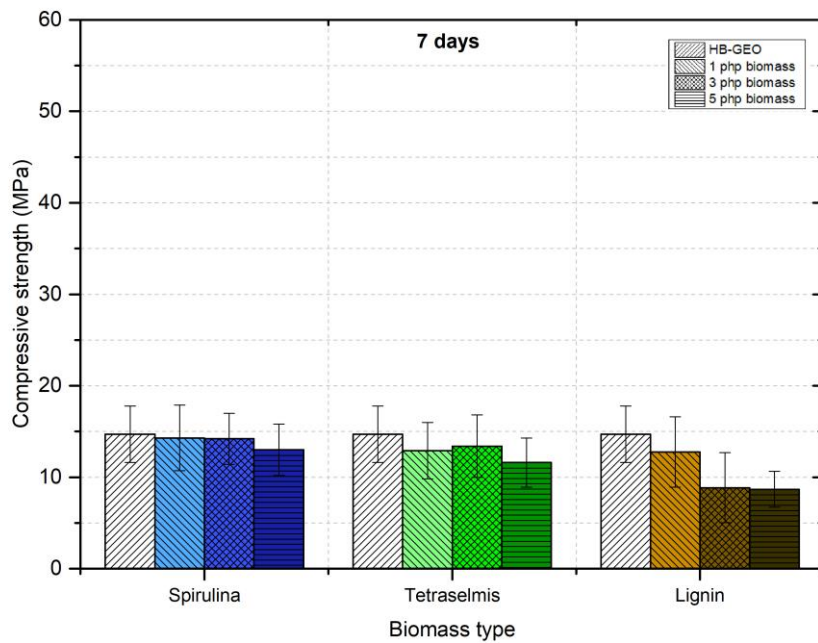


Figure 3.3.5. Compressive strength of geopolymers (high-bentonite formulation, containing biomass), tested on 3D printed hollow cylinders after 7 days of ambient curing

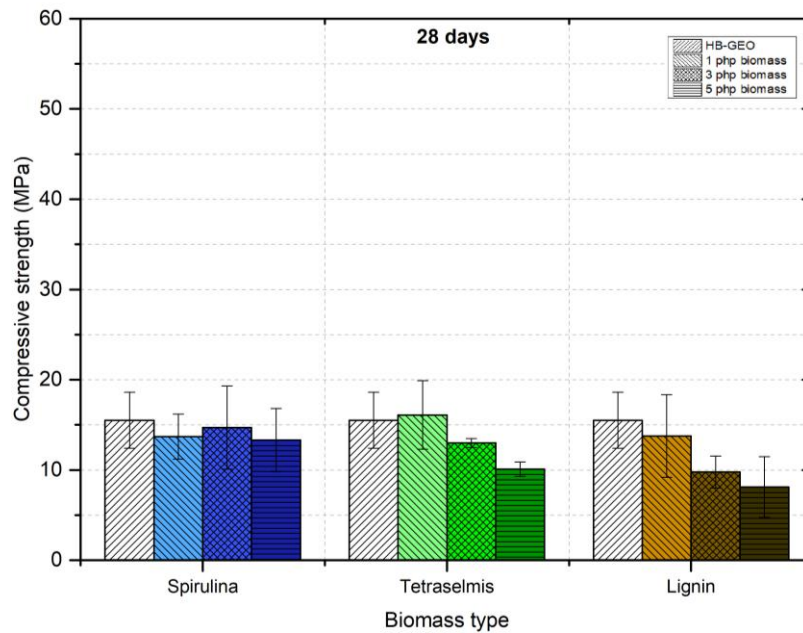


Figure 3.3.6. Compressive strength of geopolymers (high-bentonite formulation, containing biomass), tested on 3D printed hollow cylinders after 28 days of ambient curing

Annealing always improved the compressive strength of HB samples: considering the unfilled reference (HB-GEO), compressive strength grows from 14.7 ± 3.1 MPa to 38.3 ± 2.3 MPa at 7 days and from 15.5 ± 3.1 MPa to 25.5 ± 3.2 MPa at 28 days. Thermal treatment is reported to induce structural and phase composition changes in the material [18], [44]. The former ones are mainly related to sintering effects, which affect size, volume and interconnectivity of pores; the latter to melting and crystal growth or modifications in crystal structure. At the temperatures attained for thermal treatments performed in this work, only sintering processes can occur. Sintering of the geopolymer results in a closer porosity and allows for more uniform stress gradients during the application of loads, improving mechanical strength. Moreover, other beneficial effects are the improved bonding between the particles and crack healing. SEM analyses, reported in the next paragraph, are performed to have an experimental verification of these theoretical considerations.

Thermal treatment was more effective on specimens cured for 7 days than 28 days, probably because after 7 days there is still some residual mobility in the network, which eases the fast hardening induced by heat. In general, standard deviations are higher than for non-annealed specimens, meaning that the effect of annealing can change significantly

sample by sample, reducing the reproducibility of the results, particularly in the case of formulations containing lignin.

For specimens annealed after 7 days of ambient curing (Figure 3.3.7), microalgae seem to increase mechanical properties, with a peak around 47 MPa for the addition at 3 php both of Spirulina and Tetraselmis. Following the aforementioned consideration, this result must be taken just as a general indication of a possible effect of biomass, because of the high scattering of the results. Lignin effect is in all cases detrimental.

At 28 days (Figure 3.3.8), annealed specimens containing Spirulina by 1 php are the only ones which present a clear improvement with respect to the unfilled formulation. The other formulations have similar values of compressive strength, as far as the standard deviation of data is concerned. In any case, the value reached are lower than the ones obtained with an annealing after 7 days.

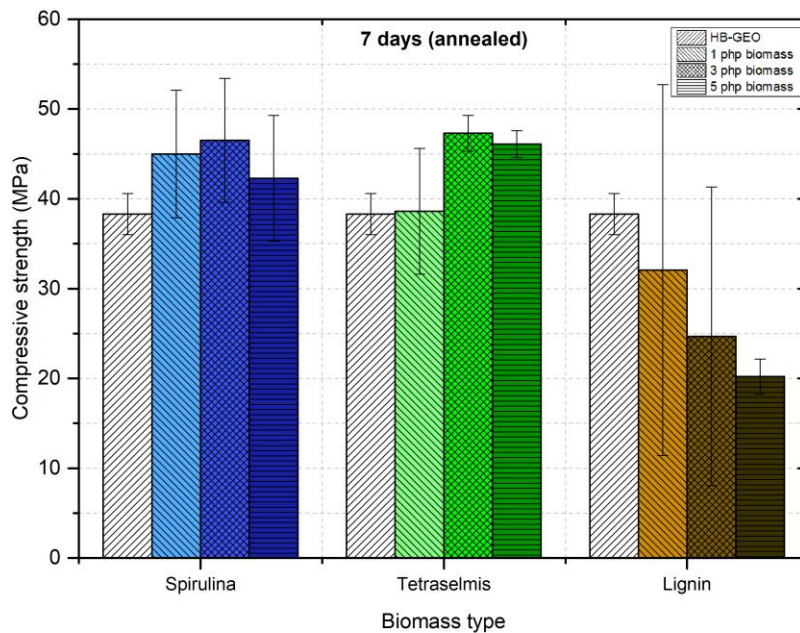


Figure 3.3.7. Compressive strength of geopolymers (high-bentonite formulation, containing biomass), tested on 3D printed hollow cylinders after 7 days of ambient curing and 4 hours of annealing at 800°C

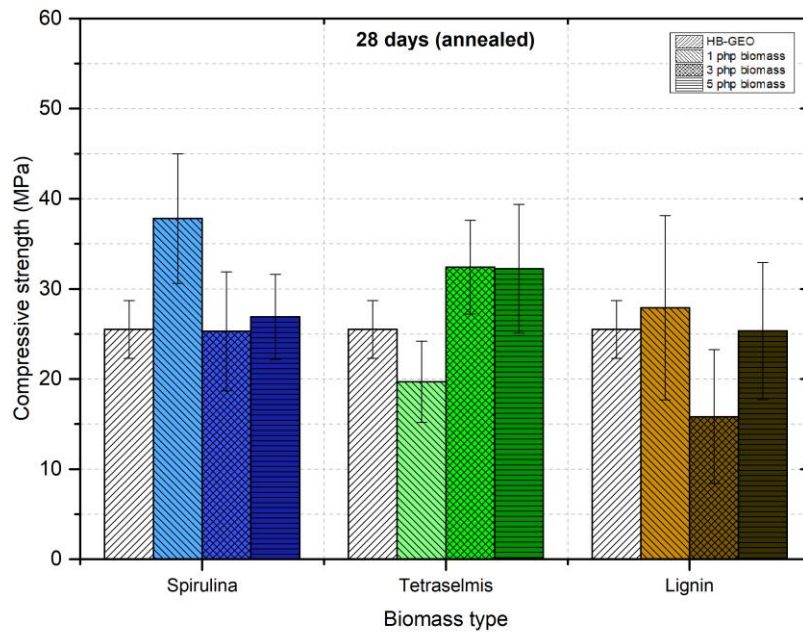


Figure 3.3.8. Compressive strength of geopolymers (high-bentonite formulation, containing biomass), tested on 3D printed hollow cylinders after 28 days of ambient curing and 4 hours of annealing at 800°C

Compressive strength of 3D printed hollow cylinders was compared to cubic and cylindrical casted samples, to understand whether the printing process influences mechanical properties or not. A complete characterization for all formulations containing Spirulina and Tetraselmis was performed on cubic specimens after 28 days of ambient curing, with or without annealing (Table 3.3.3).

Table 3.3.3. Compressive strength of geopolymers containing microalgal biomass, measured on cubic casted specimens after 28 days of ambient curing, annealed or not

Sample	Biomass php (powder)	Compressive strength at 28 days (MPa)	
		Non-annealed	Annealed
HB-GEO	0	12.9 ± 1.8	39.8 ± 1.7
HB-GSP1	1	13.7 ± 2.2	40.2 ± 5.9
HB-GSP3	3	16.7 ± 4.4	42.4 ± 0.9
HB-GSP5	5	12.9 ± 1.6	36.7 ± 6.2
HB-GTT1	1	10.9 ± 2.9	28.5 ± 5.2
HB-GTT3	3	11.9 ± 1.4	41.4 ± 2.5
HB-GTT5	5	9.5 ± 0.5	41.5 ± 4.1

The investigation on cubic casted specimens confirmed the main results obtained with 3D printed hollow cylinders: biomass addition does not change significantly mechanical properties ; annealing improved the compressive strength in all cases, but no trend with respect to biomass amount is found at the concentrations considered.

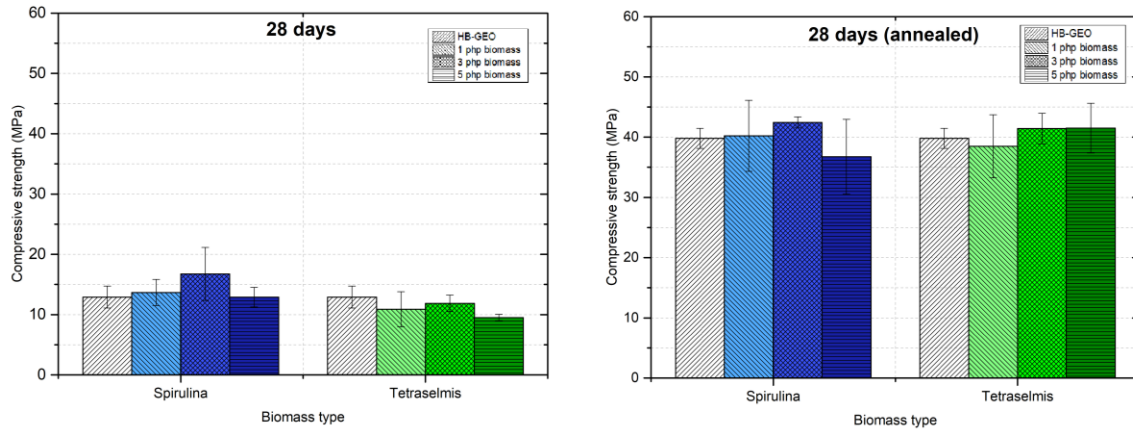


Figure 3.3.9. Compressive strength of geopolymers (high-bentonite formulation, containing biomass), measured on cubic casted samples after 28 days of ambient curing, annealed or not

Mechanical properties of samples unfilled and with 5 php addition of biomass were tested also on cylindrical casted samples. Table 3.3.4 reports the compressive strength values obtained at 28 days, without and with annealing, compared to the other geometries tested (3D printed hollow cylinders and casted cubes).

Table 3.3.4. Compressive strength of geopolymers (HB, containing biomass) tested on different kinds of samples at 28 days

Sample	Biomass php (powder)	Compressive strength at 28 days (MPa)			Compressive strength at 28 days (annealed samples) (MPa)		
		3D printed	Casted cube	Casted cylinder	3D printed	Casted cube	Casted cylinder
HB-GEO	0	15.5 ± 3.1	12.9 ± 1.8	9.7 ± 2.2	25.5 ± 3.2	39.8 ± 1.7	21 ± 5.7
HB-GSP5	5	13.3 ± 3.5	12.9 ± 1.6	9.7 ± 3.3	26.9 ± 4.7	36.7 ± 6.2	11.7 ± 4.4†
HB-GTT5	5	10.1 ± 0.8	9.5 ± 0.5	7.5 ± 2.7	32.2 ± 7.1	41.5 ± 4.1	17.5 ± 5.6†
HB-GLI5	5	8.1 ± 3.3	6.7 ± 1.9	5.5 ± 2.4	25.3 ± 7.6	40.1 ± 4.8	20.3 ± 5.5

† Samples cracked during thermal treatment.

Considering non-annealed samples (Figure 3.3.10), it is curious noticing that the best values of compressive strength are obtained with 3D printed samples. Casted cubes show comparable properties, while casted cylinders display lower values with any

biomass type. From these results some considerations on the speed of geopolymerization reaction with respect to the geometry of the sample can be made (Table 3.3.5). Since 3D printed hollow cylinders have the largest total surface area with respect to their volume, it is easier for water to evaporate and for the reaction to go on in these kinds of specimens. On the other hand, the full cylinder is the thicker specimen and there is the risk to have a central region less reacted than the outer one. The unreacted central region is characterised by a less resistant network, compromising the mechanical properties of the whole specimen.

Table 3.3.5. Surface and volume of geopolymer samples, having different geometries

Geometry	Area (mm ²)	Volume (mm ³)	Area/Volume (mm ⁻¹)
3D printed hollow cylinder	2422	2522	0.96
Casted cube	1539	4308	0.36
Casted cylinder	864	1728	0.50

Moreover, as demonstrated by rheology studies, pastes for 3D printing are much more viscous than the ones designed for casting. So, some voids may be present in samples obtained via casting with a paste formulated for 3D printing, due to its higher viscosity.

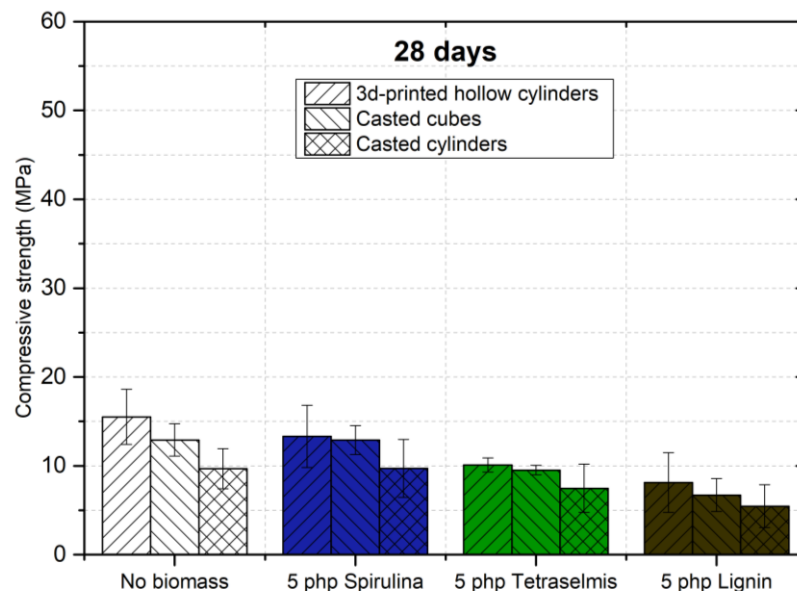


Figure 3.3.10. Comparison between compressive strength values of 3D printed and casted samples, evaluated at 28 days of curing at ambient temperature

Annealing promotes sintering phenomena and the bonding of unreacted geopolymer particles. As a consequence, the differences due to the different degrees of reaction completion evidenced by tests of non-annealed samples cannot be noticed for annealed ones. Cubes show the highest compressive strength values, because the cubic shape is able to sustain compressive loads better than the cylinder [97]. Comparing hollow and full cylinders, samples HB-GEO and HB-GLI5 show comparable compressive strength values, whereas the addition of microalgal biomass is detrimental on mechanical properties of casted cylinders (Figure 3.3.11).

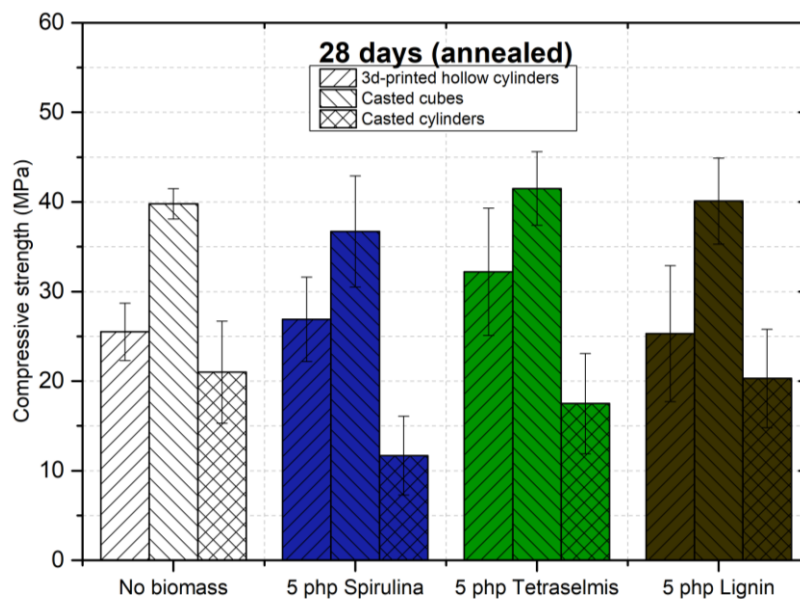


Figure 3.3.11. Comparison between compressive strength values of 3D printed and casted samples, evaluated at 28 days of curing at ambient temperature and 4 hours of annealing at 800°C

These samples appeared highly cracked before testing (Figure 3.3.12a); looking at the fracture surface after testing, a non-homogeneous structure was observed (Figure 3.3.12b). A possible explanation to this behaviour is that heat made water still contained in the central part of the specimen, in particular retained by biomass, rapidly evaporate, causing cracks on the surface; consequently, heat directly affected the central region. The visible char is probably due to burned microalgal biomass.

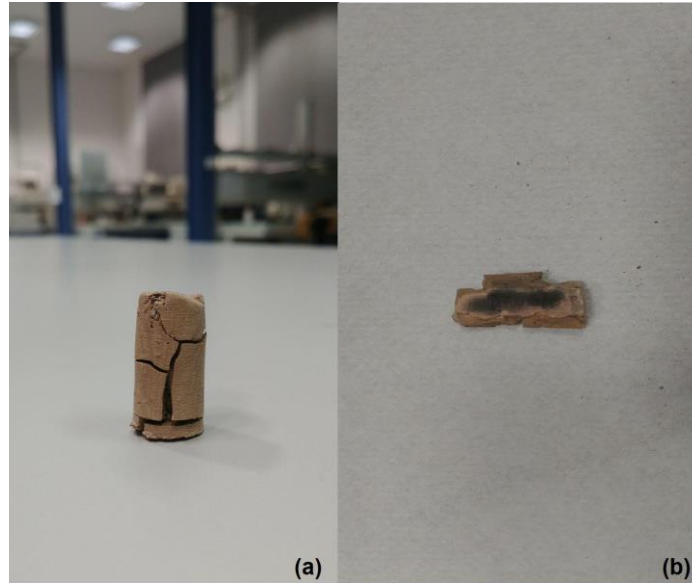


Figure 3.3.12. Example of an annealed cylindric casted specimen. Cracks are evident before testing (a) and a burning in the central region can be observed from the fracture surface (b)

In addition to microalgae and lignin, the effect of low-protein residues of *Spirulina* and *Tetraselmis* on mechanical properties of geopolymers was investigated. The results obtained are reported in Table 3.3.6.

Table 3.3.6. Compressive strength values of hardened specimens with HB formulation, containing residues of *Spirulina* and *Tetraselmis*

Sample	Biomass php (powders)	Compressive strength (MPa)			
		7 days	28 days	7 days (annealed)	28 days (annealed)
HB-GEO	0	14.7 ± 3.1	15.5 ± 3.1	38.3 ± 2.3	25.5 ± 3.2
HB-GRS1	1	12.1 ± 2.5	14.7 ± 3.1	28.6 ± 6.4	46.9 ± 2.8
HB-GRS3	3	11.0 ± 1.6	15.9 ± 3.7	38.5 ± 9.6	40.3 ± 3.0
HB-GRS5	5	10.7 ± 1.5	10.7 ± 1.7	30.9 ± 14.8	39.9 ± 6.0
HB-GRT1	1	12.8 ± 1.8	18.1 ± 5.3	46.7 ± 5.0	41.3 ± 5.3
HB-GRT3	3	12.1 ± 3.1	12.2 ± 2.6	39.6 ± 8.2	37.1 ± 8.9
HB-GRT5	5	10.1 ± 1.9	9.4 ± 2.2	43.6 ± 5.5	39.6 ± 8.3

As far as non-annealed samples are considered, the effect of residues on mechanical properties is very similar to the one of microalgae (Figure 3.3.13 and Figure 3.3.14): compressive strength is slightly reduced with the increasing concentration of additive and it does not change significantly from 7 to 28 days of ambient curing.

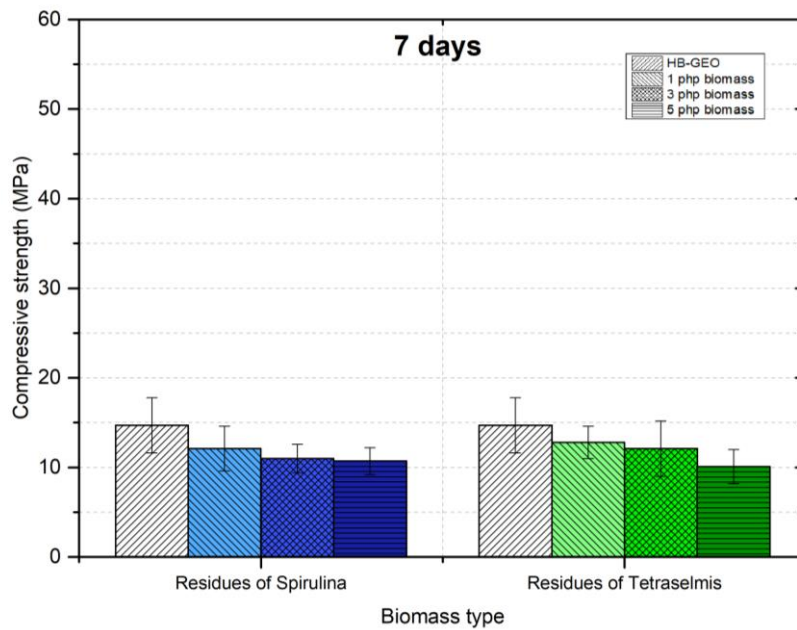


Figure 3.3.13. Compressive strength of geopolymers (high-bentonite formulation, containing microalgal biomass residues), tested on 3D printed hollow cylinders after 7 days of ambient curing

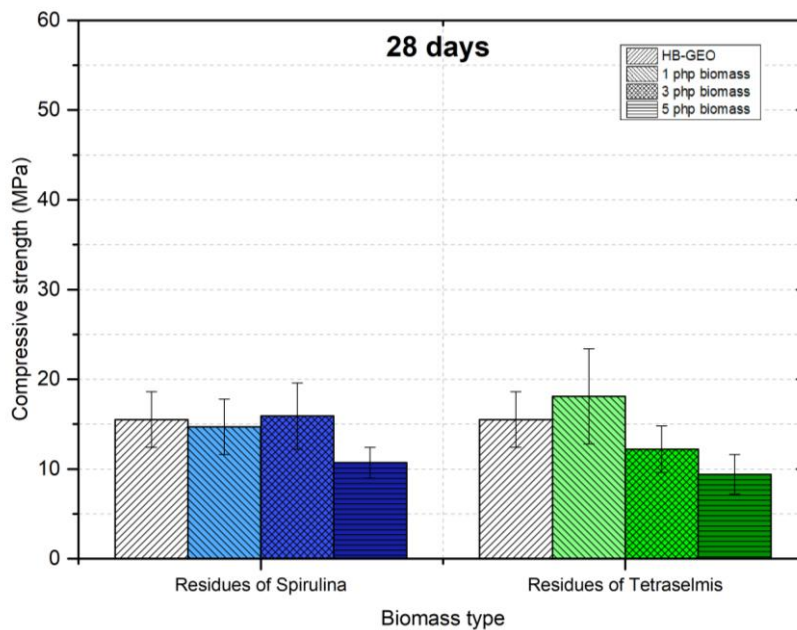


Figure 3.3.14. Compressive strength of geopolymers (high-bentonite formulation, containing microalgal biomass residues), tested on 3D printed hollow cylinders after 28 days of ambient curing

Differently from samples containing microalgae, for ones charged with residues annealing is less effective on samples aged 7 days than on ones aged 28 days. At 7 days, the addition of 1 php of residue of Tetraselmis is beneficial, while other amounts do not improve nor reduce properties. Conversely, at 28 days all the formulations with residues have improved compressive strength with respect to the unfilled geopolymer.

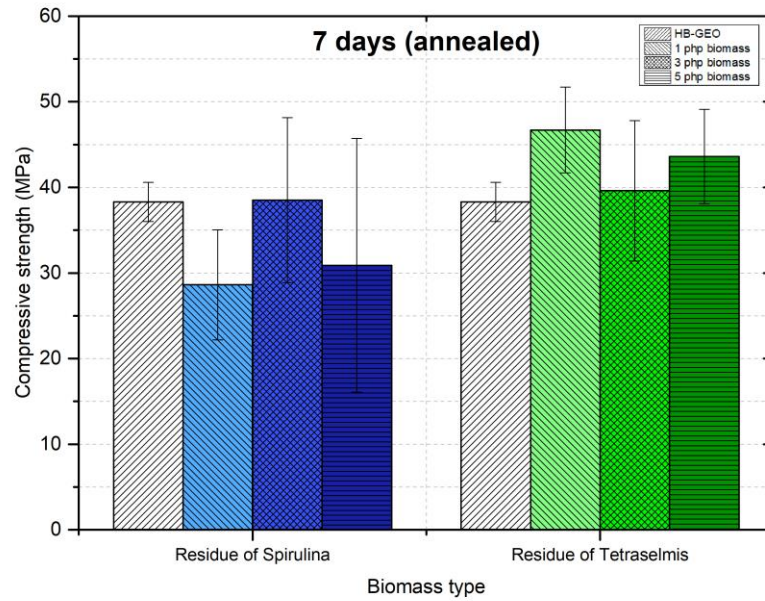


Figure 3.3.15. Compressive strength of geopolymers (high-bentonite formulation, containing microalgal biomass residues), tested on 3D printed hollow cylinders after 7 days of ambient curing and 4 hours of annealing at 800°C

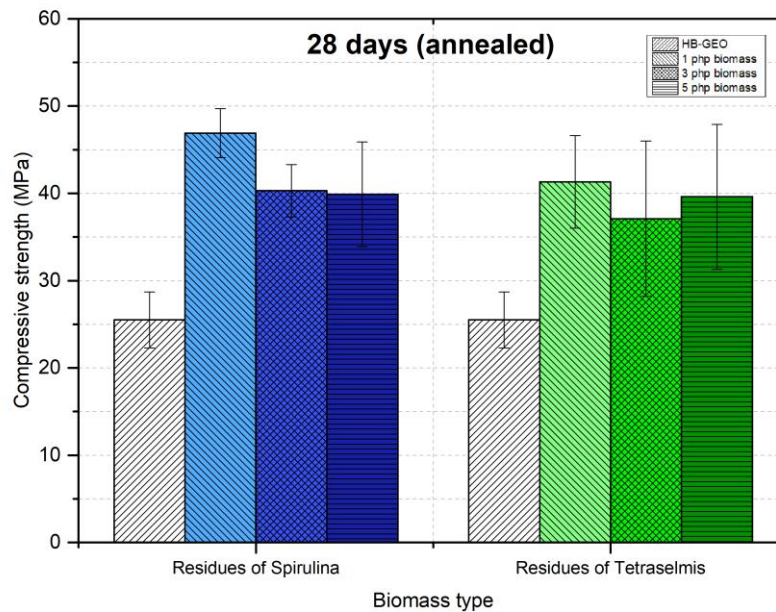


Figure 3.3.16. Compressive strength of geopolymers (high-bentonite formulation, containing microalgal biomass residues), tested on 3D printed hollow cylinders after 28 days of ambient curing and 4 hours of annealing at 800°C

3.3.1.4. SEM and EDS analyses

SEM and EDS analyses were performed on fragments belonging to 3D printed samples, tested by compression tests 28 days after their preparation, annealed and not. The formulations considered are HB-GEO, HB-GSP5, HB-GTT5 and HB-GLI5. Pictures of SEM micrographs (at two different magnification levels), with the related EDS spectra are reported in the following pages.

In all the pictures it is possible to appreciate the absence of sharp and elongated voids, which could have been present to mark the separation between different layers. Therefore, a first result is that the additive manufacturing process does not induce defects in the matrix.

SEM imaging on unfilled geopolymer (HB-GEO, Figure 3.3.17) shows a clearly amorphous matrix, some crystallites larger than 10 μm and a uniformly distributed porosity. As already observed on the casted specimen made by metakaolin and activator, EDS analysis confirmed that the matrix (Spectrum 2) is constituted mainly by Si, O and Al atoms, which forms the geopolymer network. EDS spectra of the aggregates (Spectra 1 and 3) showed a high presence of Ca, probably due to impurities in the raw materials. Their composition can suggest the formation of Ca-Si-Al gel spots in the sialate network.

HB-GEO

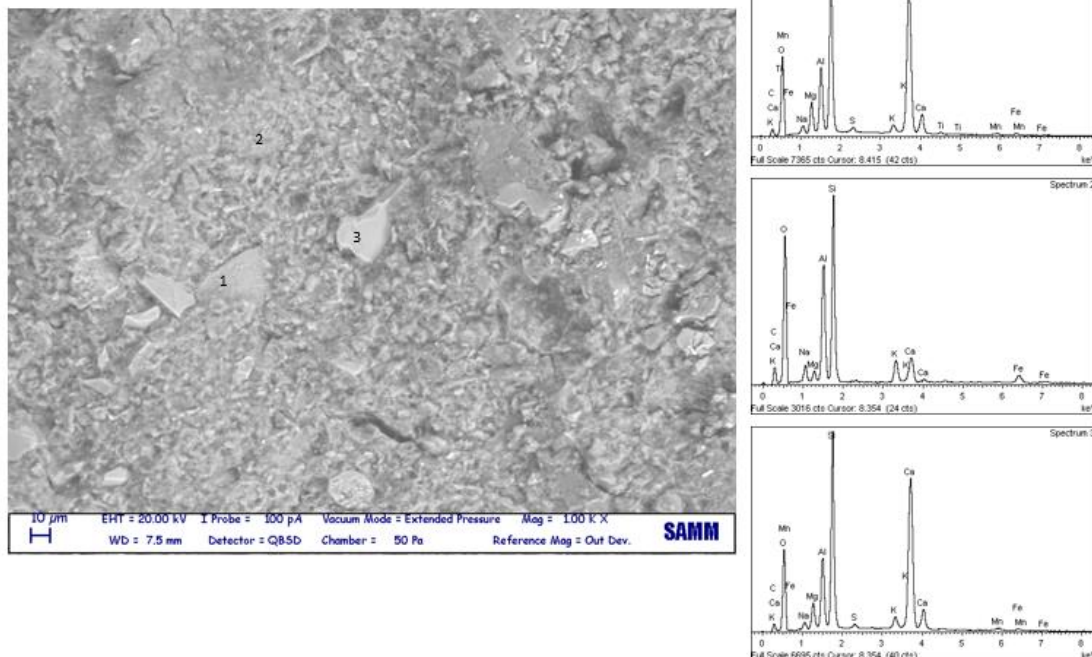


Figure 3.3.17. SEM imaging and EDS spectra of the sample HB-GEO

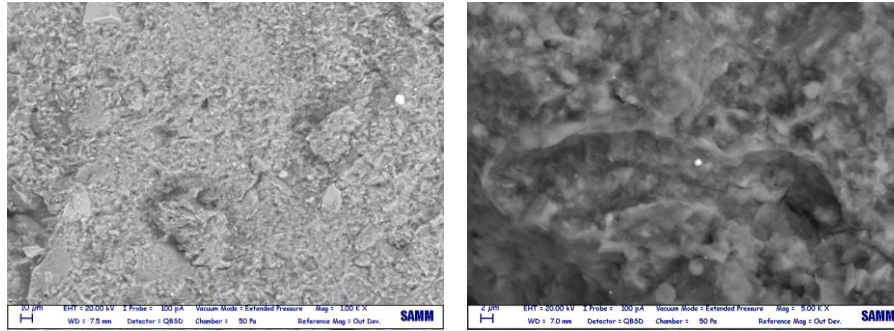


Figure 3.3.18. SEM micrographs of sample HB-GEO at different magnifications

SEM micrograph of the sample containing Spirulina (HB-GSP5, Figure 3.3.19) looks similar to the unfilled one, but more porous. EDS demonstrated the absence of carbon-based aggregates, which would have been the evidence of biomass aggregation. Thus, biomass is well mixed in the matrix, but it causes porosities, probably because it interferes in the formation of the geopolymer network. Also in this case, the matrix (Spectrum 2) is predominantly formed by Si, O and Al, while the crystallites present a high Ca concentration.

HB-GSP5

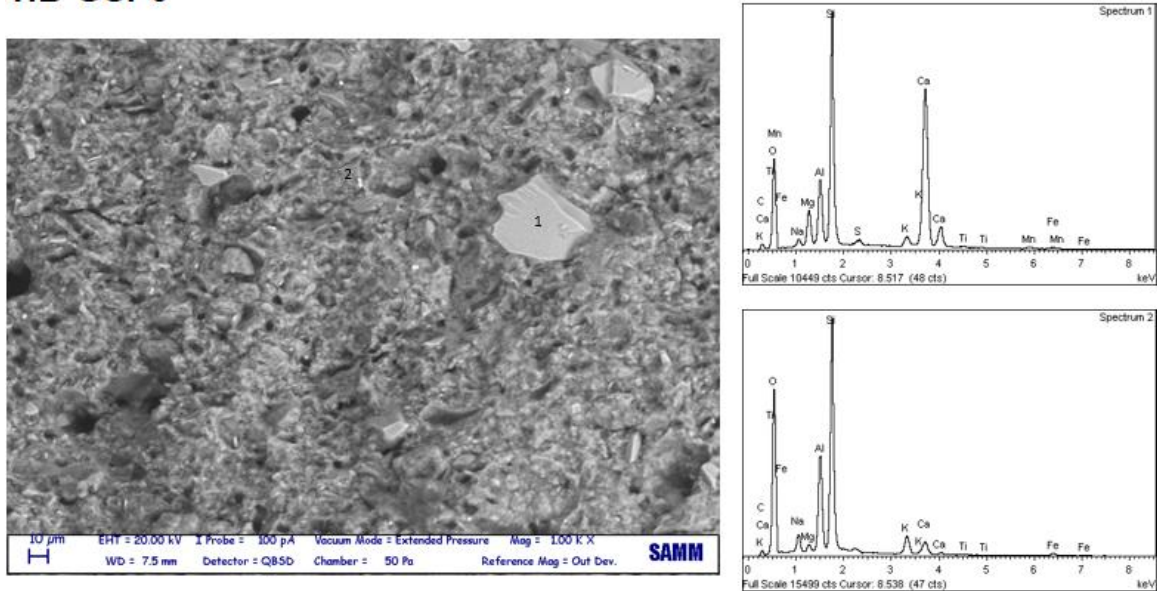


Figure 3.3.19. SEM imaging and EDS spectra of the sample HB-GSP5

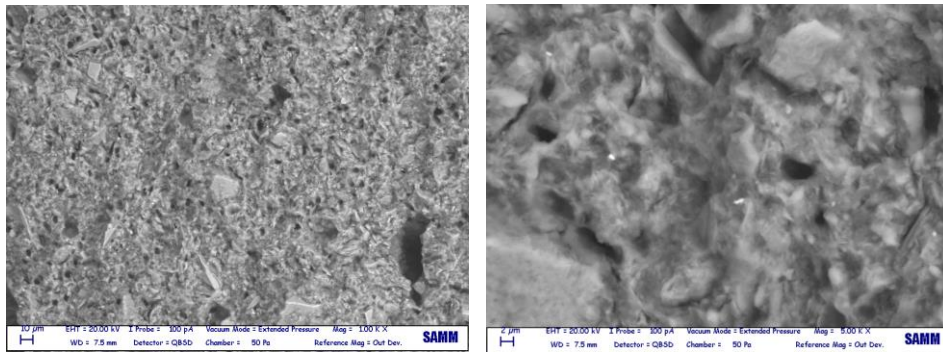


Figure 3.3.20. SEM micrographs of sample HB-GSP5 at different magnifications

The same general considerations hold also for sample containing Tetraselmis (HB-GTT5, Figure 3.3.21). Large crystallites are not found in this case, and the visible floccs are constituted mainly by metallic elements (Fe and Ni).

HB-GTT5

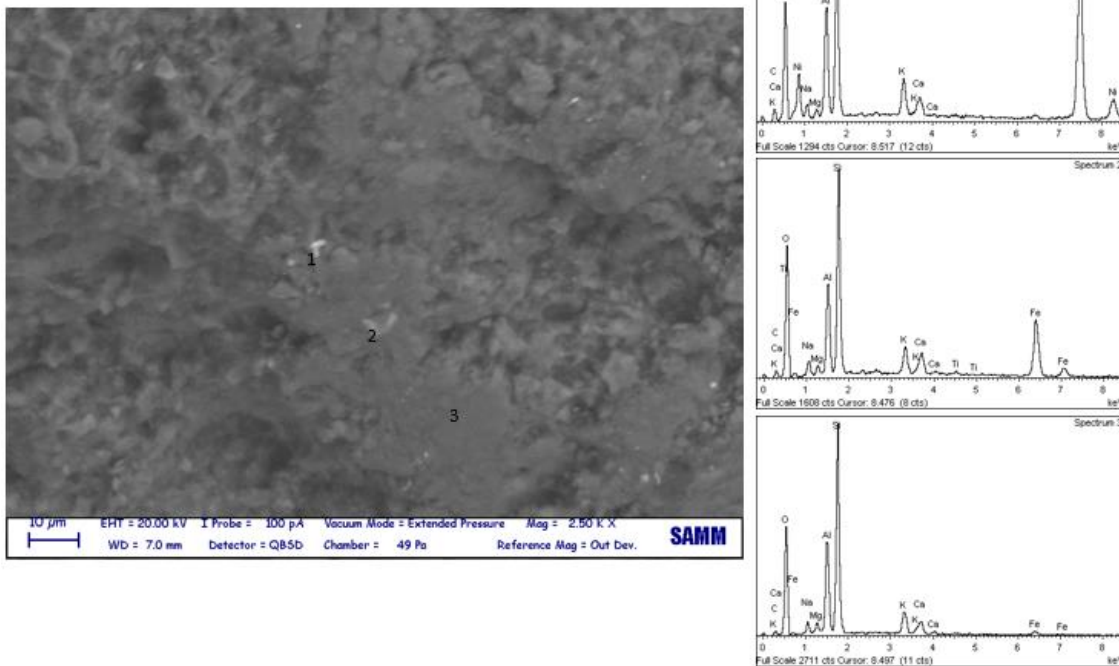


Figure 3.3.21. SEM imaging and EDS spectra of the sample HB-GTT5

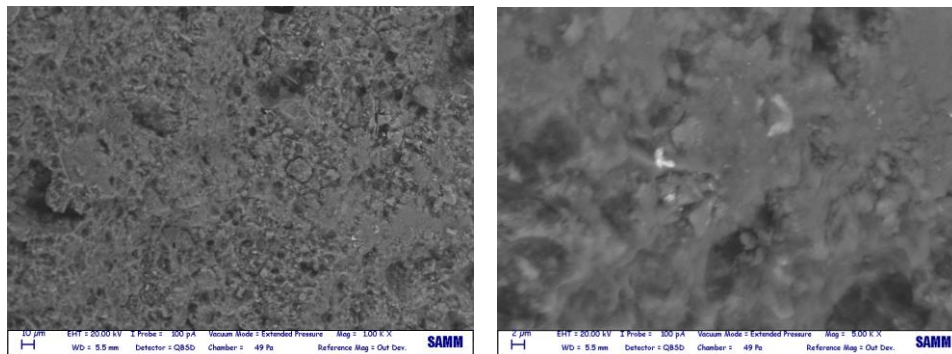


Figure 3.3.22. SEM micrographs of sample HB-GTT5 at different magnifications

Sample containing lignin (HB-GLI5, Figure 3.3.23) presents the most irregular and porous structure between all the non-annealed specimens. EDS analysis highlights the presence of CaO inclusions (Spectrum 1), as well as metallic impurities (Spectrum 2). Again, the matrix is formed mainly by Si, O and Al atoms (Spectrum 3).

HB-GLI5

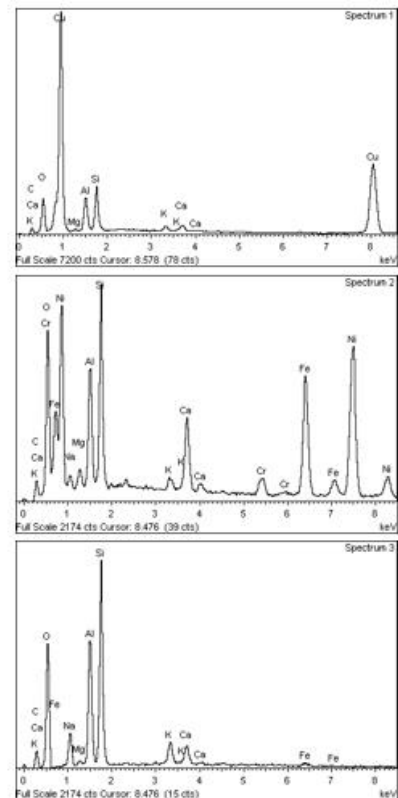
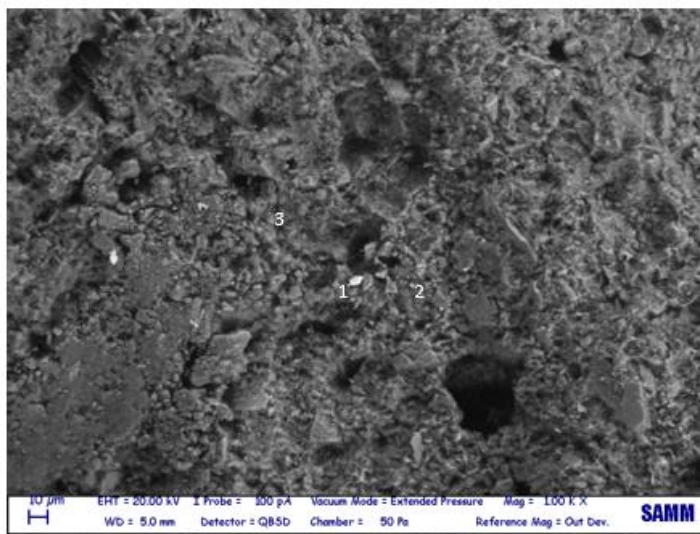


Figure 3.3.23. SEM imaging and EDS spectra of the sample HB-GLI5

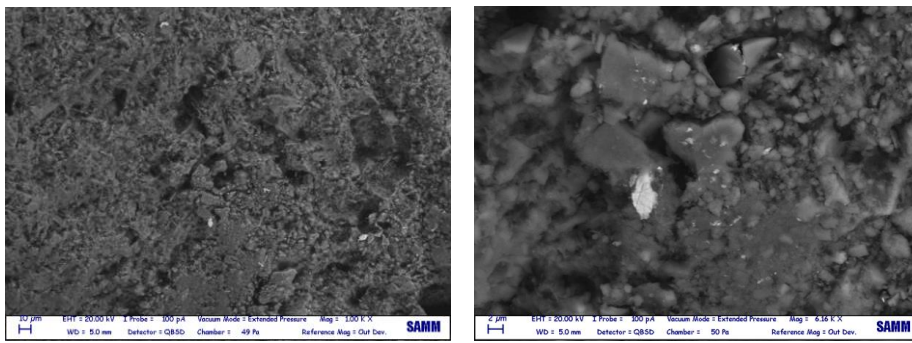


Figure 3.3.24. SEM micrographs of sample HB-GLI5 at different magnifications

Images of annealed samples show a more compact and smooth structure, with smaller pores than non-annealed ones. Pores appear more spherical and less interconnected at the surface level observed.

Elemental analysis performed by EDS gives the same results regarding matrix and flocs or aggregates. Figure 3.3.25 shows the SEM image and the EDS spectra of the annealed sample HB-GEO.

HB-GEO (annealed)

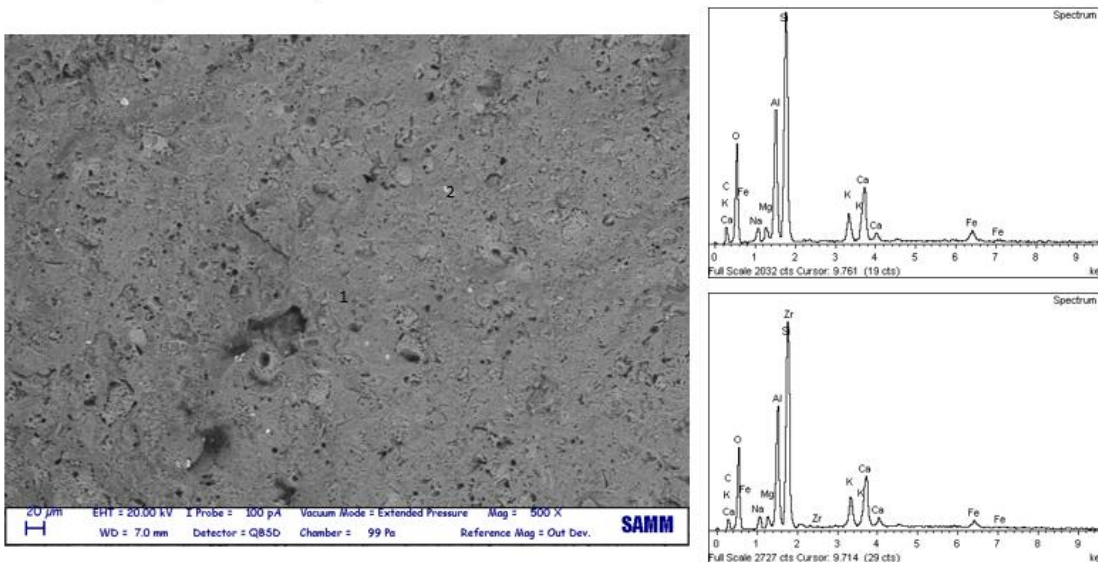


Figure 3.3.25. SEM imaging and EDS spectra of the sample HB-GEO (annealed)

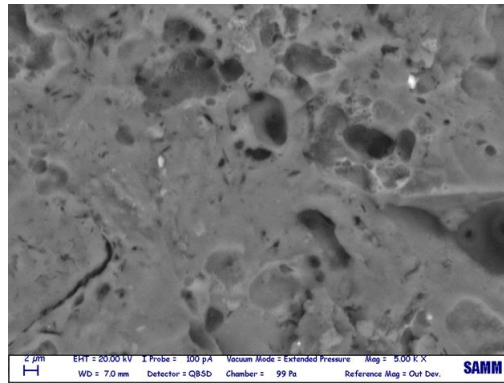


Figure 3.3.26. SEM imaging of annealed sample HB-GEO (magnified)

The effect of biomass on porosity seems to be less evident for annealed samples containing Spirulina. Figure 3.3.27 reports SEM image and EDS analysis of the sample HB-GSP5 after thermal treatment. The white spots correspond to flocks containing metallic elements (Fe).

HB-GSP5 (annealed)

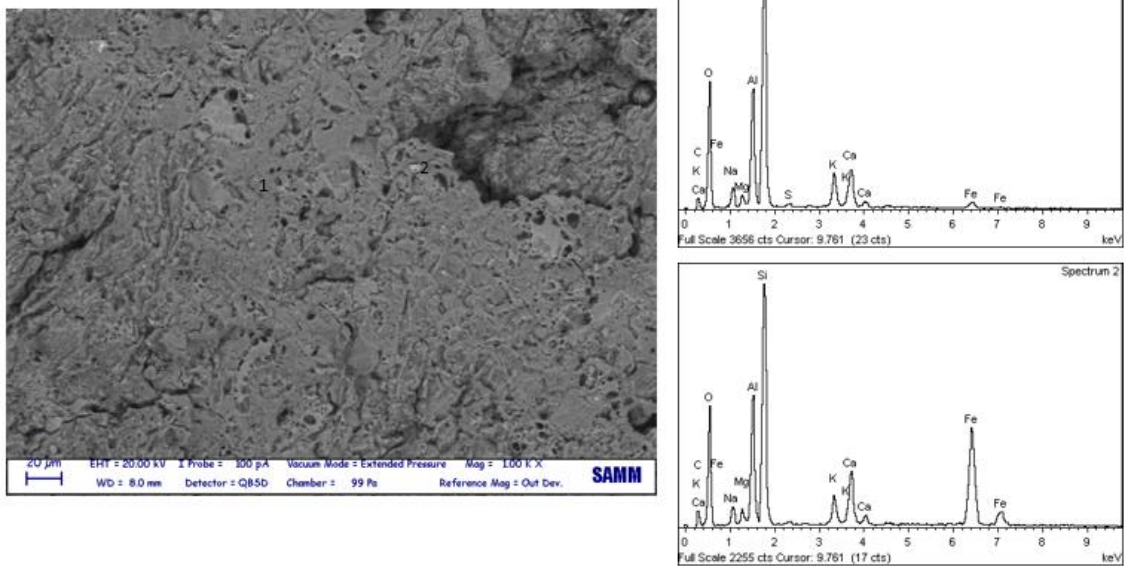


Figure 3.3.27. SEM imaging and EDS spectra of the sample HB-GSP5 (annealed)

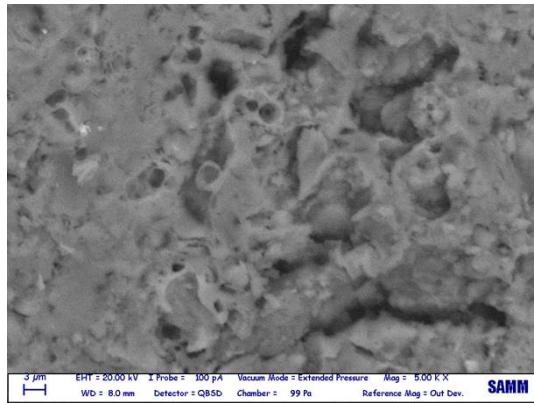


Figure 3.3.28. SEM imaging of annealed sample HB-GSP5 (magnified)

The same considerations made for the sample containing Spirulina hold also for the one containing Tetraselmis (HB-GTT5 (annealed), Figure 3.3.29).

HB-GTT5 (annealed)

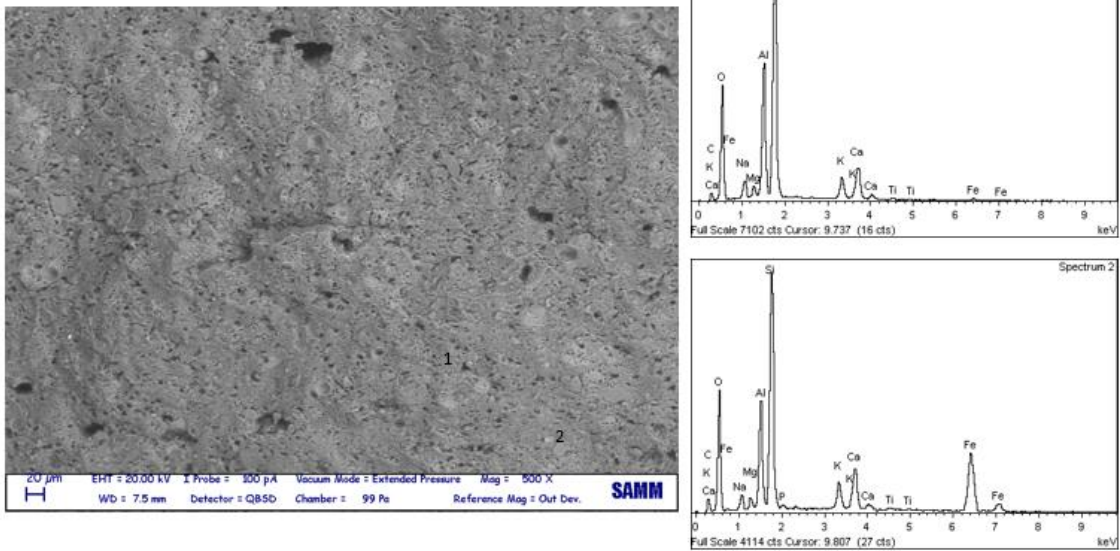


Figure 3.3.29. SEM imaging and EDS spectra of the sample HB-GTT5 (annealed)

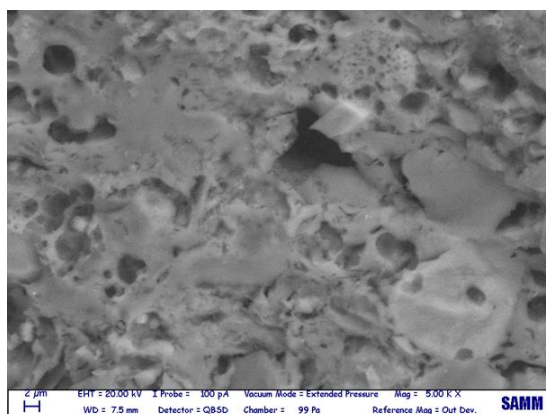


Figure 3.3.30. SEM imaging of annealed sample HB-GTT5 (magnified)

The difference between algal biomass and lignin that was found in non-annealed samples is not so evident in the thermal-treated ones. Both SEM imaging and EDS spectra of the sample HB-GLI5 (annealed), reported in Figure 3.3.31, are comparable to the previous two, containing Spirulina and Tetraselmis, respectively.

HB-GLI5 (annealed)

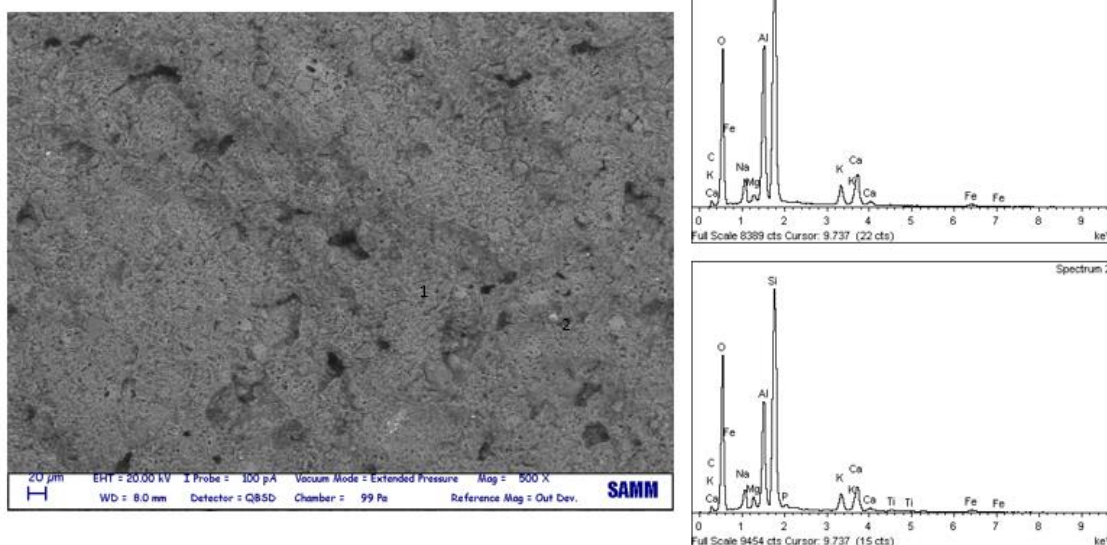


Figure 3.3.31. SEM imaging and EDS spectra of the sample HB-GLI5 (annealed)

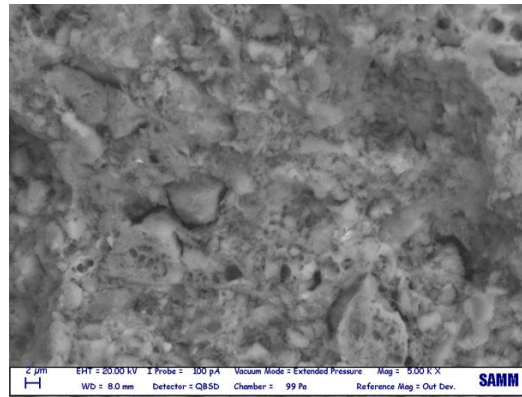


Figure 3.3.32. SEM imaging of annealed sample HB-GLI5 (magnified)

SEM micrographs were elaborated with the software ImageJ to analyse porosity (see § 2.2 for the details of the procedure adopted). In Table 3.3.7 and Table 3.3.8 the processing of the images and the results obtained are reported in terms of pore area, for specimens non-annealed and annealed, respectively. For non-annealed specimen, it is clear the increase of porosity with the addition of biomass. The same effect is not appreciable for the annealed ones.

Table 3.3.7. ImageJ analyses of non-annealed samples with HB formulation

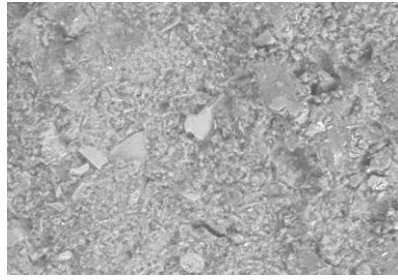
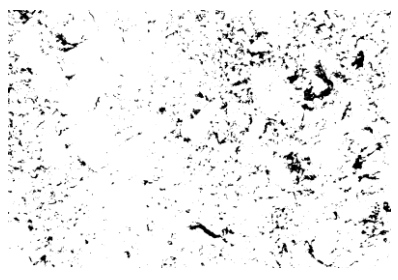
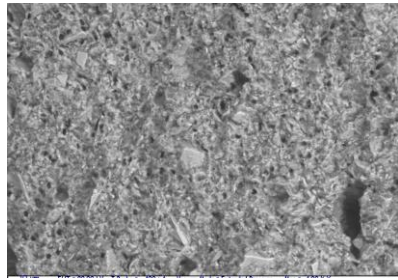
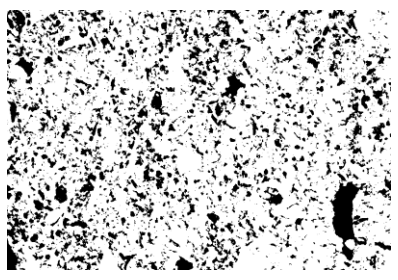
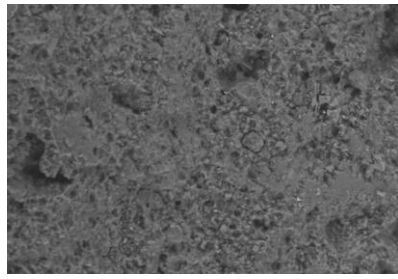
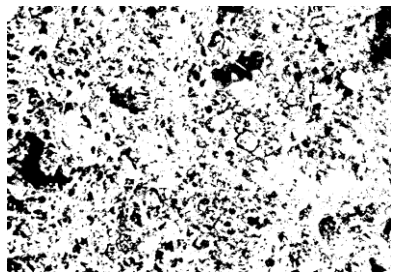
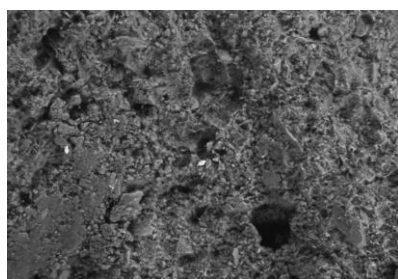
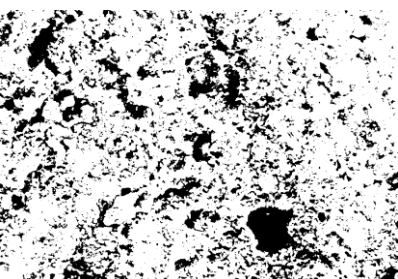
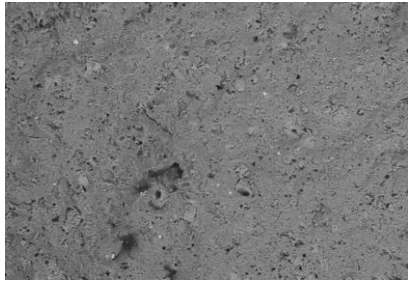
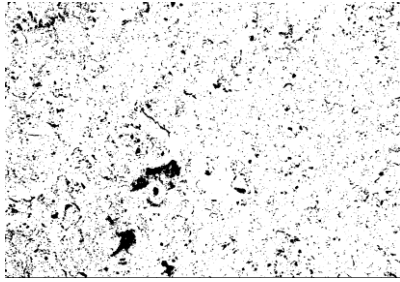
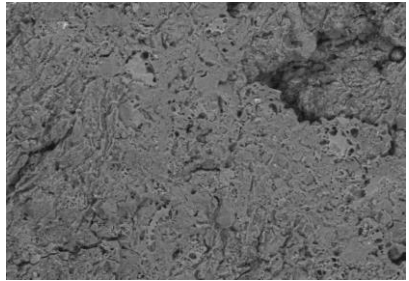
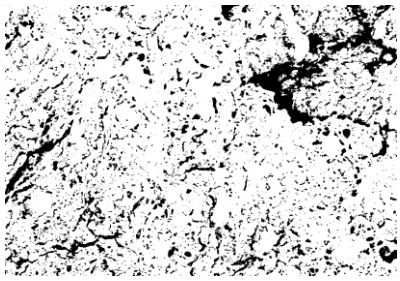
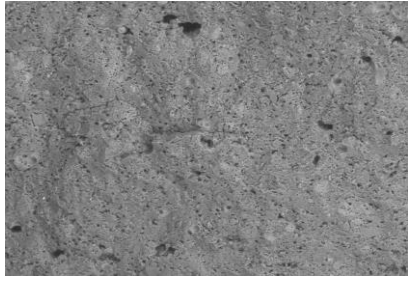
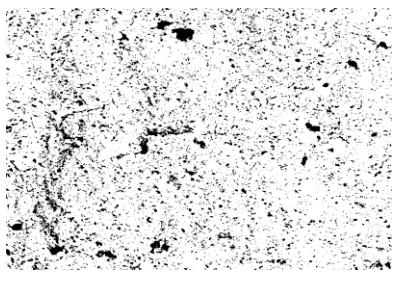
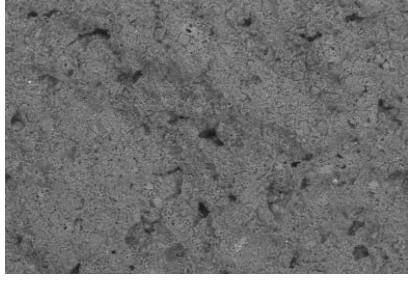
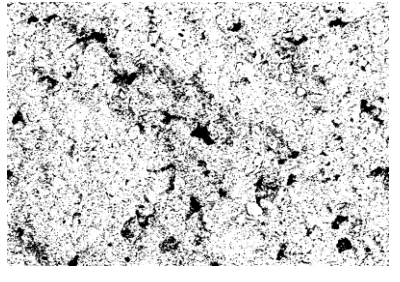
Sample	Original image	Processed image	Average pore size (μm^2)
HB-GEO			10.79
HB-GSP5			13.26
HB-GTT5			17.69
HB-GLI5			18.79

Table 3.3.8. ImageJ analyses of annealed samples with HB formulation

Sample	Original image	Processed image	Average pore size (μm^2)
HB-GEO			8.15
HB-GSP5			7.04
HB-GTT5			7.28
HB-GL15			7.24

Porosity can be interpreted as the reason for the loss of mechanical properties due to biomass. Compressive strength is plotted against pore size in Figure 3.3.33. The decrease of mechanical properties with respect to pore size is clear and it follows with good approximation ($R^2=0.964$) a power-law trend, according to the equation

$$\sigma = 265.9 \cdot A_{av}^{-1.14} \quad (7)$$

in which σ is the compressive strength (in MPa) and A_{av} is the average pore area (in μm^2).

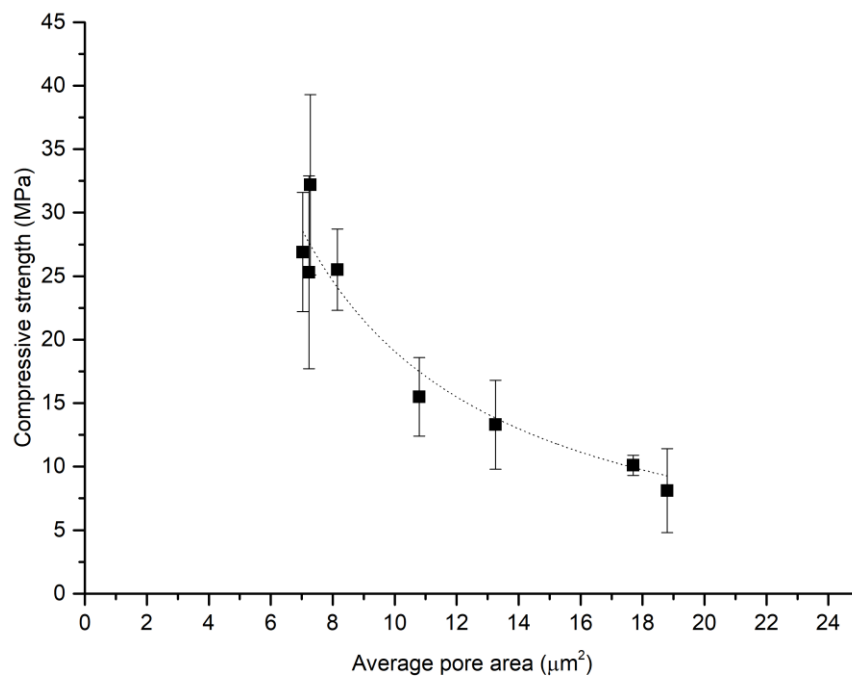


Figure 3.3.33. Compressive strength against average pore area (HB formulations)

3.3.2. Low-bentonite formulation

3.3.2.1. Rheological behaviour of the pastes

Flow curves of the geopolymer pastes filled with 1, 3 and 5 php (with respect to the powders) of Spirulina and Tetraselmis are reported in Figure 3.3.34 and Figure 3.3.35, respectively.

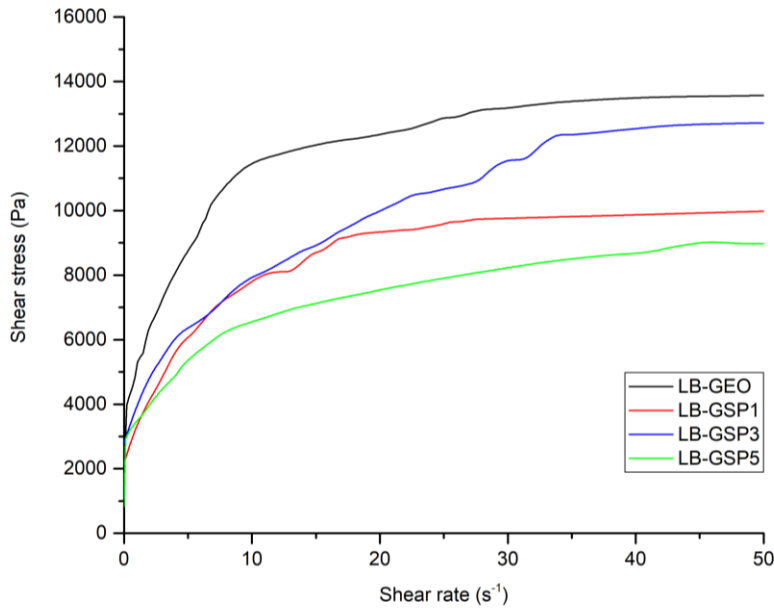


Figure 3.3.34. Flow curves of low-bentonite printable pastes, containing Spirulina

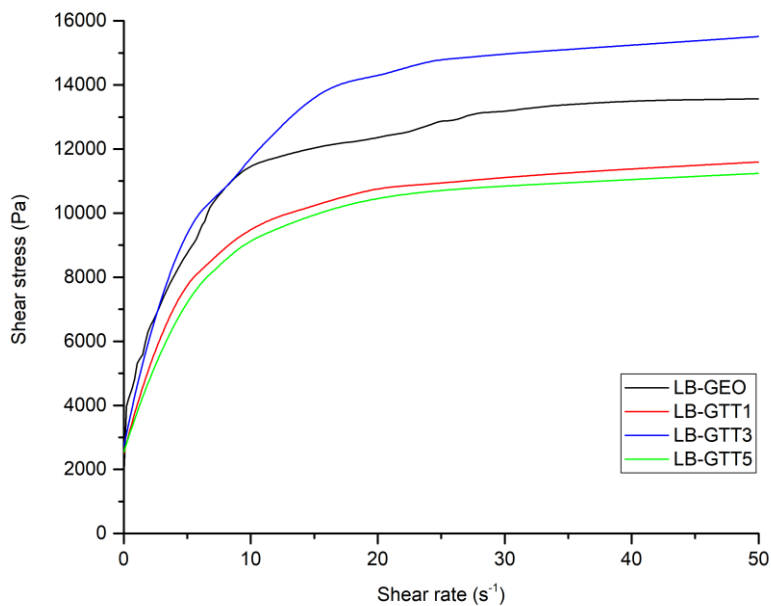


Figure 3.3.35. Flow curves of low-bentonite printable pastes, containing Tetraselmis

The shape of the flow curves is similar, but the curve of unfilled geopolymer (LB-GEO) is higher than the other ones, except LB-GTT3. This result means that unfilled geopolymer has higher apparent viscosity than almost all the pastes containing biomass in the whole shear rate range considered.

The curves were fitted according to Herschel-Bulkley's model (Equation (1)). The resulting parameters are reported in Table 3.3.9.

Table 3.3.9. Parameters of Herschel-Bulkley's model for LB formulations, containing biomass

Sample	Biomass php (powder)	Yield stress (Pa)	K (Pa s ⁿ)	n	R ²
LB-GEO	0	2864 ± 241	244 ± 212	0.53 ± 0.03	0.984
LB-GSP1	1	1715 ± 93	2750 ± 91	0.31 ± 0.01	0.988
LB-GSP3	3	1027 ± 17	3091 ± 21	0.35 ± 0.00	0.989
LB-GSP5	5	1545 ± 135	1894 ± 135	0.43 ± 0.02	0.980
LB-GTT1	1	2035 ± 114	2078 ± 113	0.61 ± 0.02	0.988
LB-GTT3	3	1311 ± 214	3723 ± 196	0.45 ± 0.01	0.991
LB-GTT5	5	1906 ± 135	2054 ± 124	0.57 ± 0.02	0.991

As already observed for high-bentonite formulation, also in the case of low-bentonite formulation the fitting with Herschel-Bulkley's model is good, meaning that the pastes behave as pseudoplastic fluids with a yield stress. The reduction of yield stress for the specimens with biomass addition is observed, as well. Differently to HB formulations, in LB ones the W/S ratio is constant. Therefore, this phenomenon can be directly related to the action of microalgae, not to the higher amount of water. Both for *Spirulina* and *Tetraselmis*, the reduction in yield stress shows a trend with a minimum at 3 php (Figure 3.3.36).

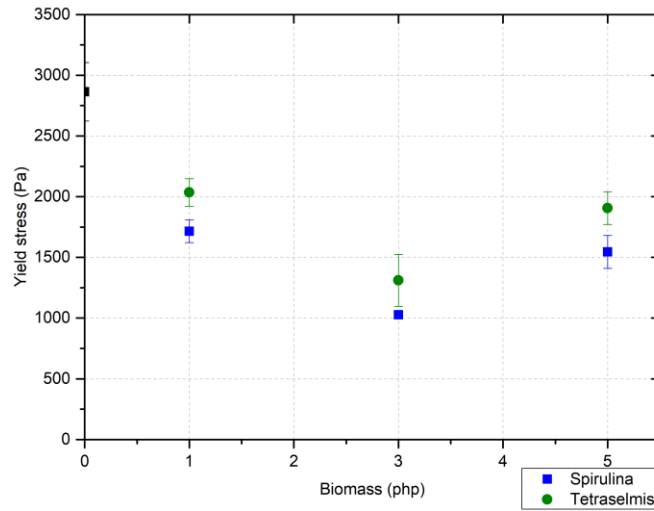


Figure 3.3.36. Yield stress against biomass amount added to geopolymer pastes with LB formulation

Dynamic tests in stress sweep are performed on the same formulations to assess the limit of linear behaviour and to look for a crossover point between the storage modulus (G') and the loss modulus (G''). From the crossover point, an estimation of the yield stress can be found, according to the following relation [98]:

$$\tau_y = (G'^2 + G''^2)^{0.5} \gamma_{crossover} \quad (8)$$

in which τ_y is the yield stress, G' is the storage modulus, G'' is the loss modulus, and $\gamma_{crossover}$ is the strain, evaluated at the crossover point.

Results of dynamic rheological analyses are reported in Figure 3.3.37. The trends that can be observed are similar for all the formulations tested; in the linear region G' is in the order of 10^6 Pa and G'' in the order of 10^5 Pa.

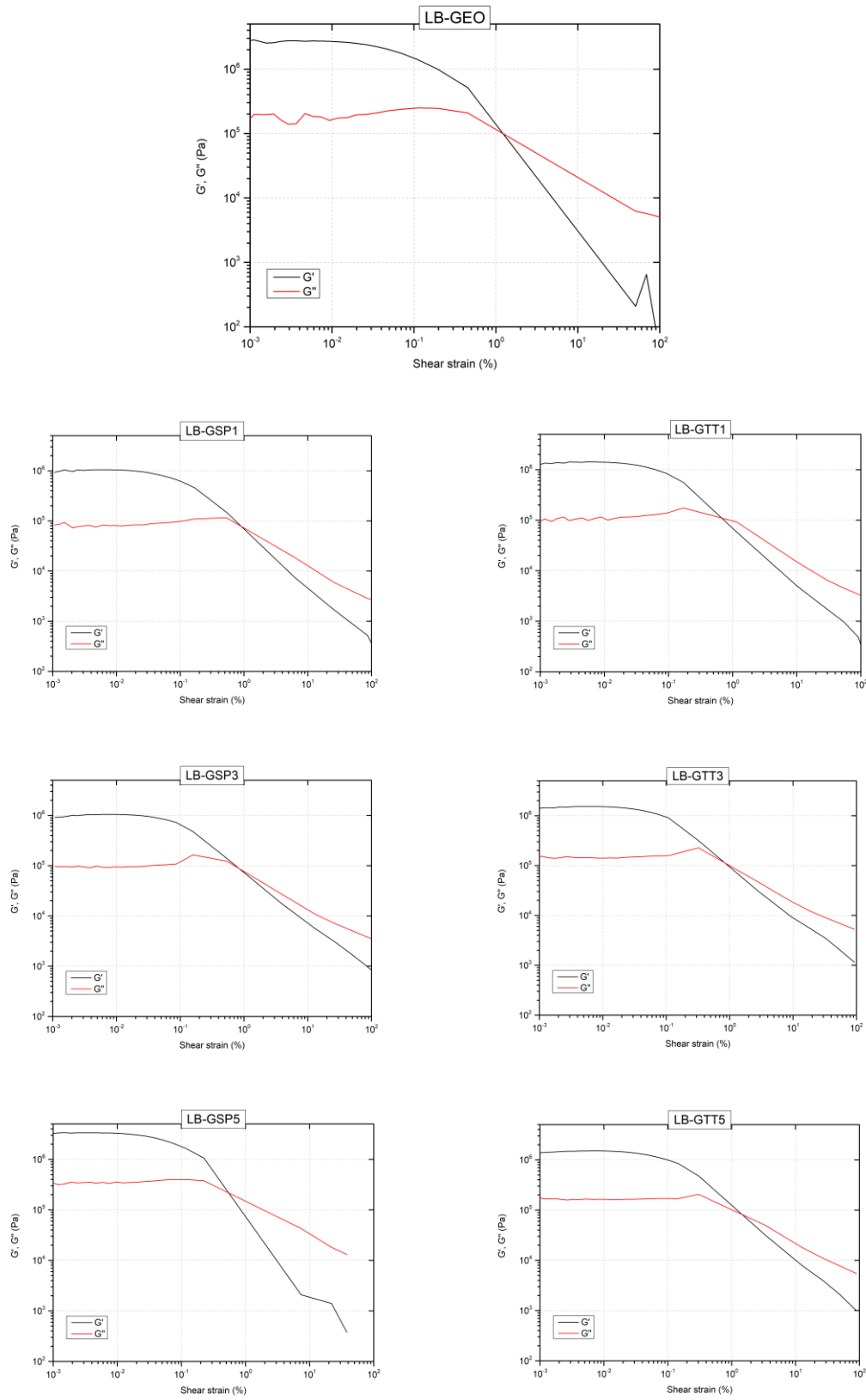


Figure 3.3.37. Plots resulting from dynamic rheological analyses performed in stress sweep, at constant frequency. The linear region and the crossover point are always visible.

According to Equation (8), the yield stress is estimated for all the formulations (Table 3.3.10). Although the values are different with respect to the ones found by fitting the flow curves, the reduction of yield stress with biomass addition, showing a minimum at concentration of 3 php, is confirmed also with this analysis.

Table 3.3.10. Cross-over points and estimation of yield stress compared to yield stress found from flow curves

Sample	Biomass php (powder)	Crossover		Estimated yield stress from dynamic tests (Pa)	Yield stress from flow curves (Pa)
		Shear strain (%)	$G' = G''$ (Pa)		
LB-GEO	0	1.22	100042	1721	2864
LB-GSP1	1	0.90	78043	997	1715
LB-GSP3	3	0.84	87848	1040	1027
LB-GSP5	5	0.55	216074	1670	1545
LB-GTT1	1	0.68	110012	1052	2035
LB-GTT3	3	0.84	113639	1346	1311
LB-GTT5	5	1.46	81706	1687	1906

One of the most important features of an ideal paste for LDM 3D printing is the ability to retain the shape after each filament is deposited. From the rheological point of view, this corresponds to a quick recovery of deformation when no shear stress is applied [99]. To assess this property, creep and recovery tests were performed on some printable and non-printable pastes. Figure 3.3.38 reports the creep and recovery curves of formulations containing Spirulina, from 1 to 5 php, while a comparison between printable and non-printable formulations is shown in Figure 3.3.39.

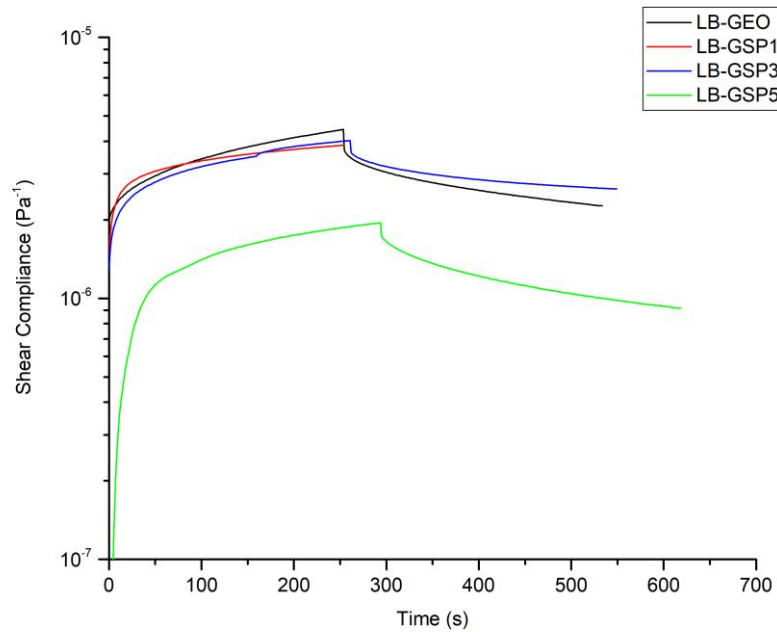


Figure 3.3.38. Creep and recovery curves of geopolymers containing Spirulina

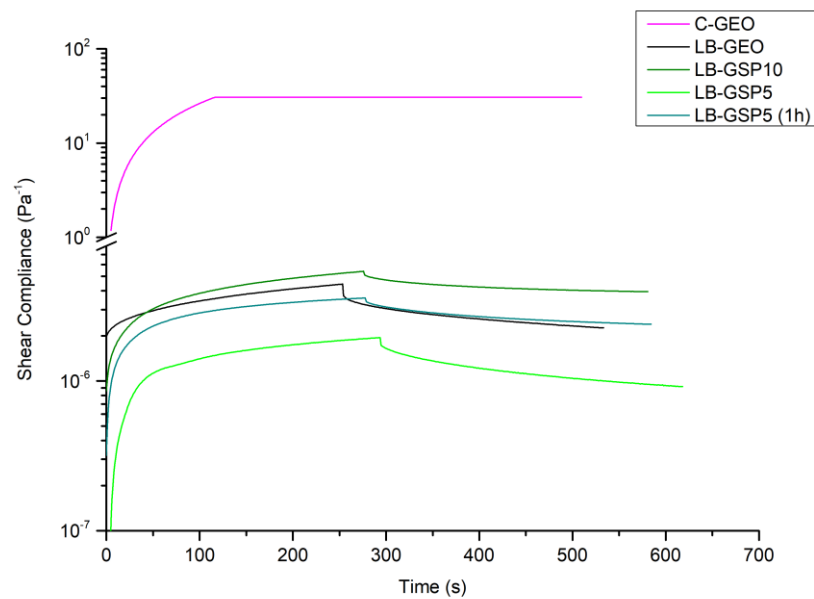


Figure 3.3.39. Comparison between printable and non-printable pastes

Curves belonging to samples containing 1 and 3 php of biomass are very similar to the one of unfilled geopolymer. LB-GSP5 presents a lower shear compliance, i.e. higher stiffness, but a similar amount of recovery. On the other hand, the curve of unfilled metakaolin and activator shows no recovery and higher values of shear compliance (in the order of 10 Pa^{-1} , compared to 10^{-6} Pa^{-1} of the other pastes). Small instantaneous

recovery is shown also by curves of the sample containing 10 php of biomass (LB-GSP10) and of LB-GSP5 tested 1 hour after the mixing of the components. The quantification of the amount of recovery is done according to the procedure explained in § 2.5.2 (Equations (5a), (5b) and (5c)). Results are reported in Table 3.3.11.

Table 3.3.11. Instantaneous, retarded and total recovery of pastes containing microalgal biomass (*Spirulina*)

Sample	J_{\max} (Pa ⁻¹)	X_i (%)	X_r (%)	X_{tot} (%)	Printable
C-GEO	3.07E+01	0	0	0	No
LB-GEO	2.26E-06	10	53	63	Yes
LB-GSP1	3.87E-06	8	28	36	Yes
LB-GSP3	4.02E-06	10	25	35	Yes
LB-GSP5	1.95E-06	11	42	53	Yes
LB-GSP5 (1h)	3.59E-06	5	28	33	No
LB-GSP10	5.40E-06	5	22	27	No

The results confirm that printability is related to the instantaneous recovery of deformation, according to literature. Three different cases are identified:

- no recovery, neither instantaneous nor retarded. This behaviour is shown by C-GEO, the slurry made only of metakaolin and activator, which is a low viscosity fluid without yield stress. This kind of pastes can be extruded, but they are not able to keep a defined shape and sustain a structure when printed;
- printable pastes all show an instantaneous recovery around 10% (the lowest value is the one of LB-GSP1, 8%), which are the higher values measured in all tests performed;
- lower instantaneous recovery (5%) is shown by the formulation with higher amount of biomass (LB-GSP10) and by the paste containing 5 php of *Spirulina* tested 1 hour after the mixing. These mixtures are less cohesive because water is absorbed by the high amount of biomass (in the former case) or has already evaporated and/or taken part in the hardening process (in the latter case). As a result, during the printing process the extruded filament, being less capable to recover the deformation due to extrusion, breaks, creating a discontinuous layer. This phenomenon is known in literature as “tearing” [100], [101].

Retarded recovery is meaningless as far as printability is concerned.

3.3.2.2. Compression tests on hardened specimens

Compression tests were performed on 3D printed hardened specimens (hollow cylinders), containing Spirulina and Tetraselmis, after 7 or 28 days, with or without annealing. Table 3.3.12 reports the results in terms of compressive strength. These results are also plotted in column diagrams and compared to the one obtained for high-bentonite formulation.

Table 3.3.12. Compressive strength values of 3D printed hardened specimens with LB formulation, containing Spirulina (from 1 to 5 php) and Tetraselmis (5 php)

Sample	Biomass php (powders)	Compressive strength (MPa)			
		7 days	28 days	7 days (annealed)	28 days (annealed)
LB-GEO	0	22.4 ± 3.6	26.7 ± 3.5	30.2 ± 5.9	28.0 ± 4.8
LB-GSP1	1	20.5 ± 5.4	-	31.1 ± 4.5	-
LB-GSP3	3	23.1 ± 5.3	-	36.8 ± 7.6	-
LB-GSP5	5	17.8 ± 2.7	26.3 ± 6.0	28.4 ± 2.9	37.6 ± 5.8
LB-GTT5	5	16.5 ± 3.0	-	30.3 ± 8.7	-

Even for low-bentonite formulation, looking at results at 7 days (Figure 3.3.40), biomass does not seem to affect significantly the compressive strength: a slight decrease in the average value can be observed for formulations at 1 and 5 php, which is negligible if the standard deviation is taken into account. The same consideration holds for samples tested after 28 days of ambient curing (Figure 3.3.41).

The effect of curing time is more pronounced for LB than for HB formulation. For instance, the compressive strength of the HB unfilled sample grows from 14.7 ± 3.1 MPa at 7 days to 15.5 ± 3.1 MPa at 28 days, while the same sample with LB formulation from 22.4 ± 3.6 MPa to 26.7 ± 3.5 MPa. This result suggests that the mechanical properties plateau is not completely achieved after 7 days for low bentonite formulation. Anyway, all the LB non-annealed samples tested displayed higher values of compressive strength if compared to HB ones. This result is in accordance with the discussion made in § 3.2.

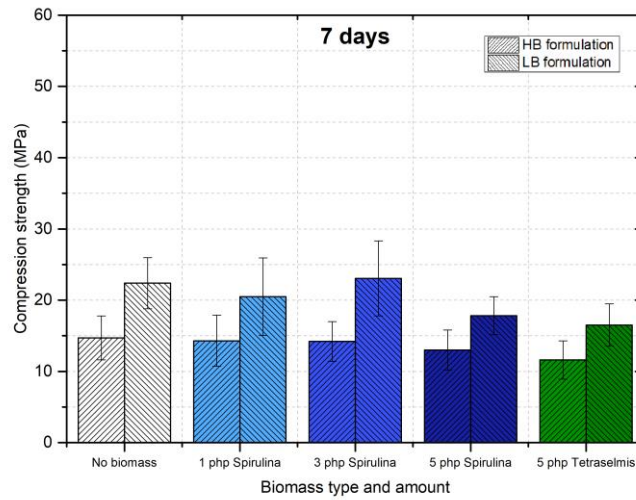


Figure 3.3.40. Compressive strength of geopolymers (low-bentonite formulation, containing biomass), tested on 3D printed hollow cylinders after 7 days of ambient curing

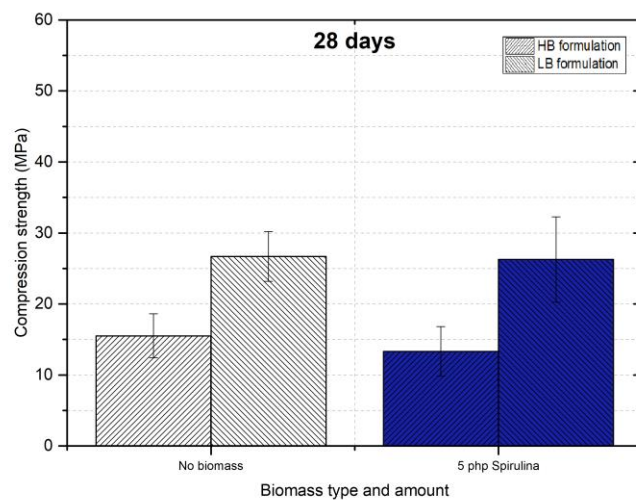


Figure 3.3.41. Compressive strength of geopolymers (low-bentonite formulation, containing biomass), tested on 3D printed hollow cylinders after 28 days of ambient curing

As already observed for high-bentonite formulation, annealing always improves mechanical properties, but the standard deviation of the data is increased, as well, meaning that the behaviour of annealed specimens is less reproducible with respect to that of non-annealed ones. At 7 days (Figure 3.3.42), annealing is more effective on samples having HB formulation, leading to higher compressive strength both for unfilled and filled formulations. Regarding the effect of biomass, also for low-bentonite formulation it is not significant.

Low-bentonite samples annealed after 28 days of ambient curing (Figure 3.3.43). show higher compressive strength values than the high-bentonite ones, in accordance with the results obtained for non-annealed geopolymer. In general, considering only LB formulation, both at 7 and at 28 days, annealing leads to improvements of mechanical properties, higher for samples filled with biomass than for the unfilled one. However, only in the case of LB-GSP5 annealed at 28 days the compressive strength is actually higher with respect to the unfilled samples (37.6 ± 5.8 MPa versus 28.0 ± 4.8 MPa).

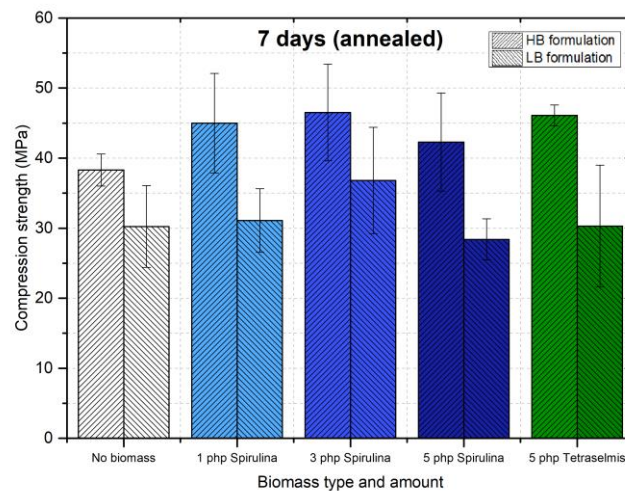


Figure 3.3.42. Compressive strength of geopolymers (low-bentonite formulation, containing biomass), tested on 3D printed hollow cylinders after 7 days of ambient curing and 4 hours of annealing at 800°C

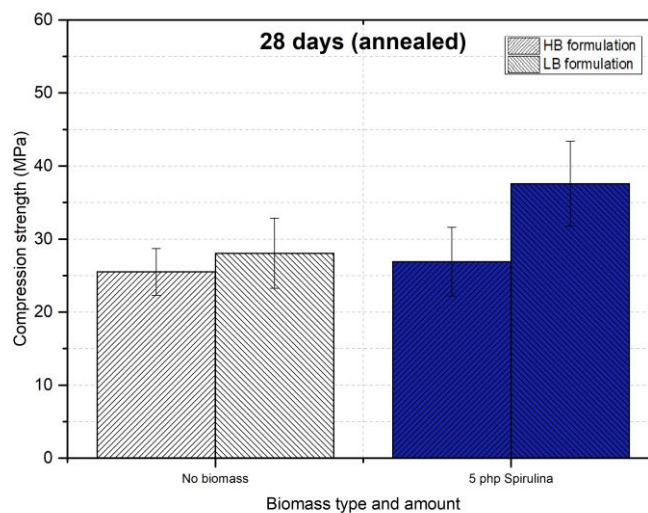


Figure 3.3.43. Compressive strength of geopolymers (low-bentonite formulation, containing biomass), tested on 3D printed hollow cylinders after 28 days of ambient curing and 4 hours of annealing at 800°C

Summarizing, if thermal treatment is not performed, higher values of compressive strength are obtained with low-bentonite formulation, which are all comprised in the interval of normal strength concrete applications (16 MPa – 45 MPa) defined by the standard UNI-EN 206-2013 [97]. On the contrary, annealing (at 7 days) leads to better results on high-bentonite formulation, even higher than 45 MPa.

In addition to the results discussed before, a comparison with casted samples has been carried out also for LB formulation (Table 3.3.13).

Table 3.3.13. Compressive strength of geopolymers (LB, containing biomass) tested on different kinds of samples at 28 days

Sample	Biomass php (powder)	Compressive strength at 28 days (MPa)			Compressive strength at 28 days (annealed samples) (MPa)		
		3D printed	Casted cube	Casted cylinder	3D printed	Casted cube	Casted cylinder
LB-GEO	0	26.7 ± 3.5	23.5 ± 3.6	19.4 ± 4.2	28.0 ± 4.8	31.6 ± 4.5	19.7 ± 5.5
LB-GSP5	5	26.3 ± 6.0	15.9 ± 2.6	18.2 ± 5.0	37.6 ± 5.8	19.2 ± 5.0 †	20.8 ± 4.4 †

† Samples cracked during thermal treatment.

Regarding non-thermally treated samples, 3D printed hollow cylinders are more resistant than casted samples, in accordance with the results already discussed in § 3.3.1.3.

Considering annealed samples, a discussion for formulations containing biomass cannot be made in a reliable way, since both casted cubes and cylinders suffered cracking during thermal treatment, as described in § 3.3.1.3 for HB formulation containing microalgal biomass. So, just examining the unfilled samples (LB-GEO), similar values of compressive stress are attained for 3D printed hollow cylinders and casted cubes, while casted cylinders displayed lower strength. This different behaviour can be referred to a different homogeneity of the thermal treatment, depending on the geometry.

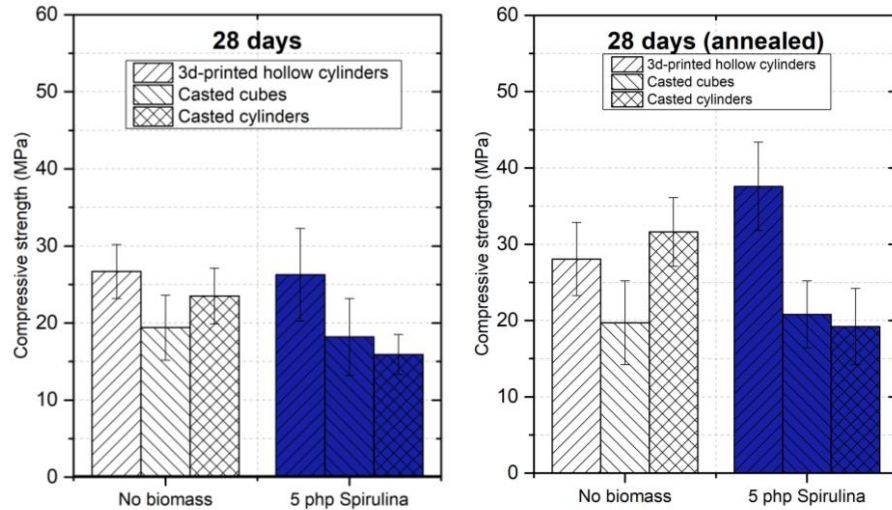


Figure 3.3.44. Comparison between compressive strength of formulations LB-GEO and LB-GSP5, measured at 28 days on samples thermally treated or not

From the discussion on results obtained with both formulations, as well as from SEM micrographs (see the comparison between C-GEO and LB-GEO in § 3.1), 3D printing process by itself does not seem to affect the mechanical properties and the microstructure. A further proof of this consideration is given by the comparison between mechanical properties obtained for casted samples (cubes and cylinders) and for samples 3D printed with the same shape and dimensions. This test was carried out only on one formulation (LB-GEO). Results are reported in Table 3.3.14.

Table 3.3.14. Comparison between casted and 3D printed samples, having the same geometry

Annealing	Compressive strength at 28 days (MPa)			
	3D printed cube	3D printed cylinder	Casted cube	Casted cylinder
No	29.8 ± 1.7	19.9 ± 4.3	23.5 ± 3.6	19.4 ± 4.2
Yes	45.2 ± 9.0	21 ± 1.6	31.6 ± 4.5	19.7 ± 5.5

Compressive strengths of printed and casted samples are comparable, demonstrating that 3D printing process does not affect mechanical properties, as far as the process itself is considered. The only value which is higher is that of 3D printed annealed cubes. However, standard deviation related to this value is higher, too.

Even if the process does not affect compressive strength, 3D printing affects mechanical properties because of the need of bentonite addition to obtain free-standing structures.

3.3.2.3. SEM and EDS analyses

SEM and EDS analyses were performed on samples LB-GEO and LB-GSP5, annealed and not.

LB-GEO (Figure 3.3.46) has a structure similar to its counterpart with high-bentonite formulation (HB-GEO). EDS analyses demonstrated again a matrix based on silicon and aluminium oxides, while the aggregates contain Ca.

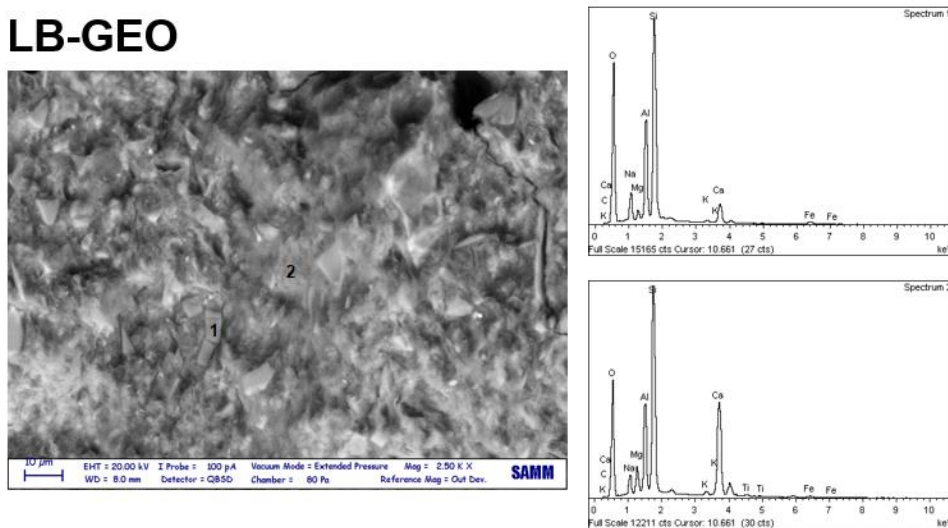


Figure 3.3.45. SEM micrograph and EDS spectra of sample LB-GEO

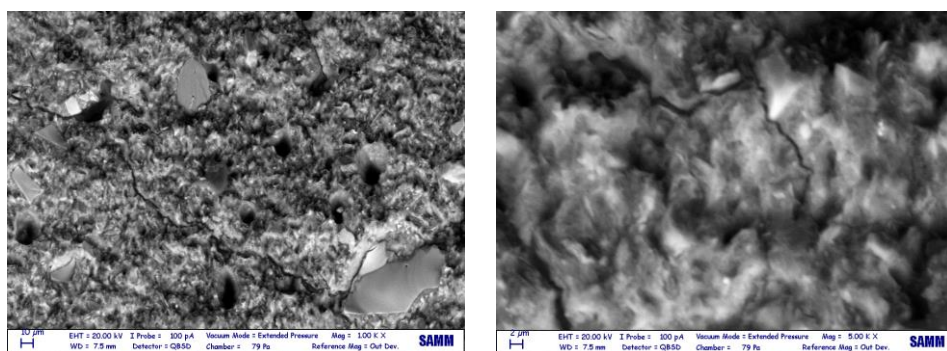


Figure 3.3.46. SEM micrographs at different magnifications (sample LB-GEO)

The addition of biomass does not affect the microstructure, which appears very similar to the unfilled sample (Figure 3.3.48). EDS analyses do not show peaks of C, meaning that biomass does not aggregate and it is well dispersed in the matrix. Looking

at the lower magnified micrograph (Figure 3.3.48, on the left), the structure seems more uniform than LB-GEO.

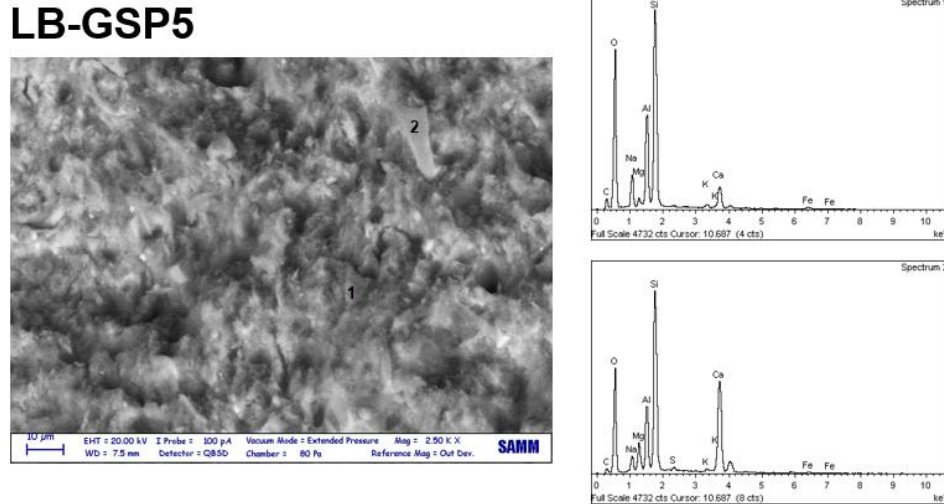


Figure 3.3.47. SEM micrograph and EDS spectra of sample LB-GSP5

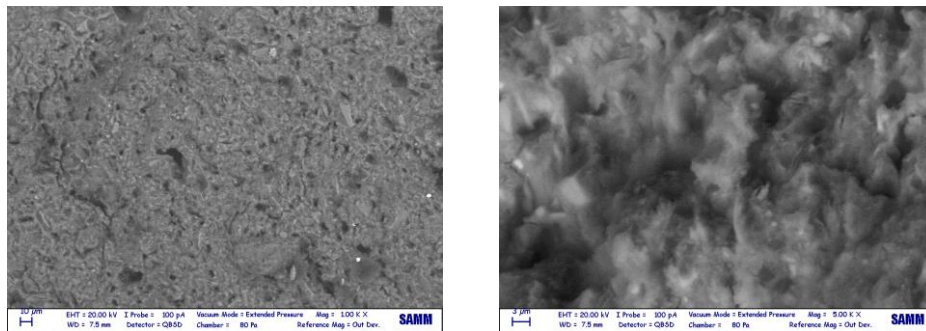


Figure 3.3.48. SEM micrographs at different magnifications (sample LB-GSP5)

Annealed samples appear more porous than the equivalent ones formulated with high bentonite (Figure 3.3.49 and Figure 3.3.50, compared to Figure 3.3.25 and Figure 3.3.27). The reason of this difference can be addressed to the filling effect of bentonite.

As previously observed, the matrix is more homogeneous and the pores exhibit a more rounded shape with respect to specimens not-thermally treated.

LB-GEO (annealed)

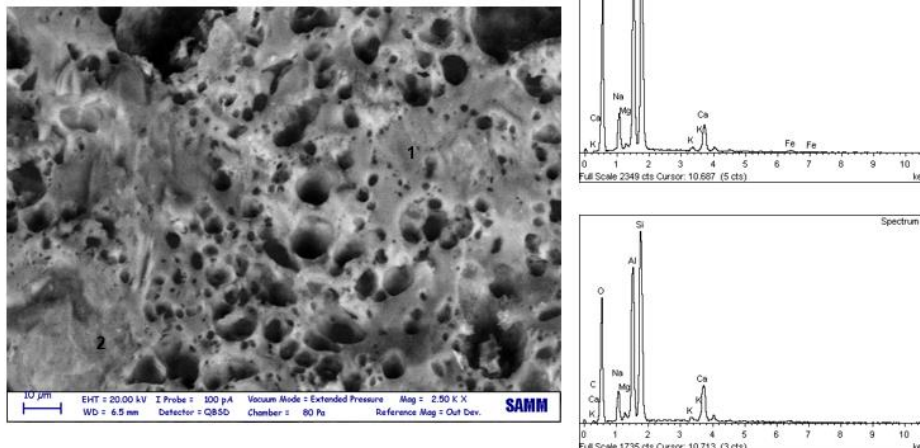


Figure 3.3.49. SEM micrograph and EDS spectra of sample LB-GEO (annealed)

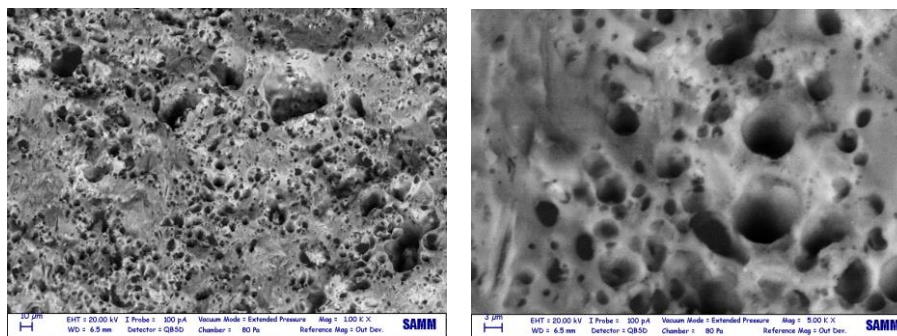


Figure 3.3.50. SEM micrographs at different magnifications (sample LB-GEO (annealed))

Adding 5 php of biomass, a microstructure with closer porosity is obtained after thermal treatment (Figure 3.3.51). Regions with different contrast, produced by secondary electrons, have basically the same composition, but slightly different amounts of Ca. Ca has been usually found as impurity in the majority of the specimens analysed by EDS.

LB-GSP5 (annealed)

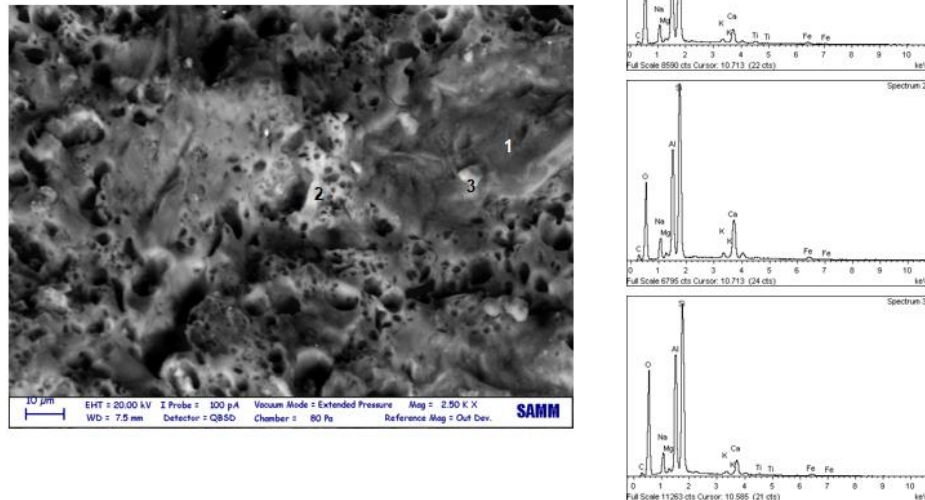


Figure 3.3.51. SEM micrograph and EDS spectra of sample LB-GSP5 (annealed)

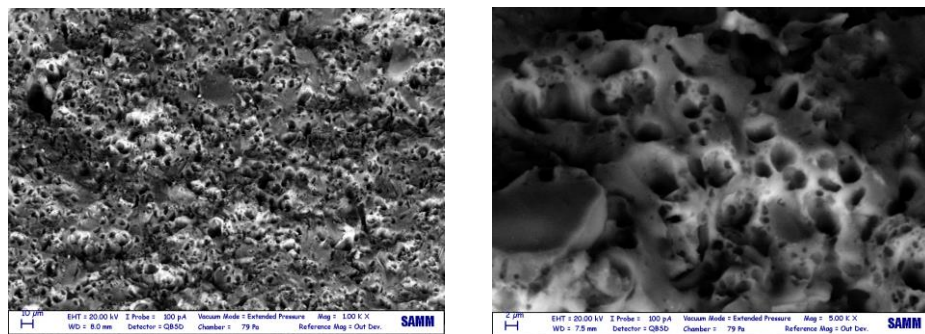
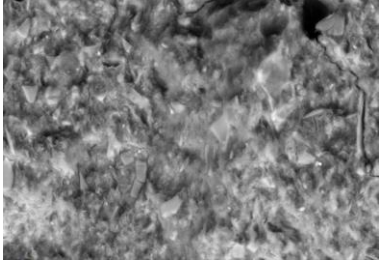

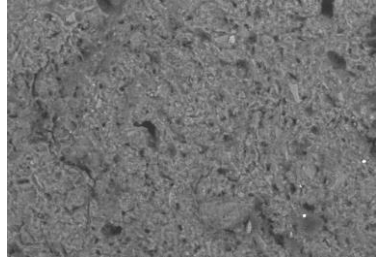
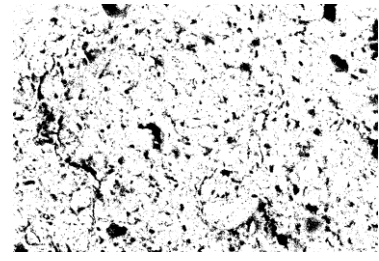
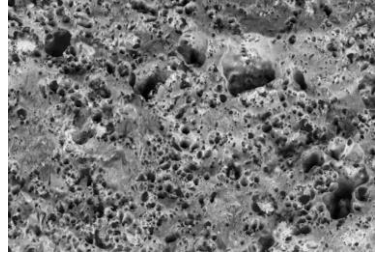
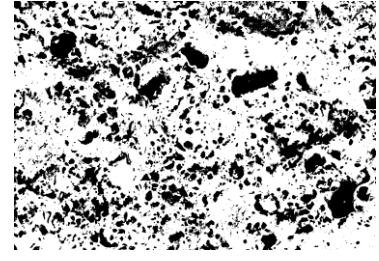
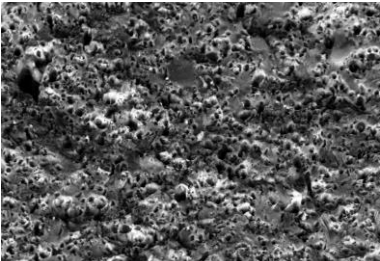
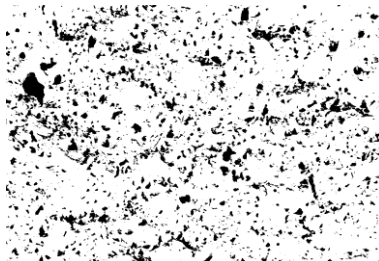


Figure 3.3.52. SEM micrographs at different magnifications (sample LB-GSP5(annealed))

The average pore area was evaluated by using the software ImageJ, following the procedure explained in § 2.2 and already applied for HB samples. Results are reported in Table 3.3.15. Despite the higher mechanical properties measured for LB samples, porosity values are comparable (in the case of non-annealed specimens) or higher (for annealed ones) with respect to HB. Therefore, the improvement in mechanical properties at 28 days achieved with LB formulation can be addressed to the higher resistance of metakaolin geopolymer matrix compared to bentonite, rather than to larger pore size.

Table 3.3.15. ImageJ analyses of LB samples

Sample	Original image	Processed image	Average pore size (μm^2)
LB-GEO			10.7
LB-GSP5			10.3
LB-GEO (annealed)			13.1
LB-GSP5 (annealed)			10.8

3.3.3. High concentration of biomass

Practical issues emerged when high quantity of biomass was added to geopolymer pastes containing bentonite (for 3D printing applications). Several tries to obtain a 3D printable mixture with additions of biomass higher than 5 php have been executed without succeeding (Figure 3.3.53).



Figure 3.3.53. Mixture obtained with an addition of 7 php of biomass to geopolymer paste containing bentonite. The paste appears discontinuous, even with the addition of supplementary water.

Because of this reason, the effect of high biomass content on geopolymer was investigated with cylindrical casted samples. High concentration, corresponding to Spirulina addition by 30 php with respect to metakaolin powder (equivalent to 13.6 wt% to the whole volume) was successfully attained. Water was added to the paste, to have a W/S ratio equal to C-GEO (0.38).

Mechanical properties were tested after 28 days of curing at ambient temperature. Annealing was performed on half of the specimens. Compressive strength values measured are compared with the unfilled sample C-GEO, tested in the same conditions (casted cylinders, 28 days). Results are reported in Table 3.3.16.

Table 3.3.16. Compressive strength of sample with high microalgal biomass concentration (30 php)

Sample	Biomass php (powder)	Compressive strength at 28 days (MPa)	
		Non-annealed	Annealed
C-GEO	0	40.1 ± 9.3	25.3 ± 6.5 †
C-GSP30	30	15.1 ± 3.0	25.4 ± 1.5

† Samples cracked during thermal treatment.

Considering non-annealed samples, the addition of high amount of biomass is detrimental as far as mechanical properties are considered. On the other hand, compressive strengths of annealed samples are comparable. As already discussed in § 3.2.2, C-GEO suffered cracking during annealing. The sample containing Spirulina at 30 php concentration did not suffered from cracking, achieving an increase of mechanical properties upon thermal treatment.

The reduction of mechanical properties of non-annealed samples can be related to the high amount and large size of pores introduced by microalgal biomass at these concentrations. SEM micrographs, reported in the following pictures, show that very high porosity is introduced both in annealed and non-annealed samples.

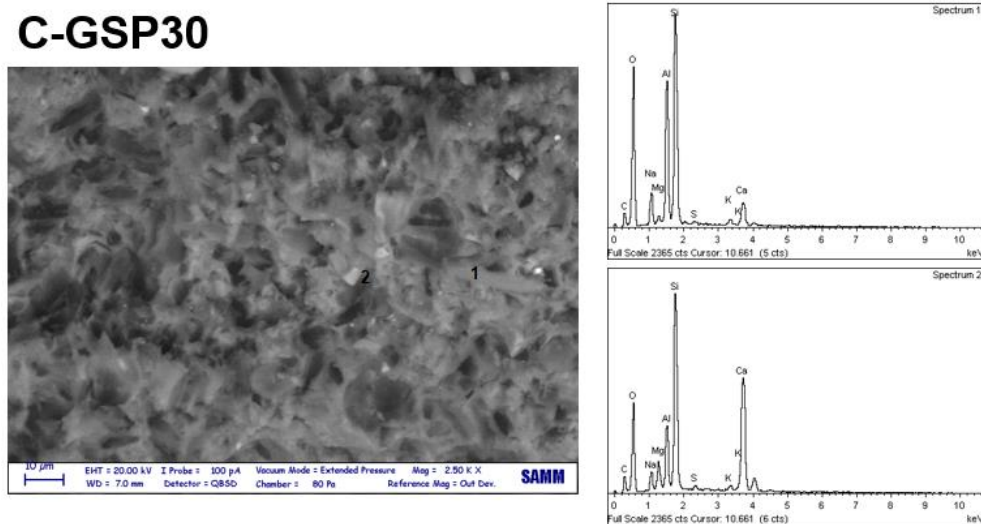


Figure 3.3.54. SEM micrograph and EDS spectra of sample C-GSP30

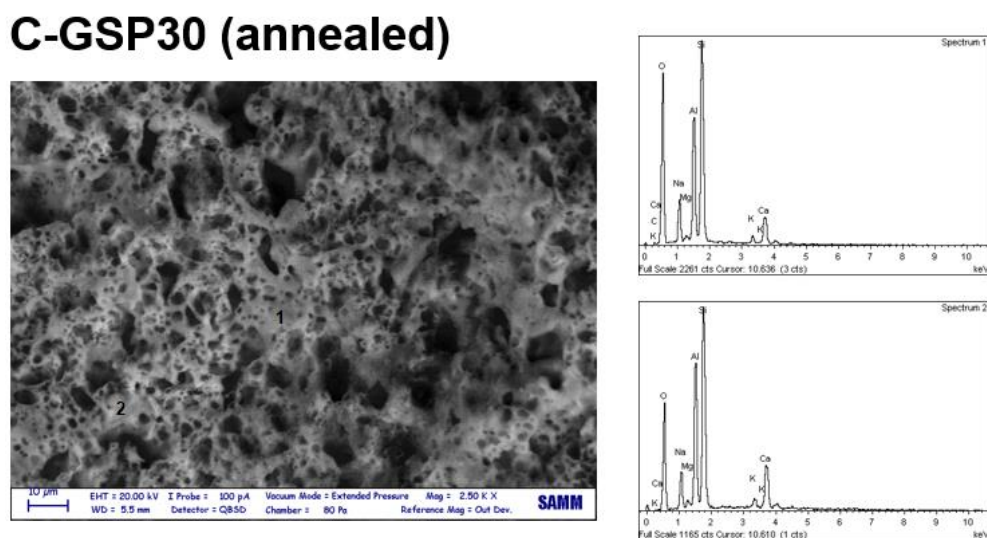


Figure 3.3.55. SEM micrograph and EDS spectra of sample C-GSP30 (annealed)

Average pore area, evaluated by ImageJ software, is $20.07 \mu\text{m}^2$ for the non-annealed sample and $14.13 \mu\text{m}^2$ for the annealed one. So, as already observed for other formulations containing biomass, annealing reduces porosity, improving the mechanical properties. Porosity of these samples is higher, compared both to C-GEO and to the other formulations for 3D printing.

EDS spectra (Figure 3.3.54 and Figure 3.3.55) show low carbon content, despite the noticeable quantity of biomass. This result confirms that microalgal biomass is well mixed in the geopolymer matrix and no aggregates are formed because of it; the main effect of biomass is the introduction of pores.

The increased porosity is also evidenced by the reduction of density. Values of density, evaluated dividing measured values of mass and volume of at least six specimens, are reported in Table 3.3.17.

Table 3.3.17. Density of samples C-GEO and C-GSP30

Sample	Density of non-annealed samples (g/cm^3)	Density of annealed samples (g/cm^3)
C-GEO	1.73 ± 0.04	1.78 ± 0.07
C-GSP30	1.41 ± 0.06	1.44 ± 0.01

Moreover, from density data, it can be observed that thermal treatment does not affect density. During annealing, samples show mass reduction, due to complete drying, along with volume reduction. In most cases, presented in the previous paragraphs and for the sample containing high concentration of biomass, annealing lead to a rearrangement of the internal structure and of porosity interconnection, which improved mechanical properties. For sample C-GEO and for some casted samples containing bentonite and biomass, the structural rearrangement of annealing was not so efficient and cracking occurred.

3.4. Feasibility study on the use of recycled glass fibres as filler

In this chapter, the feasibility of the use of glass fibres as fillers (or reinforcing materials) in 3D printed metakaolin geopolymers is studied. Since the aim of the European project FiberEUse is the valorisation of recycled glass fibres, the first try in this preliminary study is to embed as much recycled material as possible.

Many formulations have been prepared both for casting and 3D printing. Results from rheological, mechanical and microstructural characterizations are reported in the following paragraphs.

3.4.1. Rheological behaviour of the pastes

Rheology of some formulations containing fibres was studied. Pastes with similar (the same if the usual weighing is considered, see § 2.2) amount of red recycled (for casting, C-GRR26, and for 3D printing, LB-GRR20) and virgin fibres were compared with the slurry made by metakaolin and activator (C-GEO) and with the unfilled geopolymer formulation for 3D printing (LB-GEO). Flow curves are reported in Figure 3.4.1a and viscosity curves of the formulations for casting in Figure 3.4.1b.

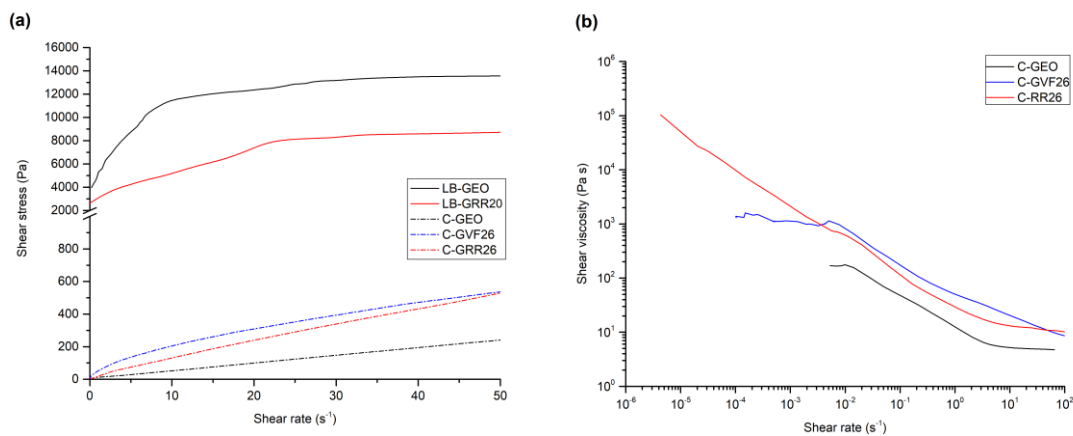


Figure 3.4.1. Flow curves (a) and viscosity curves (b) of pastes containing fibres

The addition of fibres increases the viscosity of the fluid, but it is not enough to have a yield stress, as can be observed from flow and viscosity curves of casted samples. Yield stress, which is necessary to obtain self-sustaining 3D printed structures, is present only in mixtures containing bentonite.

Flow curves of pastes showing yield stress (LB-GEO and LB-GRR26) are fitted according to Herschel-Bulkley's model (Equation (1)). The behaviour of the other formulations is modelled according to the power law model (Equation (2) and (3)) in the linear range of the double-logarithmic plot.

Table 3.4.1. Effect of fibre addition on the rheological properties (flow) of geopolymer pastes. Parameters of Herschel-Bulkley's model are reported

Sample	Yield stress (Pa)	K (Pa s ⁿ)	n	R ²
C-GEO	0 ± 0	13 ± 1	0.43 ± 0.00	0.999
C-RR26	0 ± 0	28 ± 1	0.36 ± 0.01	0.997
C-VF26	0 ± 0	62 ± 1	0.51 ± 0.01	0.983
LB-GEO	2864 ± 241	2444 ± 212	0.53 ± 0.02	0.984
LB-GRR20	2805 ± 27	345 ± 14	0.85 ± 0.01	0.996

Considering formulations for 3D printing, differently from biomass, red recycled added to the mixture does not affect the yield stress value, which remains around 2800 Pa. On the other hand, during flow, the behaviour is quite different: the flow index (n) is higher, meaning that the behaviour is more Newtonian-like (Newtonian behaviour corresponds to $n = 1$), while the consistency (K) is much lower. The effect is that, conversely to samples not containing bentonite, a paste with the same yield stress, but lower apparent viscosity is obtained, as can be observed in Figure 3.4.1a.

Dynamic tests at constant frequency (Figure 3.4.2) performed on formulations for casting showed no crossover, with a predominant viscous behaviour in all the shear stress range considered. Differences between virgin and recycled fibres are negligible.

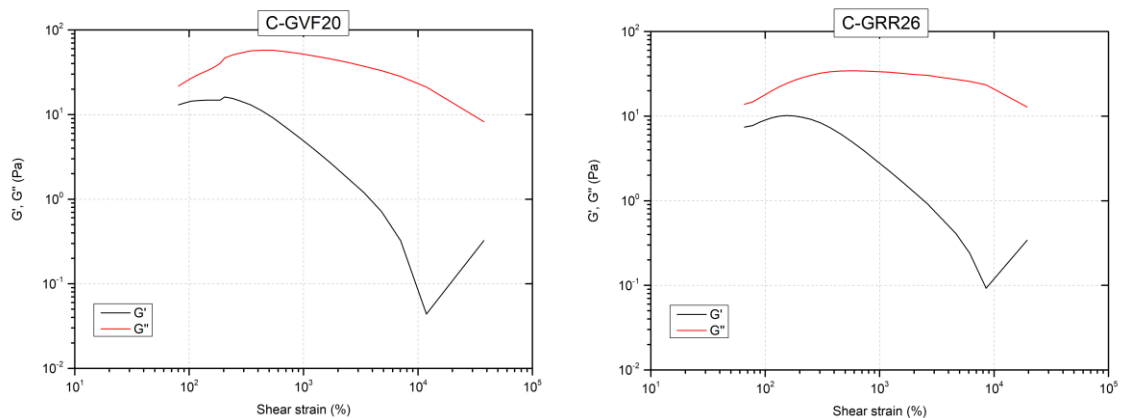


Figure 3.4.2. Dynamic moduli of specimens containing fibres

Creep and recovery tests were made on the same formulations considered for flow curves (Figure 3.4.3).

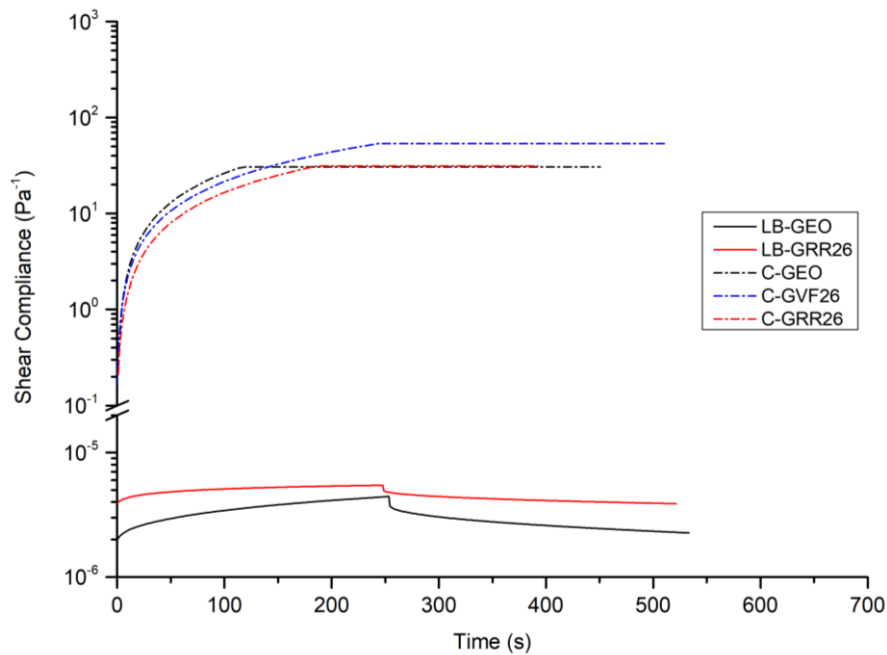


Figure 3.4.3. Creep and recovery of geopolymer pastes containing fibres

Formulations for casting present shear compliance values in the order of 10 Pa^{-1} ; and the addition of fibres does not have significant effects. All these samples do not show any recovery. On the contrary, the formulation for 3D printing (LB-GRR20) displays lower shear compliance (in the order of 10^{-6} Pa^{-1}), and deformation recovery (instantaneous and retarded), in accordance with the considerations made for creep and recovery tests on formulations containing biomass (§ 3.3.2.1). In particular, the instantaneous recovery of the sample containing recycled fibres is equal to the unfilled one and in the same range of the other printable formulations analysed in this work. Table 3.4.2 reports the different contributions to recovery, computed following Equations (5a), (5b) and (5c).

Table 3.4.2. Instantaneous, retarded and total recovery of pastes containing fibres

Sample	$J_{\max} (\text{Pa}^{-1})$	$X_i (\%)$	$X_r (\%)$	$X_{\text{tot}} (\%)$	Printable
C-GEO	3.07E+01	0	0	0	No
C-GVF26	5.36E+01	0	0	0	No
C-GRR26	3.13E+01	0	0	0	No
LB-GEO	2.26E-06	10	53	63	Yes
LB-GRR20	5.48E-06	10	19	29	Yes

3.4.2. Compression tests on hardened specimens

Compression tests are carried out on all formulations containing fibres, 3D printed and prepared by casting. The maximum amount of white recycled is lower than virgin fibres and red recycled, because problems in miscibility with geopolymer paste are evident at concentrations higher than around 10 php.

Mixtures for 3D printing are based on low-bentonite formulation and hollow cylinder specimens prepared are tested after 7 days of ambient curing. Compressive strength values are reported in Table 3.4.3.

Table 3.4.3. Compressive strength values of 3D printed hardened specimens containing recycled glass fibres, tested after 7 days of ambient curing

Sample	Fibre php (powder)	Compressive strength at 7 days (MPa)
LB-GEO	0	22.4 ± 3.6
LB-GRR5	5	25.8 ± 3.3
LB-GRR10	10	19.6 ± 1.1
LB-GRR20	20	23.4 ± 3.6
LB-GRR30	30	16.3 ± 1.3
LB-GWR5	5	19.5 ± 3.7
LB-GWR10	10	25.3 ± 5.5

The addition of fibres at these concentrations does not improve mechanical properties (Figure 3.4.4). The best results, which are obtained at 5 php for red recycled and at 10 php for white recycled, are just slight increase of compressive strength, negligible taking into account the error bars. On the other hand, red recycled at 30 php significantly lowers mechanical properties. This result suggests that the interaction between recycled fibres and the matrix is not good enough to promote a reinforcing effect. Anyway, up to 20 php of red recycled and 10 php of white recycled, recycled fibres can be effectively used as a filler for 3D printing pastes.

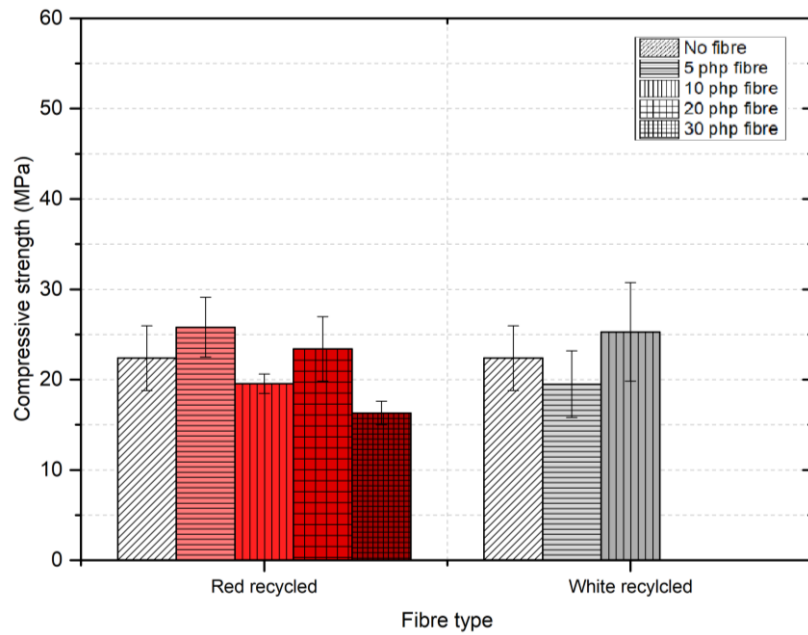


Figure 3.4.4. Compressive strength of geopolymers (low-bentonite formulation, containing recycled glass fibres), tested on 3D printed hollow cylinders after 7 days of ambient curing

Higher concentrations of recycled fibres and a comparison with virgin glass fibres are investigated with casted samples. Results of compression tests carried out on cylinder casted samples after 28 days of ambient curing are reported in Table 3.4.4 and plotted in Figure 3.4.5.

Table 3.4.4. Compressive strength values of cylindrical casted hardened specimens containing recycled glass fibres, tested after 28 days of ambient curing

Sample	Fibre php (powder)	Compressive strength at 28 days (MPa)
C-GEO	0	40.1 ± 9.3
C-GRR13	13	26.7 ± 2.4
C-GRR19	19	38.3 ± 4.3
C-GRR26	26	25.6 ± 7.6
C-GRR39	39	24.6 ± 5.4
C-GRR57	57	24.9 ± 3.9
C-GWR13	13	28.9 ± 6.8
C-GVF13	13	40.1 ± 9.4
C-GVF26	26	26.3 ± 5.6
C-GVF39	39	32.4 ± 9.8

Analysing the values obtained, the same considerations made for 3D printed samples hold: in general, the addition of fibres does not improve nor reduce the mechanical properties. Considering red recycled, which has been investigated in more

formulations, the best result is obtained for C-GRR19, whose compressive strength is comparable to the one of unfilled sample (C-GEO). Higher concentrations have the same effect of mechanical properties: from 26 to 57 php addition of recycled material, compressive strength is almost constant, around 25 MPa. White and red recycled have a similar effect, so the composition of the recycled seems not to have influence on the properties at the concentration considered.

Even the use of virgin fibres does not lead to a reinforcing effect. At 13 php, the mechanical properties are the same as the unfilled samples, while at higher concentrations compressive strength is reduced. The values obtained are similar to recycled glass fibres.

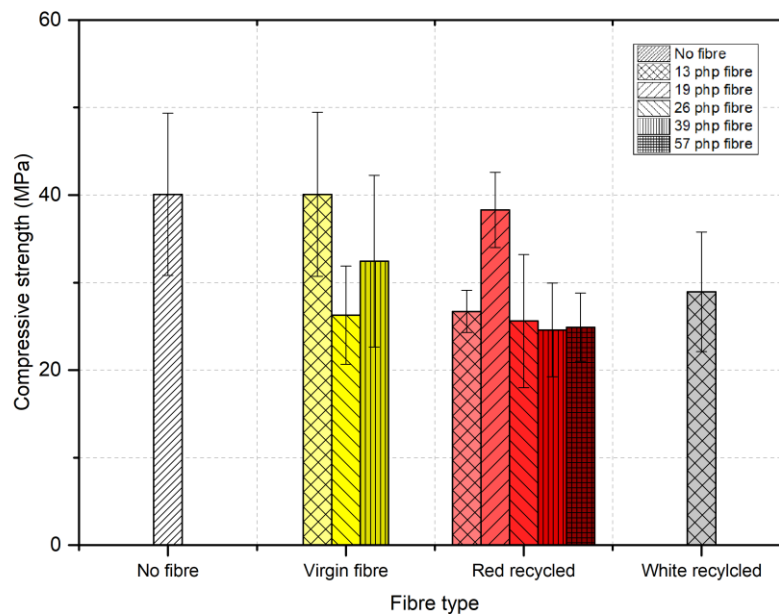


Figure 3.4.5. Compressive strength of geopolymers (low-bentonite formulation, containing recycled glass fibres), tested on casted cylinders after 28 days of ambient curing

3.4.3. SEM and EDS analyses

SEM and EDS analyses were performed on three samples containing fibres: C-GVF26, C-GRR26, C-GWR13 and LB-GRR5.

Glass fibres are clearly visible in the sample C-GVF26, which contains high quantity of virgin fibre. SEM micrographs, along with EDS spectra are reported in Figure 3.4.6.

C-GVF26

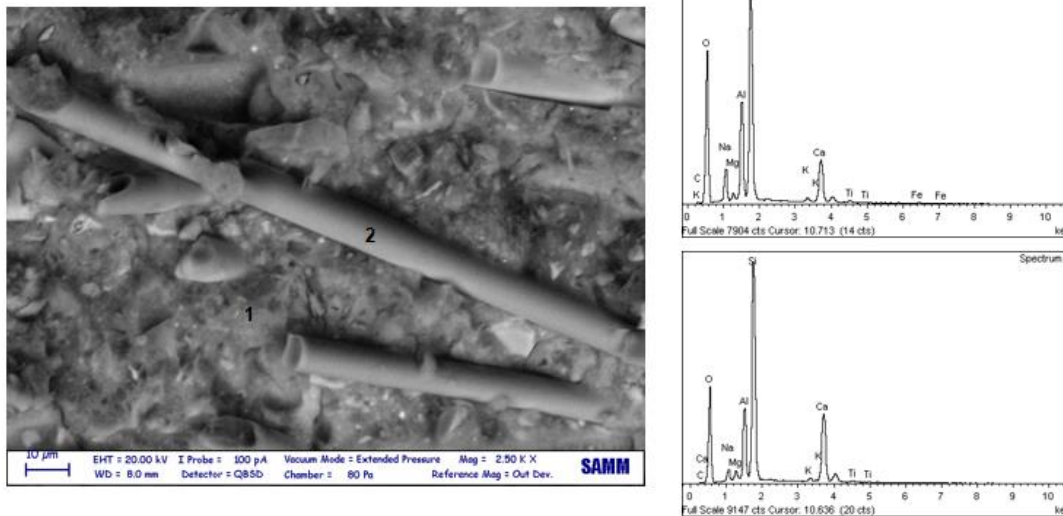


Figure 3.4.6. SEM micrograph and EDS spectra of sample C-GVF26

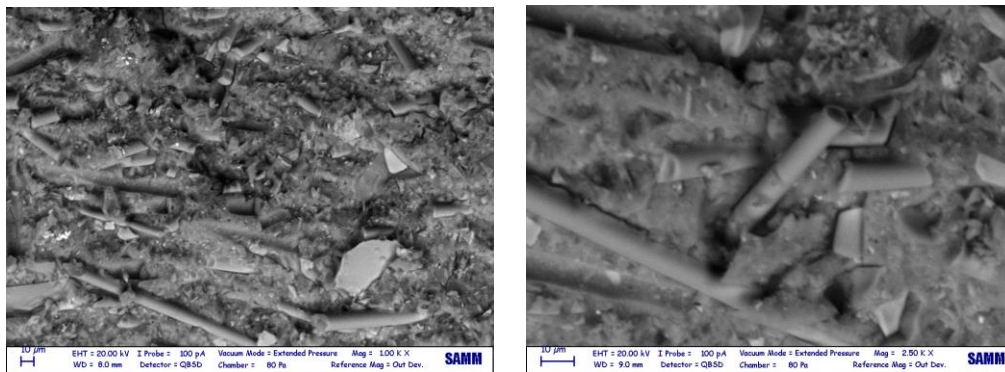


Figure 3.4.7. SEM micrographs of C-GVF26 at different magnifications

Because of the high content of silicon and aluminium oxides both in the matrix and in fibres, EDS spectra are very similar. Observing different magnification levels and spots (Figure 3.4.7), the distribution of fibres appears homogeneous: neither preferential orientations, nor clustering are visible.

Fibres are not visible in samples containing recycled glass fibres. Casted samples containing high concentration of additive display noticeable cracks, which are probably due to a poor interaction between recycled material and the geopolymer matrix (Figure 3.4.8, Figure 3.4.9 and Figure 3.4.10). The visible aggregates cannot be directly related to recycled glass fibres, since the usual composition based on Ca is found. No great differences can be appreciated between samples containing red and white recycled. Fe impurities are detected in very low concentrations by EDS (Spectrum 1 of sample C-GRR26).

C-GRR26

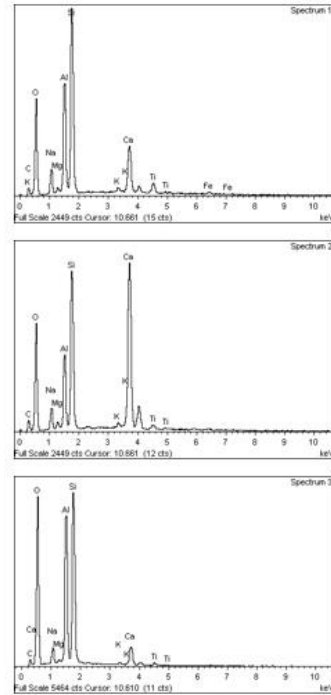
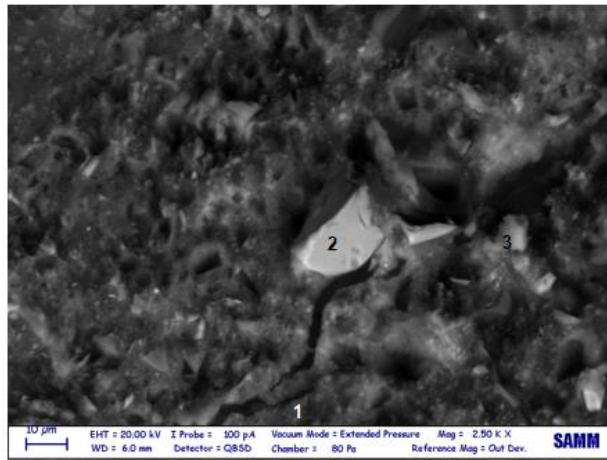


Figure 3.4.8. SEM micrograph and EDS spectra of sample C-GRR26; a large crack can be noticed near the aggregate

C-GWR13

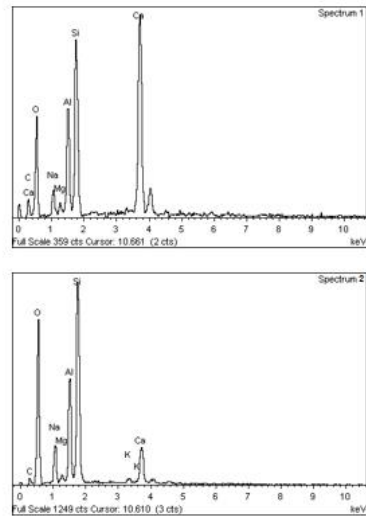
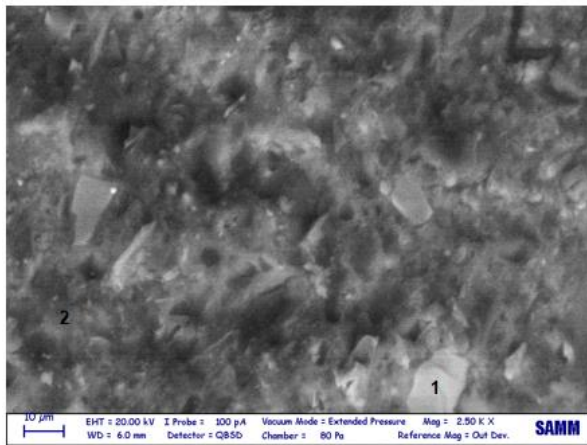


Figure 3.4.9. SEM micrograph and EDS spectra of sample C-GWR13

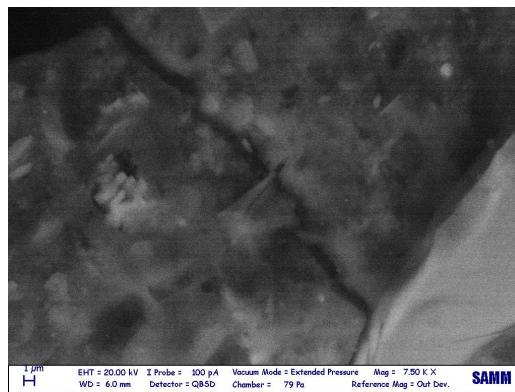


Figure 3.4.10. Magnification of sample C-GWR13, showing a crack

The formulation prepared for 3D printing, containing bentonite along with red recycled glass fibre additive, has a more uniform appearance at SEM (Figure 3.4.11), similar to other 3D printed samples. Despite the higher homogeneity, the poor interaction between recycled glass fibres and the matrix is demonstrated by the presence of cracks also in this sample at lower additive concentration (Figure 3.4.12). Therefore, the poor interaction between fibres and matrix can be addressed as the cause of the missed improvement in mechanical properties. Lowering even more the quantity of glass fibres, approaching values present in literature (no more than 5 wt%) may be the key to obtain the desired increase of compressive strength [87].

EDS spectra (Figure 3.4.11) does not show any relevant result for this sample.

LB-GRR5

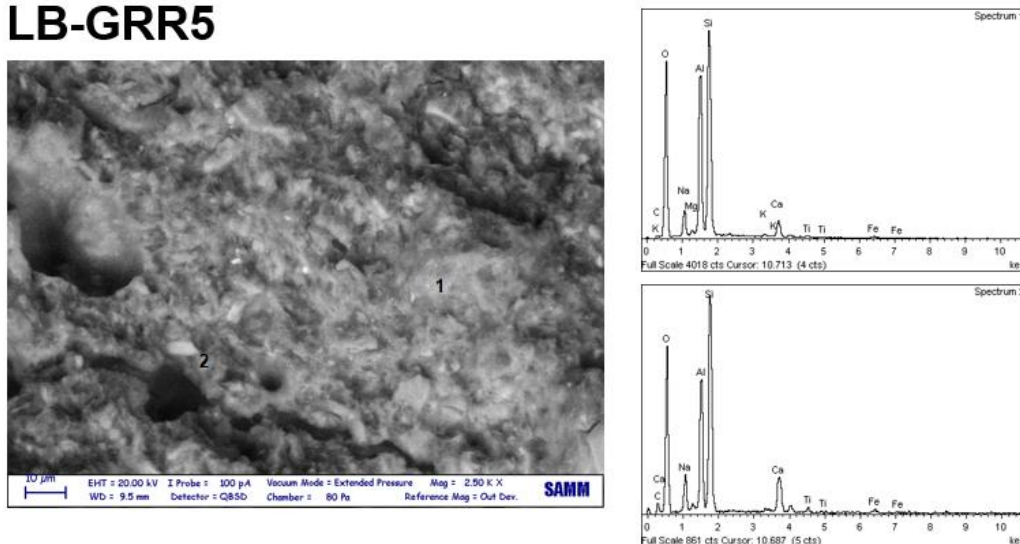


Figure 3.4.11. SEM micrograph and EDS spectra of sample LB-GRR5

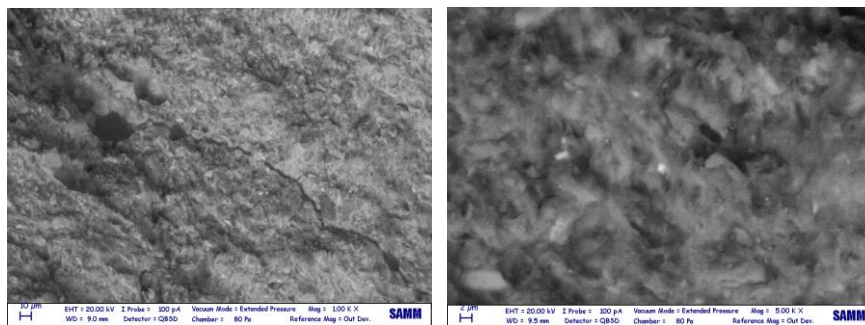


Figure 3.4.12. SEM micrographs of sample LB-GRR5 at different magnifications

3.5. Scale-up

The possibility to 3D print objects made by geopolymer in large scale is very interesting in view of the potential applications of this technology. A scale-up with a larger 3D printer has been tried.

The preparatory analyses on the formulation used and the results of the process are reported in the following paragraphs.

3.5.1. Materials for scale-up

The formulation chosen for the scale-up is based on low-bentonite approach, with the addition of 5 php of Spirulina; this formulation is selected since a large volume of biomass can be implied, with an acceptable reduction of mechanical properties. Bentonite B3 is used, because of its lower cost compared to B1 and B2. Referring to the studies reported in § 3.2.3, formulations containing B3 show lower yield stress than the ones with B1 or B2. Therefore, no water is added to the mixture, which is reported in Table 3.5.1.

Table 3.5.1. Composition of the formulation selected for the scale-up

Metakaolin (wt%)	Bentonite (wt%)	Activator (wt%)	Spirulina (wt%)
45.9	14.6	36.6	2.9

Rheology, mechanical properties and microstructure are studied for this formulation. Flow curves (Figure 3.5.1) are fitted with Herschel-Bulkley's model (Equation (1)); flow parameters are comparable to that of other formulations containing biomass, studied in the previous paragraph, using bentonite B1 in the mixture (Table 3.5.2).

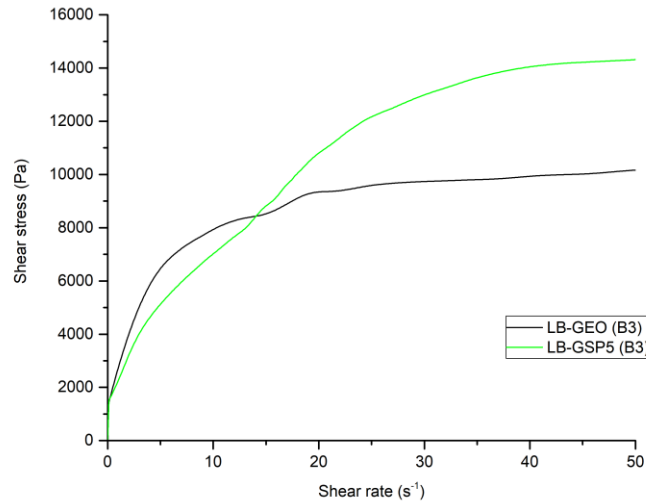


Figure 3.5.1. Flow curves of formulations containing bentonite B3

Table 3.5.2. Flow parameters of the formulation chosen for the scale-up printing, fitted according to Herschel-Bulkley's model

Yield stress (Pa)	K (Pa s ⁿ)	n	R ²
1446 ± 3	1843 ± 59	0.55 ± 0.01	0.998

A compressive strength of 31.5 ± 3.3 MPa is measured on 3D printed hollow cylinders, after 7 days of curing at ambient temperature. This value is higher than that measured on the unfilled sample (containing B3), 23.0 ± 4.7 MPa, and on the same formulation (containing B1), 17.8 ± 2.7 MPa. Probably, the combined action of biomass and bentonite B3, without the addition of water, has an optimal filling effect, which improves the mechanical resistance of the material.

The microstructure observed by SEM is comparable to that of the formulation LB-GSP5, containing B1 (Figure 3.5.2).

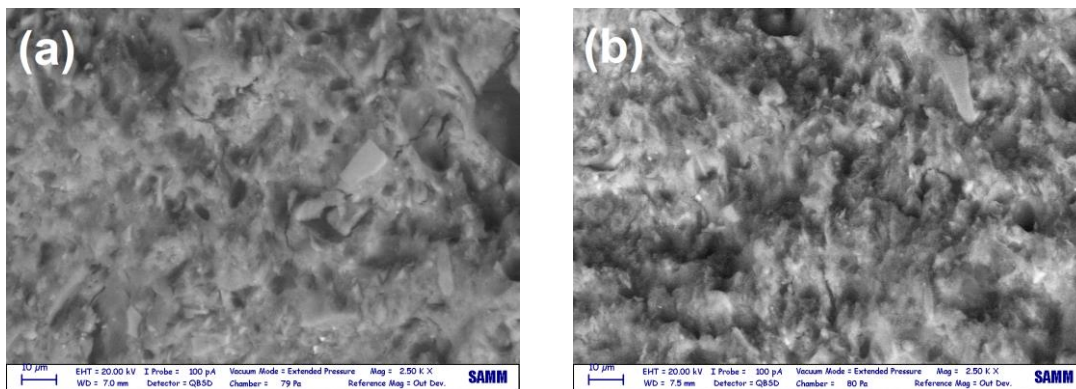


Figure 3.5.2. SEM micrograph of LB-GSP5 for scale-up, containing B3 (a) and formulated with B1 (b)

3.5.2. Scale-up process and results

Two main project constraints must be taken into account to tune process parameters and procedures. From one hand, the printing speed must be selected with respect to the ability of the material to sustain the weight of the layers subsequently deposited. An estimation of the maximum height that could be reached by a printed structure, considering the yield stress constant, is computed according to Equation (6). From the calculations made (reported in Appendix), the structure could grow around 24 cm before failure. This value is highly underestimated, since the studies made on the early age variation of properties (reported in § 3.3.1.2) showed that already after 30 minutes geopolymer pastes become more resistant (higher stress values at the same deformation). So, to work in safe conditions, the printing speed is selected for each object to have no more than 25 cm of increase in height in 30 minutes.

On the other hand, the fast setting of geopolymers gives a strong limitation on the amount of material that can be printed for each batch. From trial and error approach, it was found that batches not larger than 2 kg of material should be used to avoid hardening of the material in the pipes and plugging in the screw extruder. Since the designed objects are more massive than 2 kg, it was not possible to print the whole part in one step and the process is periodically stopped to refill the tank of geopolymer paste.

During the trial printings, performed to set printing parameters, the formulation prepared and characterised was slightly changed to adapt to the screw extrusion system. A paste with a lower viscosity was empirically found to flow more uniformly, so the formulation has been changed reducing bentonite quantity and adding water (Table 3.5.3).

Table 3.5.3. Formulation actually used in the scale-up printing. The composition is slightly changed to adapt to the screw-extrusion printing process

Metakaolin (wt%)	Bentonite (wt%)	Activator (wt%)	Water (wt%)	Spirulina (wt%)
47.7	10.4	38.0	0.7	3.1

Three objects with different features were printed (§ 2.3.2): a hollow pipe with a thick perimeter, a model of Pirelli skyscraper and a hollow structure with a complex twisted geometry.

Regarding the pipe, during printing some flow instability occurred, probably caused by the too large diameter of the nozzle. The consequences of an instable flow are a lower surface definition, as well as the introduction of unwanted voids in the structure. At around the 80% of execution of the printing, a structural failure occurred in the bulged region, because of the excessive weight of the structure built above. The failure occurred longitudinally in correspondence with the passage point between subsequent layers, which is a region intrinsically characterized by the presence of voids (Figure 3.5.4). As a consequence of this failure, the top layers were deposited in a tilted position with respect to the original design and the final structure resulted to be visibly bent (Figure 3.5.3b).



Figure 3.5.3. (a) Printing process of the pipe; (b) final structure, showing a bent shape because of the structural failure occurred



Figure 3.5.4. Close-up on the failure point: as can be observed, the failure started in the discontinuity due to the change of layer

Conversely, no great structural issues showed up during the printing of the model of Pirelli skyscraper, thanks to the infill, which acted as a structural reinforce. The use of a smaller nozzle (4 mm instead of the 8 mm used for the pipe) guaranteed a more uniform flow, as well as lower weight of the stacked layers. Unfortunately, looking at the result (Figure 3.5.5b), the definition of the details is not as good as expected. Moreover, horizontal discontinuities due printing interruption can be clearly seen.

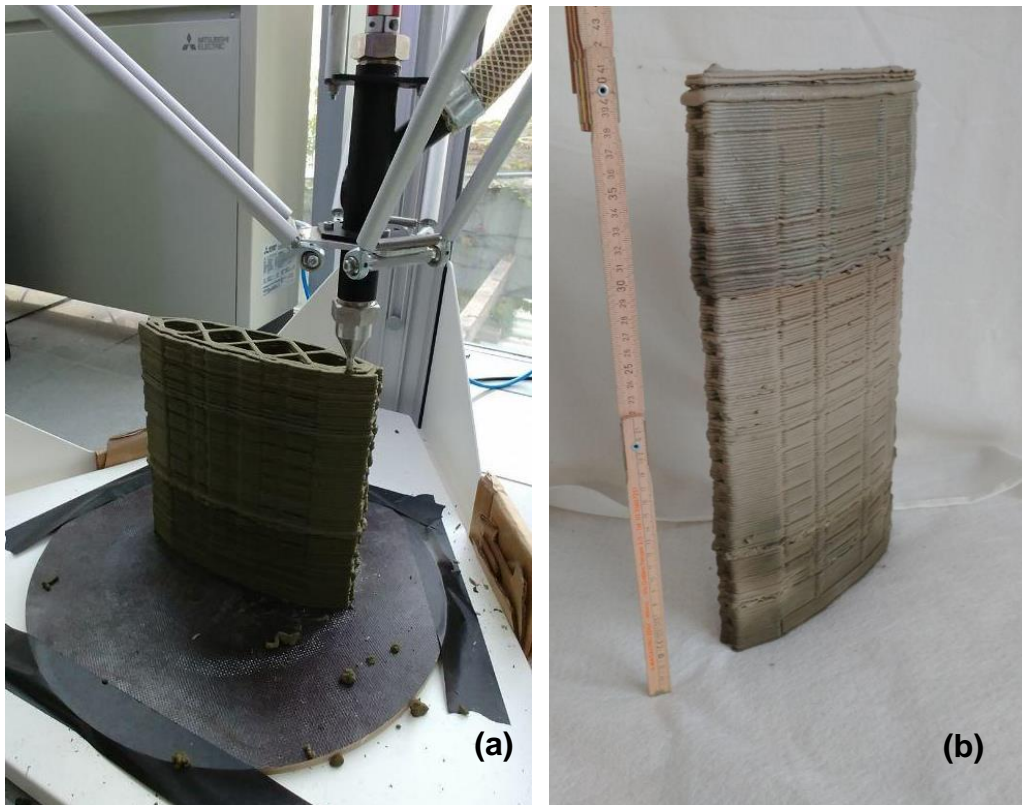


Figure 3.5.5. (a) Printing process of Pirelli skyscraper model; (b) result of the printing

The printing of the hollow twisted structure led to better results. Despite the absence of infill, the lighter structure, obtained by printing a thinner single walled-perimeter, self-sustained itself up until the conclusion of the printing. The small defects that can be observed at the top of the structure occurred because of flow instabilities, due to the approaching emptying of the tank.

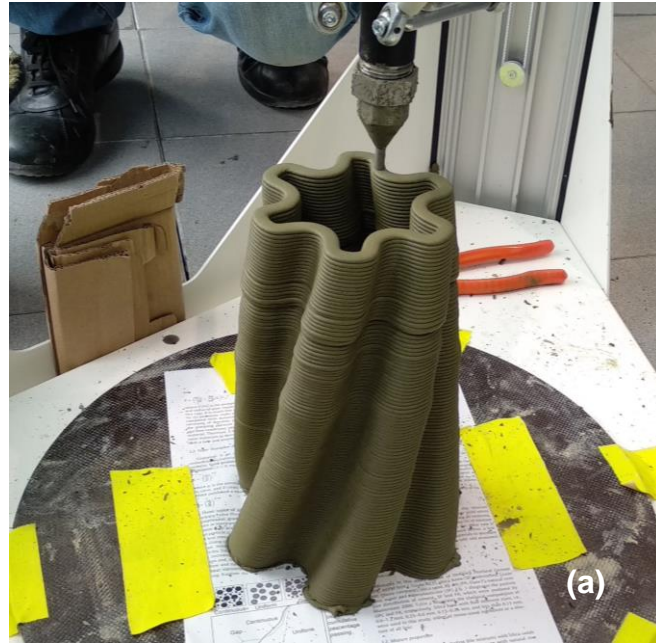


Figure 3.5.6. (a) Printing process of the hollow twisted structure; (b) final result

Summarizing, the printing of larger structure is feasible, with some restrictions. First of all, the change of formulation necessary to reduce viscosity, reduced also the ability of the material to sustain stresses. In addition, the batch configuration of the printing system entailed breaks of the printing, which caused visible discontinuities in the printed parts. Finally, high degree of detail cannot be successfully achieved with this technology at this scale for geopolymer cement.

The first two problems may be solved in principle by adopting a continuous feeding system, like a hopper. Better definitions could be achieved by using smaller nozzles or by printing larger structures.

4. Conclusions and future developments

4.1. Conclusions

Through this experimental work, a comprehensive study on liquid deposition modelling (LDM) additive manufacturing of geopolymers loaded with waste materials has been carried out. Many formulations have been prepared, having a fixed mass ratio between metakaolin and activator and variable amount of bentonite, added as rheology modifier, and fillers. All geopolymer formulations have been tested by following the main evolution stages of the printed material: the liquid paste has been studied through several rheology tests; then early-age hardening and mechanical properties of hardened specimens have been assessed by compression tests; finally, a relation between structure and properties has been investigated by SEM and EDS analyses. The effect of the addition of biomass (microalgae and lignin) and recycled glass fibres has been always taken into account in all the tests performed.

Regarding rheological properties, all pastes prepared for 3D printing applications showed a pseudoplastic behaviour with yield stress, which has been successfully modelled by Herschel-Bulkley's equation. While the pseudoplastic behaviour can be related to the addition of metakaolin to the activator liquid solution, which is a Newtonian fluid, the main responsible for the appearance of the yield stress is bentonite.

Yield stress is necessary to achieve a self-standing structure, but it can cause plugging problems and scarce printability if too high. The addition of microalgal biomass up to 5 per hundred parts (php) with respect to the powder weight, was found to be an effective way to reduce the yield stress without compromising the buildability of the structure. Keeping the W/S ratio constant, the minimum of yield stress has been found at 3 php, for any microalgal species used. This trend, clearly appreciable from rheological tests in static regime, has been confirmed by the analysis of the crossover point between the storage and the loss moduli in oscillatory regime. On the other hand, the addition of fibres increases the viscosity of the pastes and, in general, reduces their pseudoplasticity, leading to a worst flowability.

A window of printability has been defined through creep and recovery tests: all printable pastes showed recovery values of deformation around 10%, while non-printable formulations were able to recover less than 5% of the deformation applied.

The evolution of mechanical properties at early-age stages were assessed by compression tests of fresh casted samples. The main result of these experiments is that higher values of stress are reached earlier with formulations containing biomass. Therefore, biomass can be used as an accelerant of setting, which enables the possibility of reducing the printing time.

Compressive tests performed on the hardened material demonstrated that microalgal biomass and fibres can be effectively used as fillers up to 5 php and 10 php respectively, since their effect on mechanical properties is a slight reduction of compressive strength that, in most cases, can be neglected as far as the standard deviation of data is concerned. Differently, lignin in any case has a worsening effect.

The comparison between printed and casted samples demonstrated that 3D printing process does not affect mechanical properties directly. However, bentonite, whose addition is necessary to achieve the desired rheological behaviour, reduced compressive strength by 50-60% with respect to the unfilled geopolymer. In most cases, anyway, the values are in the range of normal strength concrete applications, which are between 16 MPa and 45 MPa. Higher values are reached, even exceeding 45 MPa, when a thermal treatment at high temperature is done.

A relation between mechanical properties and microstructure was found by SEM and EDS analyses. Biomass has the main effect of creating pores, reducing consequently density and compressive strength. High quantities of fibres, on the other hand, tend to generate cracks, which can be related to the lowering of mechanical properties.

Finally, the printing process of a formulation containing 5 php of Spirulina was scaled-up to obtain objects higher than 40 cm. The best printing result was achieved with a hollow lightweight structure, having a twisted shape very difficult to obtain with traditional manufacturing techniques. This object, reaching 45 cm height, is the highest printed structure in metakaolin-based geopolymer present in literature.

4.2. Future developments

The weakest aspect of all the formulations analysed for 3D printing applications is the reduction of compressive strength due to bentonite. In sight of using LDM technology to print buildings, an alternative to bentonite with a lower or no effect on mechanical properties should be found.

The study of different formulations can be interesting also to develop strategies to embed higher quantities of biomass or other waste materials in the geopolymer matrix. On the contrary, more experiments should be done on recycled glass fibres addition lower than 5 php, which may lead to reinforcing effects.

Large-scale printings, even larger than the ones already performed, are for sure a very important aspect to be furtherly developed. A different printing system, based on continuous instead that on batch feeding, should be used to avoid printing interruptions and consequently surface and structural defects.

Appendix

Results of preliminary studies

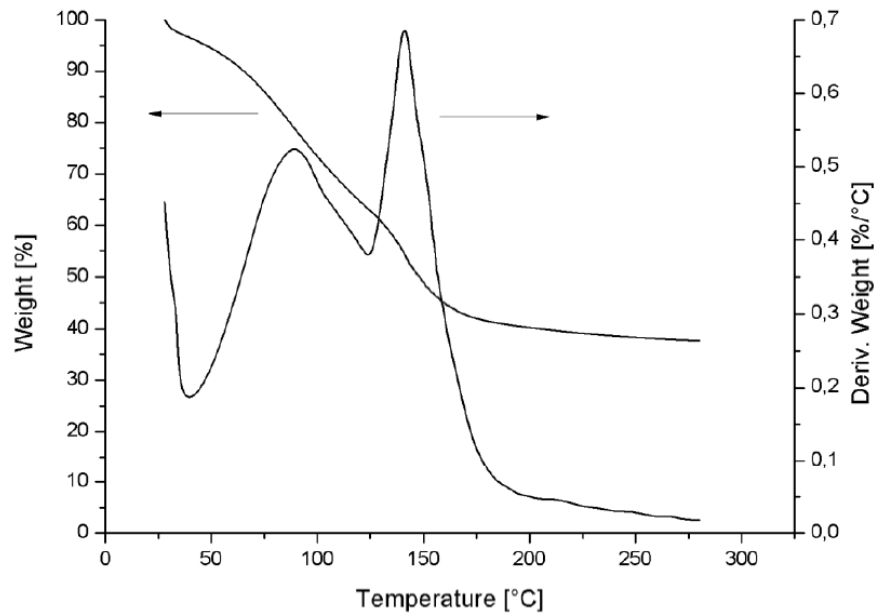


Figure A 1. TGA of the alkaline activator solution

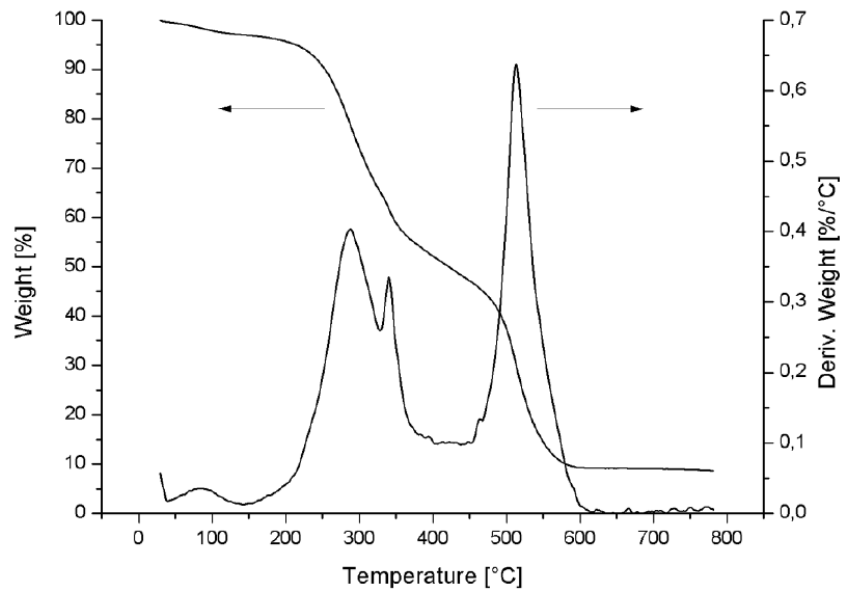


Figure A 2. TGA of Spirulina

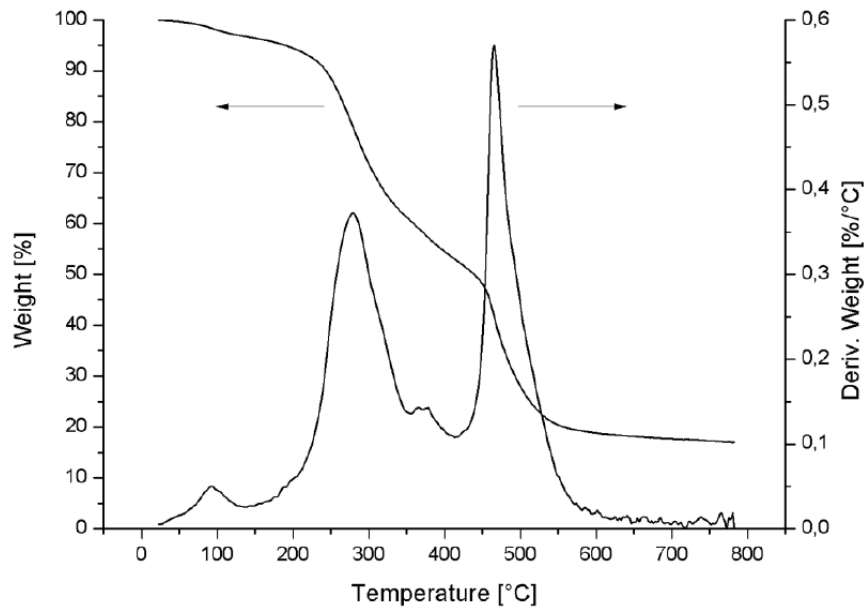


Figure A 3. TGA of Tetraselmis

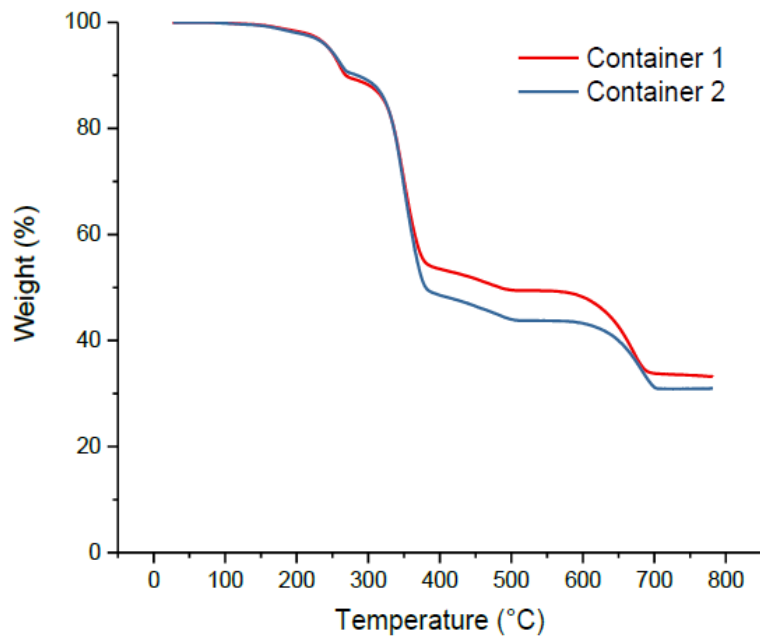


Figure A 4. TGA of red recycled glass fibres, performed on two batches

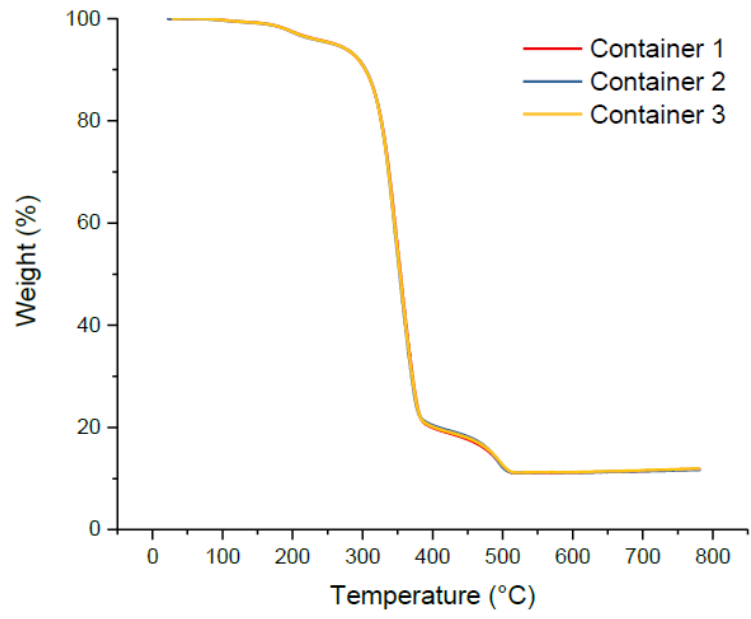


Figure A 5. TGA of white recycled glass fibres, performed on three batches

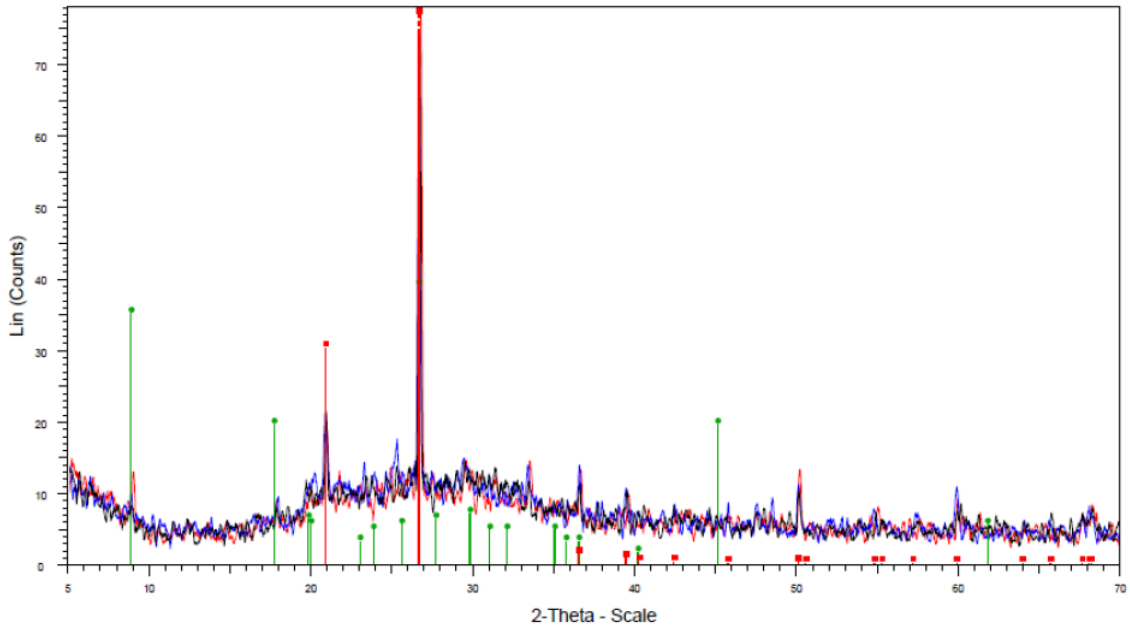


Figure A 6. XRD spectrum of metakaolin powder

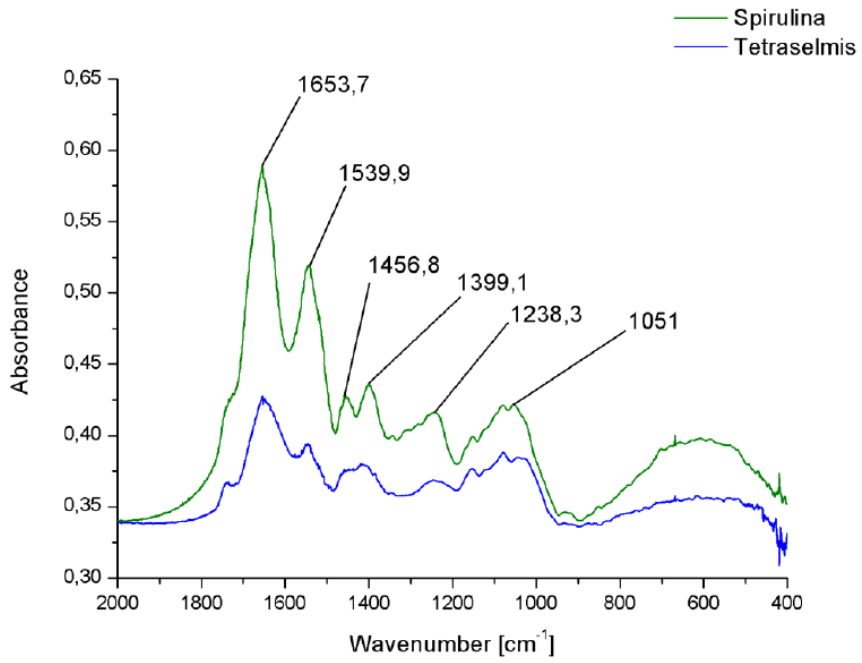


Figure A 7. FT-IR spectrum of microalgae

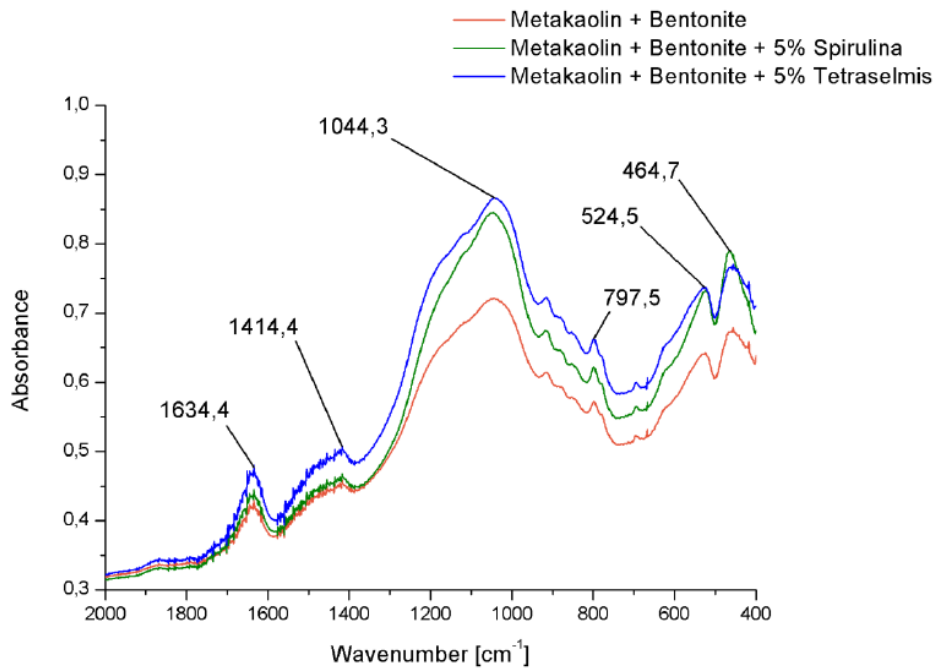


Figure A 8. FT-IR spectra of microalgae and geopolymer before geopolymerization

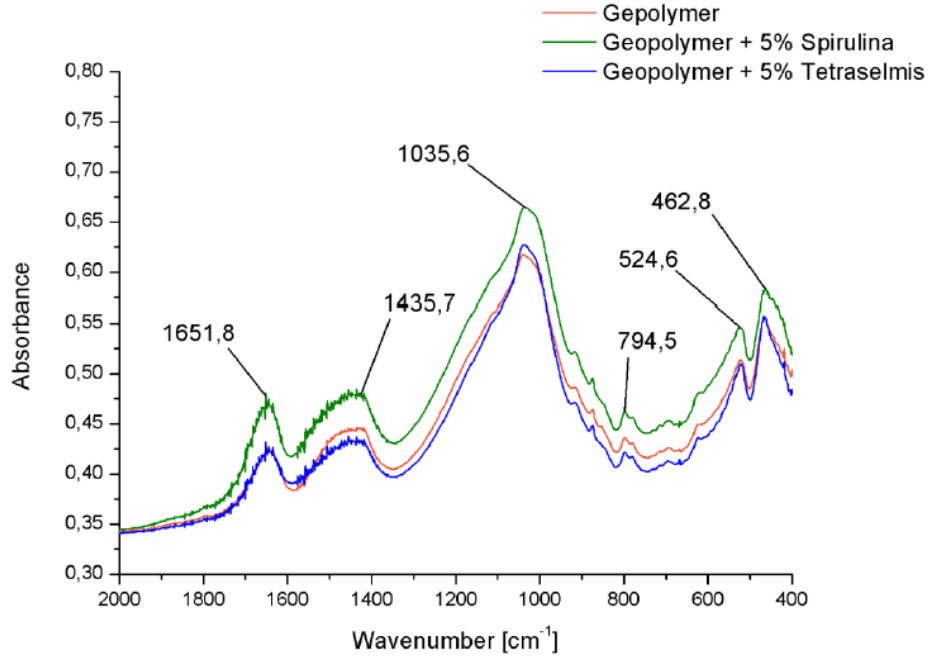


Figure A 9. FT-IR spectra of geopolymer and microalgae after geopolymerization

Estimation of maximum height of printed structures

Following the approach of Weng et al. [92], the maximum height of a printed structure is estimated according to Equation (6):

$$H = \frac{\alpha}{\rho g} \tau_y$$

α is defined through the following expression:

$$\alpha = (R_2^2 - R_1^2)^{-1} \left(\frac{1}{2} + \frac{C_\alpha}{R_2^2} \right)^{-1} \sqrt{\frac{3}{4} + \frac{C_\alpha^2}{R_2^4}} \cdot \left\{ \frac{4}{H} \left[\frac{R_2^3 - R_1^3}{6} + C_\alpha (R_2 - R_1) \right] + 2C_\alpha \left(\sqrt{\frac{3R_2^4}{4C_\alpha^2} + 1} - \sqrt{\frac{3R_1^4}{4C_\alpha^2} + 1} \right) - 2C_\alpha \left[\operatorname{arcsinh} \left(\frac{2C_\alpha}{\sqrt{3}R_2^2} \right) - \operatorname{arcsinh} \left(\frac{2C_\alpha}{\sqrt{3}R_1^2} \right) \right] - 2R_1^2 \left(\frac{3}{4} + \frac{C_\alpha^2}{R_1^4} \right)^{-0.5} \left(\frac{1}{4} - \frac{C_\alpha^2}{R_1^4} \right) - 2R_2^2 \left(\frac{3}{4} + \frac{C_\alpha^2}{R_2^4} \right)^{-0.5} \left(\frac{1}{4} - \frac{C_\alpha^2}{R_2^4} \right) \right\}$$

C_α can be computed solving the equation:

$$\frac{\frac{1}{2} - \frac{C_\alpha}{R_2^2}}{\sqrt{\frac{3}{4} + \frac{C_\alpha^2}{R_2^4}}} - \frac{\frac{1}{2} - \frac{C_\alpha}{R_1^2}}{\sqrt{\frac{3}{4} + \frac{C_\alpha^2}{R_1^4}}} + \operatorname{arcsinh}\left(\frac{2C_\alpha}{\sqrt{3}R_2}\right) - \operatorname{arcsinh}\left(\frac{2C_\alpha}{\sqrt{3}R_1}\right) = 0$$

Therefore, to find H , the parameter C_α was computed graphically and then inserted in the expression of α and in Equation (6), which was solved graphically, as well.

The estimation has been done on a single-walled cylinder, having $R_1 = 0.14 \text{ m}$ and $R_2 = 0.15 \text{ m}$. The yield stress considered is that of the formulation LB-GSP5 with B3, applied in the scale-up, which is 1446 Pa. The density was estimated by weighted average of the densities of the compound used in the mixtures, which is around 2230 kg/m³.

The final result is $H = 24 \text{ cm}$.

Bibliography

- [1] ASTM and ISO, “Standard Terminology for Additive Manufacturing – General Principles – Terminology,” *Iso/Astm*, vol. 52900, p. 9, 2015.
- [2] H. Miyanaji, M. Orth, J. M. Akbar, and L. Yang, “Process development for green part printing using binder jetting additive manufacturing,” *Front. Mech. Eng.*, vol. 13, no. 4, pp. 504–512, 2018.
- [3] T. D. Ngo, A. Kashani, G. Imbalzano, K. T. Q. Nguyen, and D. Hui, “Additive manufacturing (3D printing): A review of materials, methods, applications and challenges,” *Compos. Part B Eng.*, vol. 143, no. February, pp. 172–196, 2018.
- [4] I. Gibson, D. Rosen, and B. Stucker, *Additive Manufacturing Technologies: 3D Printing, Rapid Prototyping, and Direct Digital Manufacturing*. 2015.
- [5] N. Guo and M. C. Leu, “Additive manufacturing : technology , applications and research needs,” vol. 8, no. 3, pp. 215–243, 2013.
- [6] M. Invernizzi, G. Natale, M. Levi, S. Turri, and G. Griffini, “UV-assisted 3D printing of glass and carbon fiber-reinforced dual-cure polymer composites,” *Materials (Basel)*., vol. 9, no. 7, 2016.
- [7] A. Ambrosi and M. Pumera, “3D-printing technologies for electrochemical applications,” *Chem. Soc. Rev.*, vol. 45, no. 10, pp. 2740–2755, 2016.
- [8] F. Calignano *et al.*, “Overview on additive manufacturing technologies,” *Proc. IEEE*, vol. 105, no. 4, pp. 593–612, 2017.
- [9] I. Gibson, D. W. Rosen, and B. Stucker, *Additive Manufacturing Technologies*. 2010.
- [10] “<https://www.3dhubs.com/knowledge-base/additive-manufacturing-technologies-overview#direct-energy-deposition>.”, Accessed October 2018 .
- [11] K. V. Wong and A. Hernandez, “A review of additive manufacturing,” *ISRN Mech. Eng.*, vol. 2012, p. 10, 2012.
- [12] B. Berman, “3-D printing: The new industrial revolution,” *Bus. Horiz.*, vol. 55, no. 2, pp. 155–162, 2012.
- [13] J. Maric, F. Rodhain, and Y. Barlette, “Frugal innovations and 3D printing: insights from the field,” *J. Innov. Econ.*, vol. 21, no. 3, p. 57, 2016.
- [14] N. Radjou, P. Jaideep, and A. Simone, *Jugaad Innovation: Think Frugal, Be*

Flexible, Generate Breakthrough Growth. 2012.

- [15] J. Mair, I. Martì, and M. J. Ventresca, “Building inclusive markets in rural Bangladesh: how intermediaries work institutional voids,” *Acad. Manag. J.*, vol. 55, no. 4, pp. 819–850, 2012.
- [16] T. Campbell, C. Williams, O. Ivanova, and B. Garrett, “Could 3D Printing Change the World? Technologies, Potential, and Implications of Additive Manufacturing,” *Atl. Counc. Strateg. Foresight Rep.*, 2012.
- [17] “<https://www.sculpteo.com/blog/2017/01/18/3d-printing-benefits-impossible-designs-and-internal-channels/>,” Accessed August 2018.
- [18] J. L. Provis and J. S. J. van Deventer, *Geopolymers*. 2009.
- [19] J. Pegna, “Exploratory investigation of solid freeform construction,” *Autom. Constr.*, vol. 5, no. 5, pp. 427–437, 1997.
- [20] B. Khoshnevis and R. Dutton, “Innovative Rapid Prototyping Process Makes Large Sized, Smooth Surfaced Complex Shapes in a Wide Variety of Materials,” *Mater. Technol.*, vol. 13, no. 2, pp. 53–56, 1998.
- [21] B. Khoshnevis, D. Hwang, K.-T. Yao, and Z. Yeh, “Mega-scale fabrication by contour crafting,” *Int. J. Ind. Syst. Eng.*, vol. 1, no. 3, pp. 301–320, 2006.
- [22] S. Lim, R. A. Buswell, T. T. Le, S. A. Austin, A. G. F. Gibb, and T. Thorpe, “Developments in construction-scale additive manufacturing processes,” *Autom. Constr.*, vol. 21, no. 1, pp. 262–268, 2012.
- [23] G. W. Ma, L. Wang, and Y. Ju, “State-of-the-art of 3D printing technology of cementitious material—An emerging technique for construction,” *Sci. China Technol. Sci.*, pp. 1–21, 2017.
- [24] E. Canessa, C. Fonda, and M. Zennaro, *Low-cost 3D printing for science, education & sustainable development*. ICTP, 2013.
- [25] I. Hager, A. Golonka, and R. Putanowicz, “3D Printing of Buildings and Building Components as the Future of Sustainable Construction?,” *Procedia Eng.*, vol. 151, pp. 292–299, 2016.
- [26] “<https://www.3dnatives.com/en/crane-wasp-modular-3d-printer-construction-industry-251020184/>,” Accessed November 2018
- [27] “<https://www.3dwasp.com/>,” Accessed October 2018.
- [28] B. Panda, S. C. Paul, L. J. Hui, Y. W. D. Tay, and M. J. Tan, “Additive

- manufacturing of geopolymer for sustainable built environment,” *J. Clean. Prod.*, vol. 167, pp. 281–288, 2018.
- [29] B. Panda, S. C. Paul, N. A. N. Mohamed, Y. W. D. Tay, and M. J. Tan, “Measurement of tensile bond strength of 3D printed geopolymer mortar,” *Meas. J. Int. Meas. Confed.*, vol. 113, no. September 2017, pp. 108–116, 2018.
- [30] B. Panda and M. J. Tan, “Experimental study on mix proportion and fresh properties of fly ash based geopolymer for 3D concrete printing,” *Ceram. Int.*, no. March, 2018.
- [31] B. Panda, M. Li, Y. W. D. Tay, S. C. Paul, and M. J. Tan, “Modeling Fly Ash Based Geopolymer Flow for 3D Printing Applications,” *Int. Conf. Adv. Constr. Mater. Syst.*, no. September, pp. 9–16, 2017.
- [32] G. Cesaretti, E. Dini, X. De Kestelier, V. Colla, and L. Pambaguian, “Building components for an outpost on the Lunar soil by means of a novel 3D printing technology,” *Acta Astronaut.*, vol. 93, pp. 430–450, 2014.
- [33] P. Wu, J. Wang, and X. Wang, “A critical review of the use of 3-D printing in the construction industry,” *Autom. Constr.*, vol. 68, pp. 21–31, 2016.
- [34] D. Asprone, C. Menna, F. P. Bos, T. A. M. Salet, J. Mata-Falcón, and W. Kaufmann, “Rethinking reinforcement for digital fabrication with concrete,” *Cem. Concr. Res.*, no. January, pp. 0–1, 2018.
- [35] C. F. Revelo and H. A. Colorado, “3D printing of kaolinite clay ceramics using the Direct Ink Writing (DIW) technique,” *Ceram. Int.*, vol. 44, no. 5, pp. 5673–5682, 2017.
- [36] A. Zocca, P. Colombo, C. M. Gomes, and J. Günster, “Additive Manufacturing of Ceramics: Issues, Potentialities, and Opportunities,” *J. Am. Ceram. Soc.*, vol. 98, no. 7, pp. 1983–2001, 2015.
- [37] K. Komnitsas and D. Zaharaki, “Geopolymerisation: A review and prospects for the minerals industry,” *Miner. Eng.*, vol. 20, no. 14, pp. 1261–1277, 2007.
- [38] J. Davidovits, “Geopolymers and geopolymeric materials,” *J. Therm. Anal.*, vol. 35, no. 2, pp. 429–441, 1989.
- [39] J. W. Phair and J. S. J. Van Deventer, “Effect of the silicate activator pH on the leaching and material characteristics of waste-based geopolymers,” *Int. J. Miner. Process.*, vol. 66, no. 1–4, pp. 121–143, 2002.

- [40] M. . Villaquirán-Caicedo, R. Mejía de Gutiérrez, and N. C. Gallego, “A Novel MK-based Geopolymer Composite Activated with Rice Husk Ash and KOH: Performance at High Temperature,” *Mater. Construcción*, vol. 67, no. 326, pp. 1–13, 2017.
- [41] Z. H. Zhang, H. J. Zhu, C. H. Zhou, and H. Wang, “Geopolymer from kaolin in China: An overview,” *Appl. Clay Sci.*, vol. 119, pp. 31–41, 2016.
- [42] H. Xu and J. S. J. Van Deventer, “The geopolymerisation of alumino-silicate minerals,” 2000.
- [43] Z. Zuhua, Y. Xiao, Z. Huajun, and C. Yue, “Role of water in the synthesis of calcined kaolin-based geopolymer,” *Appl. Clay Sci.*, vol. 43, no. 2, pp. 218–223, 2009.
- [44] P. Duxson, A. Fernández-Jiménez, J. L. Provis, G. C. Lukey, A. Palomo, and J. S. J. Van Deventer, “Geopolymer technology: The current state of the art,” *J. Mater. Sci.*, vol. 42, no. 9, pp. 2917–2933, 2007.
- [45] D. Khale and R. Chaudhary, “Mechanism of geopolymerization and factors influencing its development: A review,” *J. Mater. Sci.*, vol. 42, no. 3, pp. 729–746, 2007.
- [46] J. Davidovits, “Geopolymers: Ceramic-like inorganic polymers,” *J. Ceram. Sci. Technol.*, vol. 8, no. 3, pp. 335–350, 2017.
- [47] P. De Silva, K. Sagoe-Crenstil, and V. Sirivivatnanon, “Kinetics of geopolymerization: Role of Al_2O_3 and SiO_2 ,” *Cem. Concr. Res.*, vol. 37, no. 4, pp. 512–518, 2007.
- [48] P. Duxson, J. L. Provis, G. C. Lukey, S. W. Mallicoat, W. M. Kriven, and J. S. J. Van Deventer, “Understanding the relationship between geopolymer composition, microstructure and mechanical properties,” *Colloids Surfaces A Physicochem. Eng. Asp.*, vol. 269, no. 1–3, pp. 47–58, 2005.
- [49] J. G. S. van Jaarsveld, G. C. Lukey, J. S. J. van Deventer, and A. Graham, “The stabilisation of mine tailings by reactive geopolymerisation,” *Minprex 2000 Int. Congr. Miner. Process. Extr. Metall.*, no. September, pp. 363–371, 2000.
- [50] X. Chen, A. Sutrisno, and L. J. Struble, “Effects of calcium on setting mechanism of metakaolin-based geopolymer,” *J. Am. Ceram. Soc.*, vol. 101, no. 2, pp. 957–968, 2018.

- [51] P. Duxson, G. C. Lukey, and J. S. J. Van Deventer, "Physical evolution of Na-geopolymer derived from metakaolin up to 1000 °c," *J. Mater. Sci.*, vol. 42, no. 9, pp. 3044–3054, 2007.
- [52] T. W. Cheng and J. P. Chiu, "Fire-resistant geopolymer produce by granulated blast furnace slag," *Miner. Eng.*, vol. 16, no. 3, pp. 205–210, 2003.
- [53] P. Duan, C. Yan, and W. Luo, "A novel waterproof, fast setting and high early strength repair material derived from metakaolin geopolymer," *Constr. Build. Mater.*, vol. 124, pp. 69–73, 2016.
- [54] P. Kinnunen *et al.*, "Recycling mine tailings in chemically bonded ceramics – A review," *J. Clean. Prod.*, vol. 174, pp. 634–649, 2018.
- [55] Y. M. Liew, C. Y. Heah, A. B. Mohd Mustafa, and H. Kamarudin, "Structure and properties of clay-based geopolymer cements: A review," *Prog. Mater. Sci.*, vol. 83, pp. 595–629, 2016.
- [56] C. Fernández-Pereira *et al.*, "Immobilization of heavy metals (Cd, Ni or Pb) using aluminate geopolymers," *Mater. Lett.*
- [57] C. Bai *et al.*, "High-porosity geopolymer foams with tailored porosity for thermal insulation and wastewater treatment," *J. Mater. Res.*, vol. 32, no. 17, pp. 3251–3259, 2017.
- [58] L. N. Tchadjie and S. O. Ekolu, "Enhancing the reactivity of aluminosilicate materials toward geopolymer synthesis," *J. Mater. Sci.*, vol. 53, no. 7, pp. 1–25, 2017.
- [59] A. Sudagar *et al.*, "A novel study on the influence of cork waste residue on metakaolin-zeolite based geopolymers," *Appl. Clay Sci.*, vol. 152, no. November 2017, pp. 196–210, 2018.
- [60] K. A. Komnitsas, "Potential of geopolymer technology towards green buildings and sustainable cities," *Procedia Eng.*, vol. 21, pp. 1023–1032, 2011.
- [61] R. D. Hooton, "Bridging the gap between research and standards," *Cem. Concr. Res.*, vol. 38, no. 2, pp. 247–258, 2008.
- [62] A. Nazari and J. G. Sanjayan, *Handbook of Low Carbon Concrete*. 2017.
- [63] B. L. Damineli, F. M. Kemeid, P. S. Aguiar, and V. M. John, "Measuring the eco-efficiency of cement use," *Cem. Concr. Compos.*, vol. 32, no. 8, pp. 555–562, 2010.

- [64] C. Meyer, “The greening of the concrete industry,” *Cem. Concr. Compos.*, vol. 31, no. 8, pp. 601–605, 2009.
- [65] P. Duxson, J. L. Provis, G. C. Lukey, and J. S. J. van Deventer, “The role of inorganic polymer technology in the development of ‘green concrete,’” *Cem. Concr. Res.*, vol. 37, no. 12, pp. 1590–1597, 2007.
- [66] N. Abdel-Raouf, A. A. Al-Homaidan, and I. B. M. Ibraheem, “Microalgae and wastewater treatment,” *Saudi J. Biol. Sci.*, vol. 19, no. 3, pp. 257–275, 2012.
- [67] Z. K. Abdulsada, *Evaluation of Microalgae for Secondary and Tertiary Wastewater Treatment*. 2014.
- [68] “[https://www.sciencelearn.org.nz/images/1023-eutrophication.](https://www.sciencelearn.org.nz/images/1023-eutrophication)”, Accessed September 2018.
- [69] J. Ruiz, P. Álvarez, Z. Arbib, C. Garrido, J. Barragán, and J. A. Perales, “Effect of nitrogen and phosphorus concentration on their removal kinetic in treated urban wastewater by *Chlorella vulgaris*,” *Int. J. Phytoremediation*, vol. 13, no. 9, pp. 884–896, 2011.
- [70] N. F. Gray, *Biology of wastewater treatment*. 2004.
- [71] L. Brandt, G. Sardina, and M. Ahmed, “Dispersion of swimming algae in laminar and turbulent channel flows : theory and simulations,” 2013.
- [72] S. Mobin and F. Alam, “Biofuel Production from Algae Utilizing Wastewater,” no. December, 2014.
- [73] M. A. Borowitzka, “Commercial production of microalgae: ponds, tanks, and fermenters,” *Prog. Ind. Microbiol.*, vol. 35, no. C, pp. 313–321, 1999.
- [74] L. L. Zhuang *et al.*, “The characteristics and influencing factors of the attached microalgae cultivation: A review,” *Renew. Sustain. Energy Rev.*, vol. 94, no. June, pp. 1110–1119, 2018.
- [75] “[http://saltgae.eu/.](http://saltgae.eu/)”, Accessed October 2018.
- [76] R. Johannes and A. Gosselink, *Lignin as a Renewable Aromatic Resource for the Chemical Industry Lignin as a renewable aromatic resource for the chemical industry*, no. May. 2016.
- [77] L. P. Christopher, B. Yao, and Y. Ji, “Lignin biodegradation with laccase-mediator systems,” vol. 2, no. March, pp. 1–13, 2014.
- [78] G. Gellerstedt, “Softwood kraft lignin: Raw material for the future,” *Ind. Crops*

- Prod.*, vol. 77, pp. 845–854, 2015.
- [79] M. Naceur Belgacem and A. Gandini, *Monomers , Polymers and Composites. .*
- [80] A. Duval, F. Vilaplana, C. Crestini, and M. Lawoko, “Solvent screening for the fractionation of industrial kraft lignin,” vol. 70, no. 1, pp. 11–20, 2016.
- [81] N. A. Shuaib and P. T. Mativenga, “Effect of Process Parameters on Mechanical Recycling of Glass Fibre Thermoset Composites,” *Procedia CIRP*, vol. 48, pp. 134–139, 2016.
- [82] K. Larsen, “Recycling wind turbine blades,” *Renew. Energy Focus*, vol. 9, no. 7, pp. 70–73, 2009.
- [83] S. J. Pickering, “Recycling Technologies For Thermoset Composite Materials,” *Adv. Polym. Compos. Struct. Appl. Constr. ACIC 2004*, vol. 37, pp. 392–399, 2004.
- [84] K. Yoon, A. DiBenedetto, and S. Huang, “Recycling of unsaturated polyester resin using propylene glycol K. H. Yoon,” vol. 38, no. 9, pp. 2281–2285, 1997.
- [85] G. Oliveux, J. L. Bailleul, and E. L. G. La Salle, “Chemical recycling of glass fibre reinforced composites using subcritical water,” *Compos. Part A Appl. Sci. Manuf.*, vol. 43, no. 11, pp. 1809–1818, 2012.
- [86] “[http://fibereuse.eu/.](http://fibereuse.eu/)”, Accessed October 2018.
- [87] M. Steinerova, L. Matulova, P. Vermach, and J. Kotas, “The brittleness and chemical stability of optimized geopolymer composites,” *Materials (Basel).*, vol. 10, no. 4, 2017.
- [88] G. Natale, “3D Composites Extrusion Project,” *Politec. di Milano*, 2014.
- [89] Alexander Ya. Malkin and Avraam I. Isayev, *Rheology*. 2017.
- [90] R. Suriano, G. Griffini, M. Chiari, M. Levi, and S. Turri, “Rheological and mechanical behavior of polyacrylamide hydrogels chemically crosslinked with allyl agarose for two-dimensional gel electrophoresis,” *J. Mech. Behav. Biomed. Mater.*, vol. 30, pp. 339–346, 2014.
- [91] Y. Jia, K. Peng, X. L. Gong, and Z. Zhang, “Creep and recovery of polypropylene/carbon nanotube composites,” *Int. J. Plast.*, vol. 27, no. 8, pp. 1239–1251, 2011.
- [92] Y. Weng, M. Li, M. J. Tan, and S. Qian, “Design 3D printing cementitious materials via Fuller Thompson theory and Marson-Percy model,” *Constr. Build. Mater.*, vol. 163, pp. 600–610, 2018.

- [93] A. Perrot, D. Rangeard, and A. Pierre, “Structural built-up of cement-based materials used for 3D-printing extrusion techniques,” *Mater. Struct. Constr.*, vol. 49, no. 4, pp. 1213–1220, 2016.
- [94] C. Targan, A. Olgun, Y. Erdogan, and V. Sevinc, “Effects of supplementary cementing materials on the properties of cement and concrete,” *Cem. Concr. Res.*, vol. 32, no. 10, pp. 1551–1558, 2002.
- [95] V. Živica, M. Palou, E. Kuzielová, and M. Žemlička, “Super High Strength Metabentonite Based Geopolymer,” *Procedia Eng.*, vol. 151, pp. 133–140, 2016.
- [96] R. J. M. Wolfs, F. P. Bos, and T. A. M. Salet, “Early age mechanical behaviour of 3D printed concrete: Numerical modelling and experimental testing,” *Cem. Concr. Res.*, vol. 106, no. February, pp. 103–116, 2018.
- [97] BS EN 206, “BSI Standards Publication Concrete — Specification , performance , production and conformity,” *Br. Stand.*, no. May, p. 30, 2013.
- [98] D. Heath and T. F. Tadros, “Rheological investigations of the effect of addition of free polymer to concentrated sterically stabilised polystyrene latex dispersions,” *Faraday Discuss. Chem. Soc.*, vol. 76, pp. 203–218, 1983.
- [99] G. Franchin *et al.*, “Direct ink writing of geopolymeric inks,” *J. Eur. Ceram. Soc.*, vol. 37, no. 6, pp. 2481–2489, 2017.
- [100] A. Kazemian, X. Yuan, E. Cochran, and B. Khoshnevis, “Cementitious materials for construction-scale 3D printing: Laboratory testing of fresh printing mixture,” *Constr. Build. Mater.*, vol. 145, pp. 639–647, 2017.
- [101] F. Bos, R. Wolfs, Z. Ahmed, and T. Salet, “Additive manufacturing of concrete in construction: potentials and challenges of 3D concrete printing,” *Virtual Phys. Prototyp.*, vol. 11, no. 3, pp. 209–225, 2016.

Ringraziamenti

Siamo arrivati alla fine della tesi e della mia carriera da studente di ingegneria. È giunto quindi il momento di ringraziare tutti coloro grazie ai quali è stato possibile raggiungere questo importantissimo traguardo. Sarò sintetico, nel mio stile.

In primis, grazie ai professori Marinella Levi e Stefano Turri. Grazie per la professionalità, la pazienza e per aver sempre creduto in me.

Restando in ambito accademico, non posso non ringraziare tutti i membri del ChIP Lab e del +Lab, che sono stati sempre disponibili ad aiutarmi e a darmi preziosi consigli. Oltre a Riccardo, che mi ha seguito fin dal primo giorno, vorrei ringraziare Gigliola, Gianmarco, Raffaella, Alessio, Checco, Gilli, Andrea e Marta. Un ringraziamento speciale va ai miei compagni di laboratorio, con cui ho condiviso questi lunghi ma indimenticabili mesi di tesi. Fuori dalle mura del Dipartimento, ringrazio Maurizio di Alfatest, per il fondamentale aiuto sulle prove di reologia, e Mattia di Superforma, senza il quale lo scale-up non sarebbe stato possibile.

Il ringraziamento più grande però va ai miei genitori, che hanno sempre sostenuto le mie scelte, permettendomi di dedicarmi allo studio fino ad ora. Senza di voi nulla di tutto ciò sarebbe stato possibile. Ringrazio poi i cari zii, per avermi offerto la loro ospitalità ed avermi trattato come un figlio per quattro lunghi anni.

Un grazie enorme va agli amici, che sono diventati di fatto la mia seconda famiglia. Ringrazio gli amici di sempre, come quelli conosciuti da un po' meno di "sempre"; grazie per aver condiviso con me momenti belli, meno belli, sessioni d'esame, ansie, gioie e le piccole cose di tutti i giorni. "Dalla Valle" ringrazio quindi Ale, il mio fratello acquisito, Giulia, Linda e Daniel, mentre "da Milano" Balza, Vera, Tom, Matte, Ciaglia, Marco, Anna, Prisca, Filo e Tob. Grazie anche a tutti coloro che non ho nominato, ma che sono stati al mio fianco in questi anni.

Infine, grazie a Maria, semplicemente per aver reso tutto più bello, regalandomi il primo e l'ultimo sorriso di ogni giorno.